

ULTRA-HIGH FREQUENCY PHOTOACOUSTIC MICROSCOPY:

FROM ORGANELLES TO ORGANISMS

by

Michael J. Moore

B. Math. University of Waterloo, Waterloo, Canada, 2013

A dissertation

presented to Ryerson University

in partial fulfillment of the

requirements for the degree of

Doctor of Philosophy

in the Program of

Biomedical Physics

Toronto, Ontario, Canada, 2019

© Michael Moore, 2019

Author's Declaration

I hereby declare that I am the sole author of this dissertation. This is a true copy of the dissertation, including any required final revisions, as accepted by my examiners.

I authorize Ryerson University to lend this dissertation to other institutions or individuals for the purpose of scholarly research.

I further authorize Ryerson University to reproduce this dissertation by photocopying or by other means, in total or in part, at the request of other institutions or individuals for the purpose of scholarly research.

I understand that my dissertation may be made electronically available to the public.

Abstract

Ultra-high Frequency Photoacoustic Microscopy: From Organelles to Organisms

Michael J. Moore

Doctor of Philosophy, Biomedical Physics

Ryerson University, 2019

This dissertation describes novel signal analysis and imaging techniques for ultra-high frequency (UHF, over 100 MHz) Photoacoustic Microscopy (PAM). New approaches for extracting information pertaining to object structure and scale are described, and novel sensing techniques and contrast mechanisms for imaging biological samples ranging from single cells to small organisms are presented.

In the first section, I describe a methodology for assessing the structure of biological cells using UHF-PAM. The power spectra of ultrasound (US) pulses backscattered from MCF-7 cells, and photoacoustic (PA) waves emitted from their dyed nuclei were fit to analytical solutions to determine cell and nucleus diameter, respectively. The measured cell diameters ($15.5 \pm 1.8 \mu\text{m}$) and nucleus diameters ($12 \pm 1.3 \mu\text{m}$) were used to calculate the mean cell nucleus-to-cytoplasm ratio (1.9 ± 1.0). Good agreement was observed between UHF-PAM measured values and literature.

In the second section, I present a novel technique for PA image reconstruction that utilizes unique features in the PA power spectra as a source of contrast. The technique, termed F-Mode, provides a means for differentiating between objects of different scale that surpasses the capabilities of conventional reconstruction approaches. The ability of

F-Mode to selectively accentuate absorbers of different size was demonstrated using experimental phantoms containing microspheres and cylindrical vessels, as well as in individual biological cells and live zebrafish larvae.

Finally, I developed a new sensing technique, termed Photoacoustic Radiometry (PAR). Unlike PAM, which depicts optical absorption, PAR images depict the optical attenuation properties of the imaged object. It was demonstrated that PAR can be used to image transparent samples which generate no PA signals, and that simultaneous triplex PAR/PA/US imaging could be realized using our approach. Simultaneous PAR/PA imaging of biological cells, as well as zebrafish larvae *in vivo*, was also demonstrated. UHF-PAM provided excellent visualization of vascular organization in the larval trunk and head. The simultaneously acquired PAR images depicted anatomical structure (e.g. the notochord, muscle segments) not visible in PAM due to insufficient optical absorption.

Potential areas of application for the new UHF-PAM techniques described in this dissertation include detection of cancer cells in blood samples, and investigation of tumour growth and metastasis.

Acknowledgements

From what I've been told, writing the Acknowledgements section is often done last. The fact that I am writing this at 2am the night (morning, rather) before this dissertation is to be submitted leads me to believe this is accurate (although, my sample size is only $n = 1$). I should like to say that I've followed tradition and left this last through sheer force of will, despite the tempting promise of procrastination that it offered. However, if truth be told, I have found writing this section a daunting task to begin. So many people throughout the years have had a profound influence on my journey to where I am - and for that matter, *who I am* - today, that it is difficult to know where to start. I can only acknowledge a small subset of the people that have made this journey possible, but it is with great pleasure that I do so.

Of course, I would be remiss not to express my deepest thanks to my supervisor, Dr. Michael Kolios. Thank you for your encouragement and for providing me with an education and environment that allowed my creativity to flourish. You have my deepest appreciation for your support and patience while I pursued the many hunches that I had, and for gently guiding me back when I veered too far off course. It is only now that I realize how ironic your lighthearted references to some of these pursuits as "going fishing" ended up being. Given some of my later work, it was eerily prophetic. The collaborative and collegial culture that you have fostered for myself and my fellow lab members is truly a testament to your prowess as a supervisor. If, one day, I can become half the mentor, half the teacher, and half the scientist that you are, I will have accomplished much.

This work also could not have been realized without the guidance of my supervisory committee members: Dr. Carl Kumaradas and Dr. Alexandre Douplik. I am grateful for their counsel, and for the many fruitful scientific discussions we have had over the course of my studies at Ryerson.

If it takes a village to raise a child, it takes a whole lab to train a scientist. To my friends and colleagues in the Kolios lab (both past and present), thank you for providing me with a constant source of inspiration and stimulating scientific discussion. Working with you has made my time at Ryerson truly enjoyable. I would like to extend special thanks to the following individuals. Elizabeth Berndl and Jiayin (Jenn) Dong, for keeping the lab running like a finely tuned machine. Vaskar Gnyawali and Joseph Sebastian, whose collaborative efforts made the acoustic/photoacoustic flow cytometry, and image flow cytometry results presented in this dissertation possible. To my friends Eno Hysi and Muhannad Fadhel, thank you for never hesitating to join me on all those aforementioned ‘fishing trips’, and for always being eager to embark on new ones regardless of whether or not we previously returned empty handed. Finally, I would like to extend my gratitude to my friend, and mentor, Dr. Eric Strohm. Thank you for being such a good scientific role model, and never losing your patience with me during the early days of my graduate work (even though I plagued you incessantly with questions, and still do to this day... but to a lesser extent). While Michael exemplified the kind of scientist I wanted to be, you epitomized the type of Doctoral student I aspired to be. I am deeply appreciative of your friendship.

There are some people that I simply cannot thank sufficiently in such a short preamble, and my parents are prime examples. Mom & Dad, thank you for always encouraging my curiosity, and for providing a loving and nurturing environment for me to grow up in. It led me down the path to where I am today. To my biological father, whom I lost at a very young age, I hope that I have grown into a man that you would be proud of. Finally, to my sister, all of my grandparents, my extended family, and my in-laws, thank you so much for your love and support throughout the years.

Last, but certainly not least, to my amazing wife, Lisa. I hold you above all else. We started our undergraduate degrees together a decade ago – back then, who would have imagined we would be where we are today. I cannot put into words how much your unconditional love and support over the years has meant to me. You have been a constant source of inspiration, and have made me a better person in every imaginable way. Without your encouragement, I would never have embarked upon this journey, let alone be so close to finishing it. This dissertation, like my future, is dedicated to you.

Table of Contents

Author's Declaration	ii
Abstract.....	iii
Acknowledgements.....	v
List of Tables.....	xi
List of Figures	xii
Nomenclature.....	xiii
Epigraph	xiv
Chapter 1 Introduction	1
1.1 Photoacoustic Imaging	1
1.2 Photoacoustic Microscopy.....	5
1.3 Theoretical Description of the Photoacoustic Effect.....	7
1.4 Frequency Domain Analysis of PA Signals	11
1.5 Goals and Major Contributions.....	16
1.6 Overview of Dissertation	16
Chapter 2 Assessment of the Nucleus-to-Cytoplasmic Ratio in MCF-7 Cells Using Ultra-high Frequency Ultrasound and Photoacoustics	19
2.1 Abstract	19
2.2 Introduction	20
2.3 Theory	23
2.3.1 Acoustic Scattering by a Fluid Sphere.....	23
2.3.2 Photoacoustic Signal from a Spherical Absorber.....	24
2.4 Methods.....	26
2.4.1 Preparation of the sample.....	26
2.4.2 System Setup and Measurement	26
2.4.3 Signal Processing.....	27
2.5 Results and Discussion	28
2.6 Conclusion.....	31
2.7 Acknowledgements.....	31
Chapter 3 Photoacoustic Frequency Mode (F-Mode) Imaging: Scale-specific Contrast from Organelles to Organisms	32
3.1 Abstract	32

3.2	Introduction	33
3.3	Description of the F-Mode Technique	36
3.4	Methods.....	38
3.4.1	Photoacoustic Tomography System	38
3.4.2	Photoacoustic Microscopy System	39
3.4.3	The F Mode Algorithm.....	40
3.4.4	Preparation and Imaging of Vessel Phantom.....	40
3.4.5	Preparation and Imaging of Bead Phantom	41
3.4.6	Culturing and Imaging of CAKI-2 Cells.....	42
3.4.7	Preparation and Imaging of Zebrafish Larvae	42
3.5	F-Mode Imaging in Photoacoustic Tomography	43
3.6	F-Mode Imaging in Photoacoustic Microscopy	46
3.6.1	F-Mode imaging of Polystyrene Microspheres	47
3.6.2	In vitro imaging of unstained CAKI-2 Cells	49
3.7	In-vivo Imaging of Zebrafish Larva	52
3.8	Discussion & Conclusion	55
3.9	Acknowledgements.....	57
Chapter 4 Triplex micron-resolution acoustic, photoacoustic, and optical transmission microscopy via Photoacoustic Radiometry		58
4.1	Abstract	58
4.2	Introduction	59
4.3	Methods.....	63
4.3.1	Description of the PAR Technique	63
4.3.2	System Specifications	63
4.3.3	PAR Imaging of a Transparent Sample.....	65
4.3.4	Simultaneous PAR and PA Imaging of Biological Samples	65
4.3.5	Triplex Imaging of an Integrated Circuit	66
4.4	Results & Discussion.....	67
4.4.1	PAR Characterization.....	67
4.4.2	PAR Imaging of a Transparent Sample.....	68
4.4.3	Simultaneous PA and PAR Imaging of Single Biological Cells.....	70
4.4.4	Triplex Imaging of Silicon Wafer.....	73
4.5	Conclusion.....	76

4.6	Acknowledgements.....	77
Chapter 5 Simultaneous Ultra-high Frequency Photoacoustic Microscopy and Photoacoustic Radiometry of Zebrafish Larvae <i>in vivo</i>		
		78
5.1	Abstract	78
5.2	Introduction	79
5.3	Methods.....	82
5.3.1	System setup.....	82
5.3.2	Preparation of Zebrafish Larvae.....	83
5.3.3	Image formation.....	84
5.4	Results & Discussion.....	85
5.4.1	<i>In vivo</i> Imaging of Transgenic Zebrafish	85
5.4.2	Simultaneous Duplex Imaging of Zebrafish Larvae	87
5.4.3	Inhibition of Vascular Growth.....	93
5.5	Conclusion.....	95
5.6	Acknowledgements.....	96
Chapter 6 Conclusions and Future Work.....		
		97
6.1	Summary of Findings.....	97
6.1.1	Assessment of the N:C Ratio of single cells.....	97
6.1.2	F-Mode Imaging	99
6.1.3	Description and Applications of PAR Imaging	101
6.1.4	Zebrafish Imaging.....	104
6.2	Future Work.....	105
6.2.1	High-throughput N:C assessment	105
6.2.2	Future Directions in UHF-PAM of Zebrafish Larvae	111
6.3	Conclusions	113
Appendix A – Supplementary Information for Chapter 3		
		114
Appendix B – Supplementary Information for Chapter 5.....		
		117
References.....		
		120
Glossary		
		147

List of Tables

Table 6.1: The mean values for the cell diameter, nucleus diameter, and N:C ratio calculated for MCF-7, PC₃, and MDA-MB-231 cell lines109

Table 6.2: Comparison of the cell diameter, nucleus diameter, and N:C ratio of PC₃ cells from the same cell population determined using different detection systems110

List of Figures

Figure 1.1 Overview of the photoacoustic (PA) effect	2
Figure 1.2 One-way acoustic attenuation in water as a function of frequency	3
Figure 1.3 PA images acquired at different length scales with various PA systems.....	4
Figure 1.4 Thermal and stress relaxation times.....	8
Figure 1.5 Comparison of the temporal profile of PA waves emitted by various geometries.....	11
Figure 1.6 Photoacoustic power spectra for PA waves emitted by various geometries	12
Figure 1.7 The effects of varying different absorber parameters on the PA power spectra.....	15
Figure 2.1 Schematic of the experiment setup and optical image of a MCF-7 cell	27
Figure 2.2 Measured and fit US and PA power spectra from cells and their nuclei	29
Figure 3.1 An overview of the F-Mode technique.....	37
Figure 3.2 MAP and F-Mode images of a gelatin vessel phantom.....	45
Figure 3.3 MAP and F-Mode images of polystyrene microspheres	48
Figure 3.4 Label-free MAP and F-Mode images of a CAKI-2 cell <i>in vitro</i>	52
Figure 3.5 F-Mode images of the trunk vasculature of a live zebrafish larva.....	54
Figure 4.1 A diagrammatic description of the PAR technique, and a measured RF-Line with PAR, PA and US signals.....	62
Figure 4.2 Schematic of the experimental PAR setup, conversion efficiency, and resolution.....	65
Figure 4.3 Brightfield and PAR images of an etched glass bottom petri dish.....	70
Figure 4.4 Comparison of optical microscopy with fused PA and PAR images of single cells	72
Figure 4.5 Images of an integrated circuit acquired with the triplex PAR/PA/US technique	74
Figure 4.6 PAR image of an integrated circuit acquired with high signal averaging	75
Figure 5.1 Schematic of the experimental setup.....	83
Figure 5.2 Fluorescence and PAM images of the trunk vasculature of a zebrafish larva	86
Figure 5.3 Brightfield, PAR, and PA images of the head of a casper zebrafish larva	89
Figure 5.4 PAR and PA images of the trunk of a 5 dpf <i>casper</i> zebrafish	91
Figure 5.5 Fluorescence, PAR, and PA images of larval zebrafish treated with I3M	94
Figure 6.1 Box-and-whisker plots of the calculated cell and nucleus diameters for MCF-7, PC3, and MDA-MB-231 cells.....	107
Figure 6.2 Box-and-whisker plot of the cell N:C ratios.....	108

Nomenclature

λ	Wavelength [m ⁻¹]
NA	Numerical Aperture [dimensionless]
v_s	Longitudinal Speed of Sound [m·s ⁻¹]
f	Acoustic Frequency [MHz]
f_c	Transducer central frequency [MHz]
θ	Transducer semi-aperture angle [°]
Δf	Transducer bandwidth [MHz]
τ_{th}	Thermal relaxation time [s]
τ_s	Stress relaxation time [s]
α	Thermal Diffusivity [mm ² ·s ⁻¹]
a	Characteristic length [m]
p_0	Initial pressure [Pa]
Γ	Grüneisen parameter [dimensionless]
μ_a	Optical absorption coefficient [cm ⁻¹]
F	Optical fluence [J·cm ⁻²]
β	Thermal expansion coefficient [K ⁻¹]
κ	Compressibility [Pa ⁻¹]
ρ	Density [kg·m ³]
C_v	Thermal Capacity at constant volume [J·kg ⁻¹ ·K ⁻¹]
C_p	Thermal Capacity at constant pressure [J·kg ⁻¹ ·K ⁻¹]
H	Heat per unit time per unit volume [J·cm ⁻³ ·s ⁻¹]

“Give me a place to stand, and with a lever, I will move the whole world”

– Archimedes of Syracuse

c. 287 - 212 BC

Chapter 1

Introduction

1.1 Photoacoustic Imaging

Röntgen's discovery of the X-ray in the mid-1890's and the subsequent production of the first radiographic image of a human hand [1] paved the way for modern day biomedical imaging. In the century that followed the field matured, yielding state-of-the-art clinical imaging technologies including X-ray Computed Tomography (CT), Ultrasound (US), Magnetic Resonance Imaging (MRI), and Positron-Emission Tomography (PET). In 1880, fifteen years prior to Röntgen's discovery, Alexander Graham Bell reported on a technique involving "the production and reproduction of sound by light", which would ultimately give rise to a new form of medical imaging. Bell demonstrated that spoken words which modulated the intensity of a light source could be reproduced upon refocusing the light onto a thin diaphragm [2,3]. The phenomenon which Bell had discovered has assumed many names over the years [4]; however, it is now most commonly known as the photoacoustic (PA) effect. An overview of the PA effect is shown in Figure 1.1. The requisite for the production of a PA wave is absorption of an intensity modulated source of optical energy, such as a pulsed laser, by a target. This results in a thermoelastic expansion and subsequent non-radiative relaxation which gives rise to a

broadband acoustic wave [5,6]. Detection of these PA waves with an ultrasonic transducer allows for the mapping of optically absorbing chromophores within a target sample.

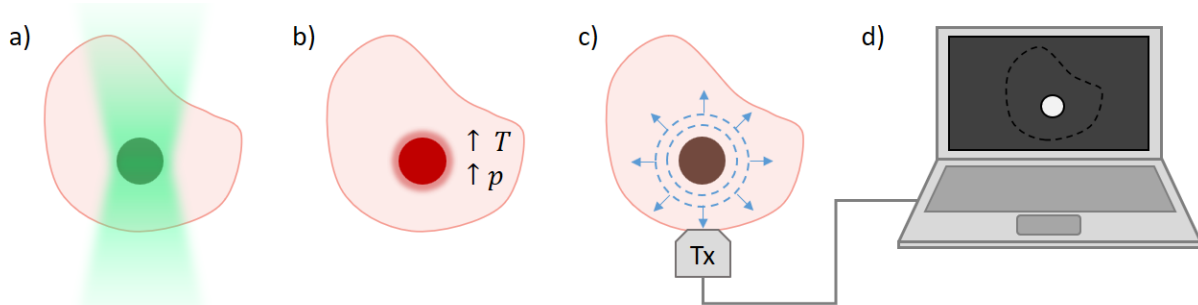


Figure 1.1: Overview of the photoacoustic (PA) effect. a) A short laser pulse (green) irradiates an optically absorbing target within a sample (in this case, biological tissue). b) Absorption of the laser pulse by chromophores results in an increase in temperature (T) and pressure (p) within the target. c) The pressure equilibrates with the surroundings via the emission of an acoustic (PA) wave, which can be detected using an ultrasonic transducer (Tx). d) An image showing the spatial distribution of optical absorption in the sample can then be reconstructed from the detected PA signal.

The PA technique was first applied to spectroscopic analysis of biological samples (cytochrome c and hemoglobin) in 1973 [7]; however, it was another 20 years before PA would be utilized for the purposes of biomedical imaging [8,9]. In present day, PA imaging is a rapidly growing discipline with an increasingly important role in biomedical research. Many imaging studies have been performed on animal models, such as rodents [10,11], rabbits [12,13], and monkeys [14,15]. Emerging areas of clinical application range from mapping of vasculature in the human breast [16,17], to label-free assessment of cancers [18–21] and other diseases [22–24]. For implementations where maximal imaging depth is desired, transducers with central frequencies in the range of 5 - 20 MHz are employed [22,25]. With these clinical frequency transducers and diffuse optical illumination, imaging depths of several centimeters *in vivo* [16,26,27], and up to 11.6 cm in *ex vivo* biological tissue

[28] have been achieved. This is well beyond the ballistic regime for photons in tissue (~ 1 mm) which constrains other optical imaging techniques like optical coherence tomography (OCT) [29] or multi-photon microscopy [30].

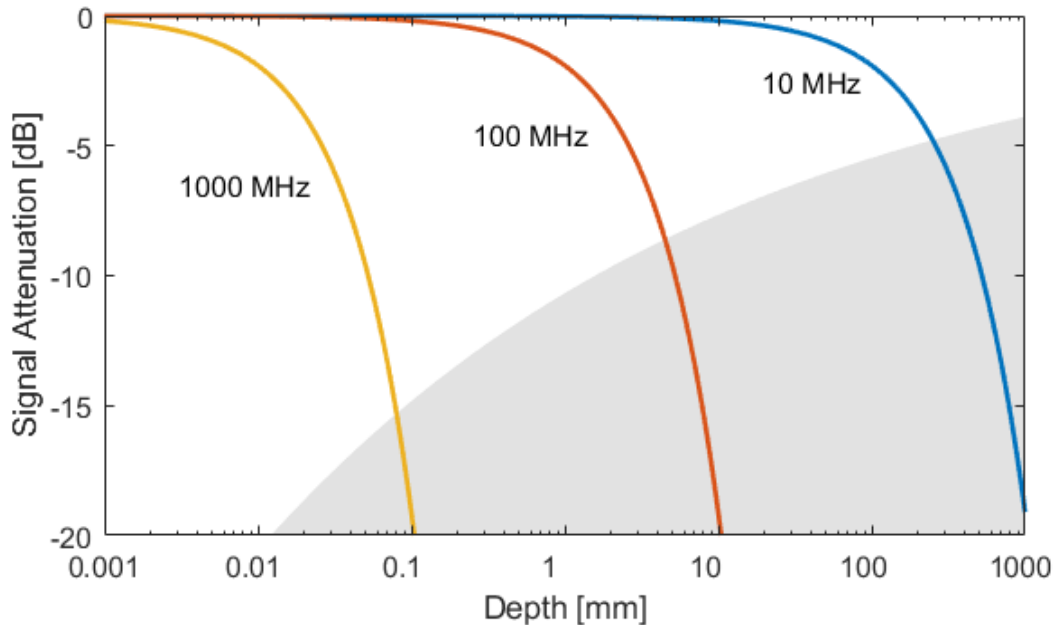


Figure 1.2: One-way acoustic attenuation in water as a function of frequency and depth for transducers with 10, 100, and 1000 MHz central frequencies. The shaded region indicates depths that are beyond the typical focal length of the transducer. Adapted from [31].

As in US imaging, there is a trade-off between the imaging depth and spatial resolution of acoustic resolution PA imaging systems. The resolution of the previously described PA imaging systems is proportional to the central frequency of the ultrasonic transducer employed, with higher frequencies yielding improved spatial resolution. However, the attenuation of an acoustic wave is frequency dependent, with higher frequencies experiencing increasing attenuation. For acoustic waves propagating in water, the attenuation increases with a f^2 dependence, increasing from 0.22 dB/m at 1 MHz to 0.22 dB/ μm at 1 GHz [32]. Thus, due to attenuation, high spatial resolutions are only

attainable at shallow imaging depths. Figure 1.2 illustrates the one-way decrease in the amplitude of acoustic waves for transducers of different central frequencies. For central frequencies in the hundreds of megahertz (MHz), transducer working distances are typically below 1 mm in order to preserve adequate signal-to-noise (SNR) ratios. By extension, this limits the PA interrogation depth to samples on the order of micrometers in thickness, or at 1000 MHz, a few cell layers at most [31]. While limited clinical applications exist at these depths, the enhanced lateral and axial resolution is ideal for studies requiring micron-scale resolution of microscopic samples. This demonstrates one of the main advantages of PA imaging; namely, the ability to image objects at substantially different length scales through the modification of the system parameters. Figure 1.3 provides an example of this scalability, showing a PA image of a stained leukocyte in a human blood smear (transducer central frequency 1 GHz), a tumour on the back of a mouse growing from inoculated BT-474 breast cancer cells (40 MHz), and the forearm and radial artery of a human subject (21 MHz).

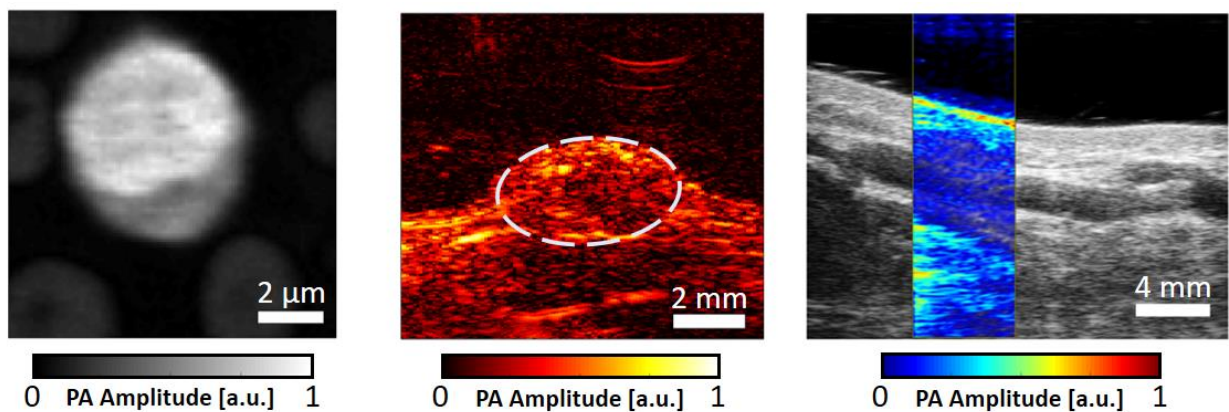


Figure 1.3: *Left* PA microscopy image of a stained human leukocyte acquired with a 1 GHz US transducer (adapted from [34]). *Middle* PAT image of a tumour grown on the back of a mouse (courtesy of Yanjie Wang, Ryerson). *Right* PAT image (colour) of the forearm and radial artery of a 28 year old healthy human male. The PA image is overlaid on top of an US image (grayscale) for context (courtesy of Tae-Hoon Bok, Ryerson).

1.2 Photoacoustic Microscopy

When single cell or sub-cellular resolution is required, such as when imaging individual capillaries or organelles within biological cells, a variant of PA imaging known as photoacoustic microscopy (PAM) is utilized [33–35]. Due to the high endogenous absorption of hemoglobin, PAM has been used for label-free mapping vascular networks, and determining hemoglobin oxygen saturation in single capillaries [36–41]. By leveraging endogenous chromophores like melanin [42–44], cytochromes [45,46], hemoglobin [34,44,47–49], and DNA [50–52], label-free imaging of individual biological cells and their organelles has become an area of increasing interest. Additionally, exogenous contrast agents such as dyes [34,53–55] and nanoparticles [56–59], can be used to increase image contrast or enable imaging of otherwise optically transparent samples.

There are two variants of PAM: optical-resolution PAM (OR-PAM), where the size of the optical focal spot is smaller than that of the acoustic focal spot; and acoustic-resolution (AR-PAM), where the opposite is true. For OR-PAM, the lateral resolution, R_{lat}^{OR} , is determined by the laser spot size at the objective focus:

$$R_{lat}^{OR} = \frac{0.51\lambda}{NA} \quad (1.1)$$

where λ is the wavelength of the illuminating laser, and NA is the numerical aperture of the focusing objective. By using high NA (>1) water-immersion objectives, lateral resolutions down to 220 nm have been reported with an illumination wavelength of 532 nm [42,60]. In AR-PAM, low NA objectives provide broad sample illumination while

tightly focused acoustic transducers control the lateral resolution. The spot size of a focused single-element transducer is given by [32,61]:

$$R_{\text{lat}}^{\text{AR}} = \frac{0.51 \left(\frac{v_s}{f_c} \right)}{\sin(\theta)} \quad (1.2)$$

where v_s is the speed of sound in the acoustic coupling medium, f_c is the transducer central frequency, and θ is the transducer semi-aperture angle. For *in vivo* PAM, US transducers with central frequencies of 50 MHz have been used to provide a lateral resolution of 45 μm at up to several millimeters depth [33,36,62]. The axial resolution in both OR-PAM and AR-PAM systems is dictated by the bandwidth, Δf , of the receiving US transducer [63,64]. It can be described by the full-width at half-maximum (FWHM) of the envelope of the system impulse response, and is given by:

$$R_{\text{ax}} = \frac{0.88v_s}{\Delta f}. \quad (1.3)$$

Most AR-PAM systems are designed to provide high resolution at depth, and thus, use transducers with central frequencies lower than 100 MHz. The bandwidths of these transducers are approximately 35 – 50 MHz, which is equivalent to an axial resolution between 26 and 37 μm (Equation 1.3). It should be noted that in early AR-PAM work, systems with sub-50 MHz bandwidth having axial resolutions of 15 μm were reported [36,62]. However, these resolutions were estimated using a shift-and-sum technique, which considers superposition of signals from two adjacent point targets at the 10% contrast point [65]. The FWHM approach has since proven to be a more realistic estimate [64,65], and is now the most prevalently used criterion.

The majority of this dissertation is devoted to the analysis of biological samples using PAM with ultra-high frequency (UHF) transducers (UHF-PAM). These UHF-PAM systems have comparable optical and acoustic lateral resolution by virtue of the high central frequencies (in the hundreds of MHz) of the transducers used. Furthermore, the large bandwidth of the UHF transducers (>100 MHz) yields axial resolutions down to 1 μm [44], enabling high resolution 3D imaging. Few PAM imaging studies above 100 MHz have been performed, although it is an area of steadily increasing interest [22,34,44,64,66–69]. Aside from imaging, quantitative analysis of UHF-PA signals can be used to ascertain morphological properties of biological samples (e.g. cells and organelles) without the need for resolving their structure. A theoretical framework and background for these analysis techniques is provided in the subsequent two sections.

1.3 Theoretical Description of the Photoacoustic Effect

The PA effect occurs subsequent to the absorption of an intensity modulated source of light (e.g. a pulsed laser) by an optically absorbing target region within an object. For a given target, the temporal pulse width of the laser beam must satisfy two criteria for maximum pressure buildup. First is the condition of thermal confinement; that the pulse energy should be deposited on timescales short enough that heat conduction is negligible. For this to be satisfied, the pulse duration should be shorter than the thermal relaxation time τ_{th} defined as [25,70,71]:

$$\tau_{th} = \frac{a^2}{4\alpha} \quad (1.4)$$

where α is the thermal diffusivity of the target, and a is the targets characteristic length. For biological tissues, the value of α is typically between 0.12 and $0.15 \text{ mm}^2 \cdot \text{s}^{-1}$ [72,73].

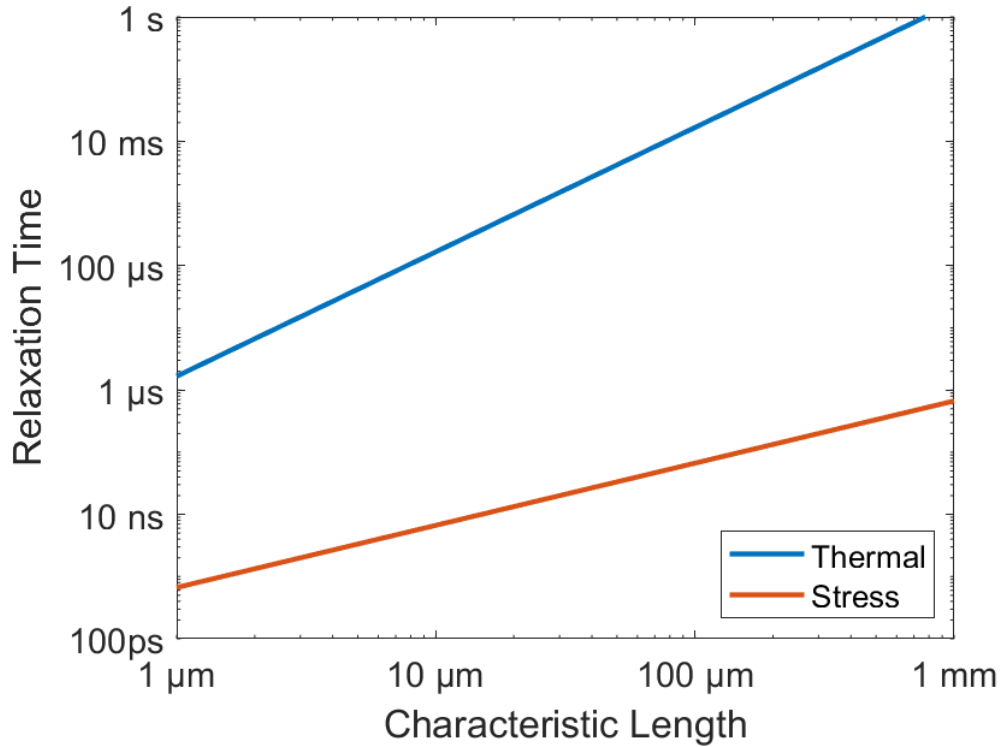


Figure 1.4: Thermal and stress Relaxation times for objects of varying characteristic length, and material properties mimicking tissue. Here $\alpha = 0.15 \text{ [mm}^2 \cdot \text{s}^{-1}]$, and $v_s = 1500 \text{ [m} \cdot \text{s}^{-1}]$.

The second criteria which must be fulfilled for maximizing the pressure of the PA wave is stress confinement; that the energy deposition should occur on timescales short enough that the stress buildup due to isochoric heating has not yet resulted in any volume change [70]. This occurs on timescales shorter than the stress relaxation time, τ_s , defined by:

$$\tau_s = \frac{a}{v_s} \quad (1.5)$$

where a is defined as above, and v_s is the longitudinal speed of sound within the target. Figure 1.4 shows τ_{th} and τ_s for characteristic lengths ranging from 1 μm to 1 mm for an object with $\alpha = 0.15 \text{ mm}^2 \cdot \text{s}^{-1}$ and $v_s = 1500 \text{ m} \cdot \text{s}^{-1}$. With these tissue mimicking conditions, τ_s is the limiting timescale, and ranges from 667 ps to 667 ns. This motivates the common choice of nanosecond pulse-width lasers for PAM applications.

With thermal and stress confinement conditions satisfied, the initial pressure increase in the target is:

$$p_0 = \Gamma \mu_a F \quad (1.6)$$

where μ_a [cm^{-1}] is the optical absorption coefficient of the target, and F [$\text{J} \cdot \text{cm}^{-2}$] is the fluence of the illuminating laser pulse. The dimensionless quantity Γ is known as the Grüneisen parameter, and it relates the pressure increase in the target to the absorbed volumetric optical energy density. The value of Γ is between 0.1 – 0.2 for biological tissue [70] and is given by:

$$\Gamma = \frac{\beta}{\kappa \rho C_v} \quad (1.7)$$

where β is the target thermal expansion coefficient, κ the isothermal compressibility, ρ the density, and C_v the heat capacity at constant volume. It should be noted that Γ has a dependence on temperature, and in some cases $\Gamma = 0$, resulting in no PA wave emission even when the appropriate conditions are satisfied [74,75].

After emission, the propagation of the PA wave at position \mathbf{r} and time t is governed by an inhomogeneous wave equation [76]:

$$\nabla^2 p(\mathbf{r}, t) - \frac{1}{v_s^2} \frac{d^2}{dt^2} p(\mathbf{r}, t) = -\frac{\beta}{C_p} \frac{\partial H(\mathbf{r}, t)}{\partial t} \quad (1.8)$$

where β is defined as previously, and C_p is the heat capacity at constant pressure. Here $H(\mathbf{r}, t) = A(\mathbf{r})T(t)$ is the heat deposited per unit volume and time in the target, where $A(\mathbf{r})$ has units of $[\text{W}\cdot\text{m}^{-3}]$ and describes the optical energy deposition at \mathbf{r} , and $T(t)$ has units of $[\text{s}^{-1}]$ and describes the temporal profile of the illumination [10,35,77]. Provided that there is homogenous optical illumination of the target, and that the target has sound speed and density identical to those of the surrounding fluid, Equation 1.8 can be solved via Green's function techniques for objects that are symmetrical in their coordinate systems [77]. The photoacoustic pressure predicted by the solution of Equation 1.8 at an observation point, r , for the case of a fluid layer, cylinder, and sphere are shown as dashed curves in Figure 1.5. For all geometries, the characteristic length was $7.5 \mu\text{m}$, the sound speeds of the object and the surrounding media were $1500 [\text{ms}^{-1}]$, and the densities of the object and media were $1000 [\text{kg}\cdot\text{m}^{-3}]$. For generality, the profiles were plotted as a function of dimensionless retarded time, $\tau = \frac{v_s}{a} \left(t - \frac{r-a}{v_s} \right)$. While the waveform profiles are easily distinguishable for these analytical results, in practice the bandpass effects of the transducer can make it difficult to differentiate between objects with different morphologies [78]. This is exemplified by the solid blue curves in Figure 1.5, which were obtained by applying a bandpass filter (4th order Butterworth, low cutoff of 200 MHz, high cutoff of 500 MHz) to the associated analytical curves. Since the bandpassing effects of the

transducer are multiplicative in the frequency domain, unique features in the power spectra dictated by object morphology are largely preserved within the transducer bandwidth. This makes analysis of the Fast Fourier Transform (FFT) of experimentally recorded PA signals an attractive alternative for quantitative analysis techniques.

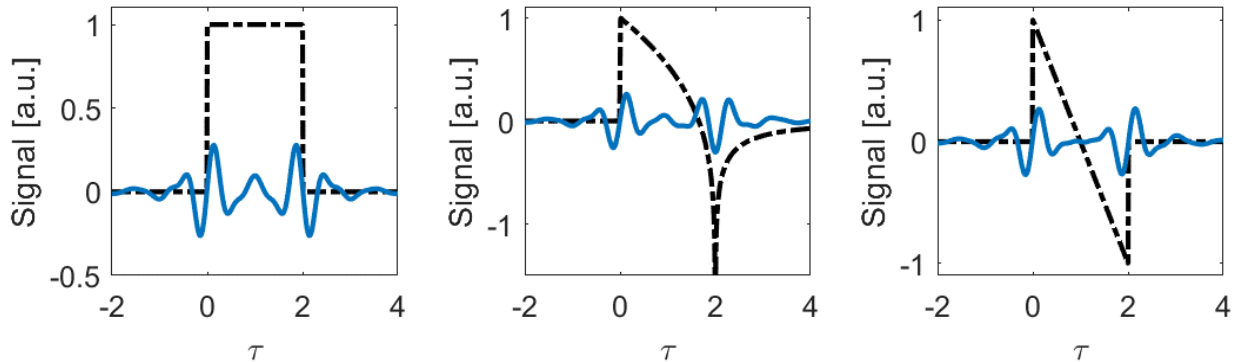


Figure 1.5: Comparison of the temporal profile of PA waves emitted by a fluid layer (left), cylinder (middle), and sphere (right). The dashed lines show the theoretical solutions, while the blue curves have had a bandpass filter applied to simulate the transducer response. Here, τ is the dimensionless retarded time.

1.4 Frequency Domain Analysis of PA Signals

Photoacoustic waves are inherently broadband, and their power spectra are encoded with information pertaining to the shape, size, and acoustic properties of the source object which produced them (Figure 1.6). Theory describing the features and profile of PA power spectra were developed starting in the late 1980's for simple optically thin geometries surrounded by transparent fluids [77,79–82]. In general, there are four main parameters which affect the profile of the power spectra, namely: the absorber shape, characteristic length, speed of sound, and density. This section will consider the effects that variations in each parameter have on the shape of the power spectrum.

For the case of geometries which exhibit symmetry about their coordinate axes (e.g. a layer (1D), cylinder (2D), sphere (3D)) analytical solutions for PA power spectra exist and have been experimentally validated [77,79–82]. The spectra of the PA emission from a layer, cylinder, and sphere are shown in Figure 1.6. Each object was set to have acoustic properties identical to those of the surrounding medium. In this case, the location of the minima (henceforth referred to as ‘spectral minima’) are the most distinguishing features of the spectra. For these simple geometries, the location of the minima are unique, and can be mapped by common functions. Analytical solutions have also recently been developed for oblate and prolate spheroids; however, these solutions have yet to be experimentally validated [83,84]. For more complex geometries, e.g. the bi-concave shape of a red blood cell (RBC), no analytical solutions exist, and Finite Element Method (FEM) techniques must be used to calculate the profile of the power spectrum [85].

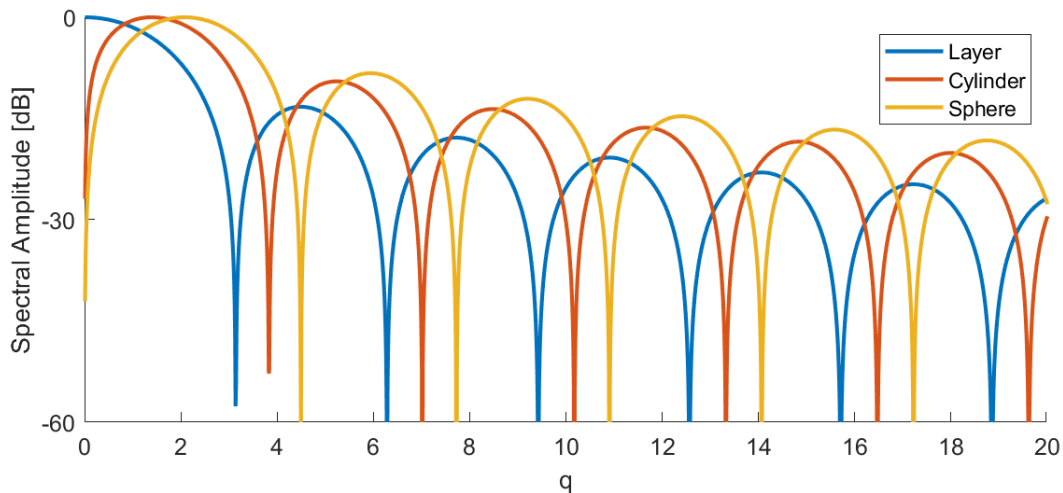


Figure 1.6: Photoacoustic power spectra for a layer (blue), cylinder (orange), and sphere (yellow) as a generalized function of $q = \frac{2\pi a}{v_s} f$. The placement of the spectral minima is unique for each object.

The power spectrum of a spherical object will be considered for investigation of the effects of variation in the remaining parameters. Spheres are of particular interest as biological cells can be approximated as poroelastic spheres composed of a viscous liquid and elastic matrix when in suspension [86]. For the case of a uniformly illuminated spherical droplet in a fluid, the frequency domain solution for the pressure at a distance r from the centre of the sphere is given by [82]:

$$P(q) = \left(\frac{i\mu_a\beta I_0 v_s^s a^2}{C_p r} \right) \frac{\left[\frac{\sin(q) - q \cos(q)}{q^2} \right] \exp(-iq\tau)}{\left[\left(1 - \frac{\rho_s}{\rho_f} \right) \left(\frac{\sin(q)}{q} \right) - \cos(q) + i \left(\frac{\rho_s v_s^s}{\rho_f v_s^f} \right) \sin(q) \right]} \quad (1.9)$$

Where I_0 is the intensity of the light, v_s^s and v_s^f are the speeds of sound in the droplet and surrounding fluid, respectively; ρ_s and ρ_f are the densities of the droplet and fluid, a is the sphere radius (i.e. the characteristic length), $q = \frac{2\pi a}{v_s^s} f$, and τ is a retarded time given by $\tau = \left(\frac{v_s^s}{a} \right) \left[t - \frac{r-a}{v_s^f} \right]$. The first term in Equation 1.9 determines the amplitude of the power spectrum, while the second dictates the location and shape of the spectral features. Unless otherwise stated, in the following discussion, $a = 5 \mu\text{m}$, $v_s^s = v_s^f = 1500 \text{ m/s}$, and $\rho_s = \rho_f = 1000 \text{ kg/m}^3$.

Of the four properties listed previously, the density of the droplet has the least significant effect on the power spectrum for small variations on the order of those observed in soft biological tissues. Figure 1.7a shows how the power spectrum of a droplet with $a = 5 \mu\text{m}$ and with density equal to that of the surrounding medium (i.e. $\rho_s = \rho_f$) changes when the droplet density is made 10% higher or lower than ρ_f . For these slight deviations

in density, there is only a slight change in the appearance of the side lobes in the power spectra; the location of the spectral minima remains unchanged. When considering water as a coupling medium $\rho_f = 1000 \text{ kg/m}^3$, this is equivalent to varying the density between 900 and 1100 kg/m^3 ; values which encompass a majority of densities for soft tissue in the body [73].

Next the effect of varying the speed of sound of the droplet is considered. Figure 1.7b shows that an increase of 10% of the sound speed (i.e. $\frac{v_s^s}{v_s^l} = 1.1$) results in a broadening of the location of all spectral minima. Expressing the location of the n -th spectral minima as f_n , the new locations are given by $f'_n = 1.1f_n$. Similarly, for a 10% decrease in the sound speed, there is a downshift of the location of the spectral minima described by $f'_n = 0.9f_n$. This also means that the shifts are larger at higher frequencies, as can be seen when comparing f'_1 and f'_2 in Figure 1.7b.

The effects of changing only the absorber size for a spherical droplet are the opposite of changing the speed of sound. In this case, increasing the cell radius by 10% results in a 10% decrease in the location of the spectral minima ($f'_n = \frac{f_n}{1.1}$). This is illustrated in Figure 1.7c. Using the dependence of the location of the spectral minima on the absorber diameter, it is possible to use quantitative PA to extract the diameter of gold nanoparticle loaded perfluorohexane droplets [78], and melanoma cells [87]. An attractive feature of quantitative PA techniques is the ability to size and differentiate between different types of biological cells without having to image them, by means of features in their power

spectrum [44,85,87–89]. However, to this point, no frequency domain analysis of sub-cellular structures with the aforementioned techniques has been performed.

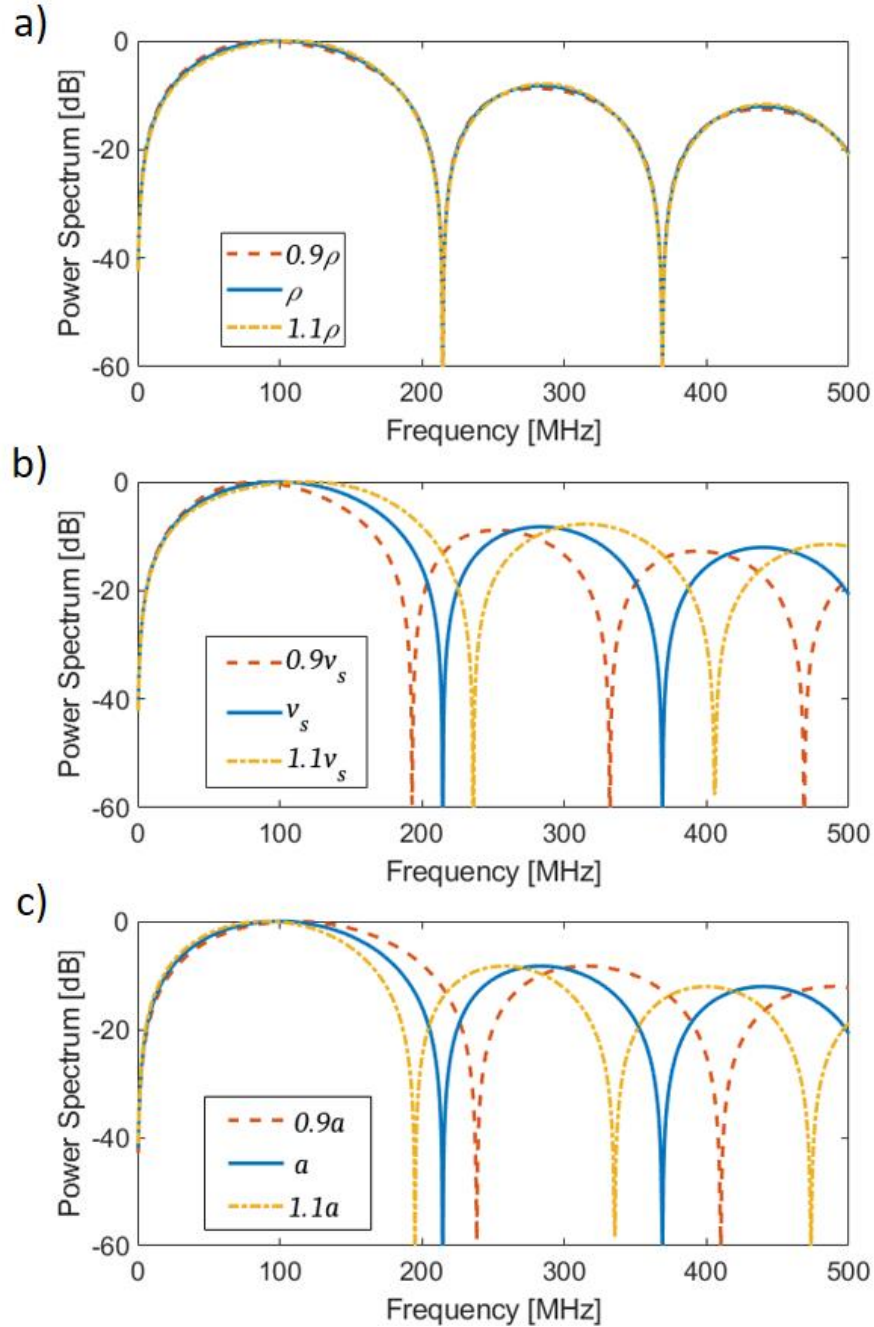


Figure 1.7: The effect which varying different parameters in Equation 1.9 has on the PA power spectra for a liquid sphere. The blue curve in each graph is identical, with the other curves showing changes in: a) the density, b) the speed of sound, c) the sphere radius.

1.5 Goals and Major Contributions

The goal of this project is to further develop analysis and imaging techniques for use in UHF-PAM studies of biological samples. The techniques presented in this dissertation can be divided into two categories. The first category uses frequency domain analysis of the broadband PA signals to ascertain morphological properties of single cells and their organelles (Chapter 2), and explores the use of unique features in the power spectra as a mechanism for image contrast (Chapter 3). The second category combines conventional PAM imaging with a novel imaging technique that is sensitive to a sample's optical attenuation properties; enabling simultaneous multimodal imaging of cells *in vitro* (Chapter 4) and zebrafish larvae *in vivo* (Chapter 5), based on the same acquired signal. These contributions enable new, non-optical means for determining the size of single biological cells and their nuclei, with potential applications in identification of cancerous cells by virtue of their morphology. The image reconstruction and acquisition techniques presented herein utilize contrast mechanisms never before applied in PAM imaging. They expand the sensitivity of PAM to absorbers of different scale, enable label-free imaging of biological specimens with little optical absorption, and can easily be integrated into conventional PAM systems with minimal modification to hardware or imaging workflow.

1.6 Overview of Dissertation

Chapter 2 provides a preliminary investigation on using frequency domain analysis techniques to determine the size of individual cancer cells and their nuclei using a PA contrast agent. The power spectra of the US waves backscattered from individual cells and the PA waves emitted from their dye stained nuclei were compared to analytical models to

extract the radius of the cell and nucleus, respectively. Using these values a nucleus-to-cytoplasmic ratio was calculated for each cell and compared to literature.

In Chapter 3, a novel PA frequency domain image formation technique (F-Mode) is presented. This approach is capable of generating images with contrast dictated by the sample's structure and spatial scale. To generate an F-Mode image, the power spectrum of each RF-Line in a PA scan dataset is partitioned into discrete frequency bands. The total power for a single band at each spatial location is then computed and used to generate a 2D F-Mode image. Each object in the scan has unique spectral features which are dependent upon its size, shape, and acoustic properties. The visibility of objects of different spatial scale can then be enhanced by selecting the F-Mode images which correspond to frequency bands that have maximum spectral power for one object, and minimal power for others. F-Mode imaging techniques are demonstrated on vessel phantoms, polystyrene beads, individual biological cells, and zebrafish larvae *in vivo*.

In Chapter 4 I present a new sensing technique (Photoacoustic Radiometry, PAR) which can be used simultaneously with PAM to generate images with contrast determined by the sample's optical attenuation properties. After being partially attenuated by the sample, the laser pulse used for PA signal generation impinges directly on the ultrasonic transducer, generating an additional PA wave within it. The amplitude of this secondary PA signal is dependent upon the amount of light transmitted through the sample, and thus is affected by *both* optical absorption and scattering. The simultaneous PAR and PAM imaging technique can be used to image samples with vastly different compositions

(biological, inorganic) and optical properties (opaque, transparent), and additionally can be combined with US imaging for triplex imaging capabilities.

Chapter 5 demonstrates simultaneous PAR/UHF-PAM imaging of zebrafish larvae *in vivo*. The PAR images allowed for visualization of the anatomical features of the optically transparent zebrafish (e.g. muscle segments, yolk sac), while UHF-PAM allowed for high-resolution 3D visualization of the zebrafish vasculature. The technique was used to image the head and trunk of transgenic and mutant zebrafish larvae, as well as larvae which had been exposed to an anti-angiogenic drug.

Chapter 6 summarizes all the results and suggests areas of future work. Appendices A and B provide supplementary information for Chapters 3 and 5, respectively.

Chapter 2

Assessment of the Nucleus-to-Cytoplasmic Ratio in MCF-7 Cells Using Ultra-high Frequency Ultrasound and Photoacoustics

2.1 Abstract

The nucleus-to-cytoplasmic (N:C) ratio of a cell is often used when assessing histology for the presence of malignant disease. In this proof of concept study, we present a new, non-optical method for determination of the N:C ratio using ultra-high frequency ultrasound (US) and photoacoustics (PA). When using transducers in the 100 MHz–500 MHz range, backscattered US pulses and emitted PA waves are encoded with information pertaining to the dimension and morphology of micron-sized objects. If biological cells are interrogated, the diameter of the scattering or absorbing structure can be assessed by fitting the power spectra of the measured US or PA signals to theoretical

This Chapter is based on an original article which has been published as:

M. J. Moore, E. M. Strohm, and M. C. Kolios, “Assessment of the Nucleus-to-Cytoplasmic Ratio in MCF-7 Cells Using Ultra-high Frequency Ultrasound and Photoacoustics,” *Int. J. Thermophys.*, vol. 37, no. 118, 2016.

models for US backscatter and PA emission from a fluid sphere. In this study, the cell and nucleus diameters of 9 MCF-7 breast cancer cells were determined using a new simplified model that calculates the theoretical values of the location of the power spectra minima for both US and PA signals. These diameters were then used to calculate the N:C ratio of the measured cells. The average cell diameter determined by US pulses from a transducer with a central frequency of 375 MHz was found to be $15.5 \mu\text{m} \pm 1.8 \mu\text{m}$. The PA waves emitted by the cell nuclei were used to determine an average nuclear diameter of $12.0 \mu\text{m} \pm 1.3 \mu\text{m}$. The N:C ratio for these cells was calculated to be 1.9 ± 1.0 , which agrees well with previously reported N:C values for this cell type.

2.2 Introduction

Cancer is one of the leading causes of death worldwide, claiming the lives of over 8.2 million people in the year 2012 [90]. The current gold standard for diagnosis of cancerous disease is histological assessment of a biopsy sample via optical microscopy [91]. One of the most prominent features of cancerous cells is an enlarged nucleus due to an atypically large amount of chromatin. The nucleus-to-cytoplasmic (N:C) ratio, defined as the ratio of the cross-sectional area of the nucleus divided by that of the cytoplasm, is a commonly used parameter in tumor staging and grading. Historically the N:C ratio has been assessed qualitatively by pathologists using optical microscopy; however, in recent years several quantitative methods utilizing image recognition software and digital post-processing have been developed to automate the process [92–95]. Even with these advances, the assessment of the cell N:C ratio may be difficult due to the thin tissue samples typically examined. For example, if the tissue slice is not taken through the plane

of the cell which exhibits the largest nucleus cross-section, stereological methods must be used to infer the maximum possible nucleus diameter and calculate the N:C ratio. To remediate this, 3D imaging techniques can be used to fully assess cellular and nuclear morphology. Balasubramanian et al. [96] examined circulating tumor cells with confocal microscopy and were able to differentiate malignant and benign cells by their N:C ratios and cytokeratin expression profiles. Nandakumar et al. [97] used the Cell-CT device to obtain 3D images of breast cancer cells and calculate N:C ratios without having to stitch together multiple planar images as in confocal microscopy. However, due to the lengthy imaging time of one cell per minute [98], the Cell-CT device is not suited to the analysis of large cell populations.

A more rapid determination of cell and organelle morphology is possible with flow cytometry (FC) techniques. In conventional FC, forward scattered light is correlated with overall cell size and side scattered light with the cell granularity; however, exact morphological dimensions are not obtained. On the other hand, imaging flow cytometry (IFC) can be used to simultaneously acquire brightfield, darkfield, and fluorescence images of suspended cells at a rate of several hundred cells per second [99–101]. Basiji et al. [101] used the ImageStream IFC system to analyze both normal mammary epithelial cells and mammary carcinoma cells, finding that while the cellular and nuclear areas of the analyzed normal and carcinoma cells was similar, on average the cytoplasmic area of the carcinoma cells was substantially lower than that of the normal cells. In contrast to the *in vitro* FC and IFC techniques, photothermal flow cytometry (PTFC) and photoacoustic flow cytometry (PAFC) can both be used to interrogate cells *in vivo*. Zharov et al. have used

PTFC for high throughput *in vivo* imaging of unlabeled erythrocytes and leukocytes in the blood and lymph [102–104]. PAFC on the other hand has been used for the *in vivo* detection of unlabeled circulating melanoma cells as well as breast cancer cells labeled with gold and magnetic nanoparticles [105–108]. While these techniques have the clear advantage of speed, they share disadvantages with standard 2D imaging modalities as they do not inherently assess 3D structure.

Recently, ultra-high frequency ultrasound (US) and photoacoustic (PA) methods have been used to assess the morphological structure of single cells [31,44,109]. At frequencies in the hundreds of megahertz (MHz), the wavelength of the incident US pulse is on the order of the cell diameter, and backscattered US waves contain information about cell size and morphology. This information has previously been extracted from various cell types, including melanoma cells, leukocytes, and erythrocytes [87,110]. A similar phenomenon occurs in PA; when irradiated by a laser, waves generated by the transient thermoelastic expansion are encoded with information pertaining to the size and morphology of the optically absorbing structure [77,79]. Deviations in these PA signals have been used to monitor the change in erythrocyte morphology as a function of the osmolality in the surrounding fluid [85]. In mouse melanoma cells, where the acoustically scattering and optically absorbing volumes are similar, the cell size calculated from backscattered US pulses was found to be in good agreement with cell size extracted from PA signals generated by melanin particles within the cell cytoplasm [87].

In this study, a new mathematical formulation is derived to extract morphological information from the unique features in the US and PA power spectra. This formulation

was used to obtain the diameter of MCF-7 breast cancer cells from backscattered ultra-high frequency US pulses and the diameter of the MCF-7 cell nuclei using PA signals originating from the nucleus. These two measurements, when performed on the same cell, can be used to rapidly determine the N:C ratio without the need for optical assessment or stereology.

2.3 Theory

2.3.1 Acoustic Scattering by a Fluid Sphere

Biological cells in suspension are approximately spherical and, being composed predominantly of water, have elastic properties determined by their cytoplasm [111]. The theory describing scattering of an acoustic wave by a fluid-filled sphere immersed in liquid was first developed by Anderson in 1950 [112]. In subsequent years, Frey and Goodman simplified the Anderson model for the case of a weakly scattering sphere, i.e., a fluid sphere with acoustic properties approximately the same as those of the surrounding liquid. In this case, the displacement potential arising from the backscattered pulse is given by [113]:

$$\phi(k) = -\frac{\exp(-ikr)}{2kr} (ka)^2 (\epsilon + \delta) j_1(2ka) \quad (2.1)$$

where $j_1(z)$ is a spherical Bessel function of the first kind of order one, a is the radius of the fluid sphere, k is the wavenumber of the incident US pulse, r is the distance between the sphere and point at which the acoustic wave is assessed, and ϵ and δ are the percent differences between the bulk moduli and density of the sphere fluid and surrounding liquid, respectively. Writing Equation 2.1 in terms of frequency, it can be shown that the

location of minima and maxima in the power spectrum of the backscattered wave are predicted by the zeros and maxima of

$$\Phi(f) = j_1\left(\frac{4\pi a}{v_s}f\right), \quad (2.2)$$

where v_s is the longitudinal speed of sound within the sphere and f is the frequency. Thus, if the speed of sound within a weakly scattering sphere, e.g., a cell, is known, the radius of the sphere may be approximated by fitting the maxima and minima in the experimentally measured power spectrum to Equation 2.2.

2.3.2 Photoacoustic Signal from a Spherical Absorber

As the acoustic properties of a fluid sphere approach those of the surrounding medium, the PA wave produced by the sphere attains a characteristic N-shape described by [114]:

$$p(t) = \frac{r + v_s t}{2r} p_o(r + v_s t) + \frac{r - v_s t}{2r} p_o(-r + v_s t) + \frac{r - v_s t}{2r} p_o(r - v_s t) \quad (2.3)$$

where a , v_s , and r are as defined as in the previous section, and $p_o = p_i U(r) U(-r + a)$; where $U(r)$ is the Heaviside function and p_i is the initial pressure within the sphere. For times $t > \frac{a}{v_s}$ after laser absorption, Equation 2.3 can be written as

$$p(t) = \frac{(r - v_s t)}{2r} p_i \Pi\left(\frac{v_s}{2a}\left(t - \frac{r}{v_s}\right)\right), \quad (2.4)$$

where $\Pi(x)$ is the rect function. An expression for the pressure in the frequency domain of the waveform described by Equation 2.4 is obtained via the convolution theorem as follows. The Fourier transform of the first term in the product is

$$\mathcal{F}\left\{\frac{(r - v_s t)}{2r}\right\}(f) = \frac{\delta(f)}{2} - \frac{iv_s}{4\pi r} \frac{d\delta(f)}{df} \quad (2.5)$$

where $\delta(f)$ is the Dirac delta function. The Fourier transform of the second term is

$$\mathcal{F}\left\{p_i \Pi\left(\frac{v_s}{2a}\left(t - \frac{r}{v_s}\right)\right)\right\}(f) = \frac{p_i \exp\left(-\frac{i2\pi r}{v_s} f\right) \sin\left(\frac{2\pi a}{v_s} f\right)}{\pi f} \quad (2.6)$$

Convolution of Eq's. 2.5 and 2.6 yields

$$P(f) = -\frac{p_i v_s i}{4\pi^2 f^2 r} \exp\left(-\frac{i2\pi r}{v_s} f\right) \left(\frac{2\pi a f}{v_s} \cos\left(\frac{2\pi a}{v_s} f\right) - \sin\left(\frac{2\pi a}{v_s} f\right)\right), \quad (2.7)$$

which is equivalent to the simplified model derived by Diebold and Westervelt for the case of a fluid droplet with acoustic properties identical to those of the surrounding liquid [82], that can be obtained by setting $v_s^s = v_s^f$ and $\rho_s = \rho_f$ in Eq. 1.9. Using the identity

$$j_1(z) = \frac{\sin(z)}{z^2} - \frac{\cos(z)}{z} \quad (2.8)$$

Equation 2.7 can be rewritten in terms of spherical Bessel functions as

$$P(f) = \frac{ip_i a^2}{v_s r} \exp\left(-\frac{i2\pi r}{v_s} f\right) j_1\left(\frac{2\pi a}{v_s} f\right). \quad (2.9)$$

The radius of optically absorbing liquid spheres can be determined by fitting the power spectra of emitted PA waves to Equation 2.9.

2.4 Methods

2.4.1 Preparation of the sample

MCF-7 cells were cultured in phenol red-free Dulbecco's Modified Eagle's Medium (DMEM) containing 10% fetal bovine serum by volume. When confluent, cells were trypsinized and resuspended in DMEM. The suspension was incubated in the dark at room temperature for 15 min with DRAQ5, a supravital fluorescent dye used to stain cell nuclei. The absorption of visible light by cell nuclei is negligible; however, DRAQ5 absorbs within the visible spectrum and facilitated the generation of PA signals from the cell nuclei. The stained MCF-7 cells were then suspended in a DMEM solution containing 16% HEPES buffer solution by volume and transferred to a glass-bottomed petri dish (MatTek, USA). A thin layer of 1% agar was deposited onto the glass-bottomed dish and allowed to solidify prior to addition of the cells, ensuring that acoustic reflections from the glass did not interfere with forward traveling acoustic waves. The petri dish containing the cells was placed in a climate-controlled enclosure at 37°C and was allowed to equilibrate with the ambient temperature before measurement.

2.4.2 System Setup and Measurement

A modified scanning acoustic microscope (Kibero GmbH, Germany) consisting of an inverted optical microscope and translation stage was outfitted with a pulsed 532 nm laser and high-frequency US transducer. The laser had a 330 ps pulse width and 4 kHz repetition rate (Teem Photonics Inc., France), and the ultrasonic transducer had a central frequency of 375 MHz with a -6dB bandwidth of 150 MHz (Kibero GmbH, Germany). The laser was directed into the microscope optical path and focused onto the sample cells by a

10X optical objective (Olympus, Japan). The theoretical -6dB acoustic beam diameter at the transducer focus was approximately $4\ \mu\text{m}$ [32], while the $1/e^2$ diameter of the objective focused Gaussian laser beam was approximately $2\ \mu\text{m}$ [115]. During measurement, the optical objective was slightly defocused to a size of approximately $10\ \mu\text{m}$ to allow irradiation of the entire cell nucleus. The transducer was coaxially aligned to the optical objective on the opposing side of the sample. For each interrogated cell, the backscattered US signals from the cell were recorded first, and then, PA signals were acquired from the nucleus. A schematic of the system and a cross-sectional view through the microscope optics are shown in Figure 2.1.

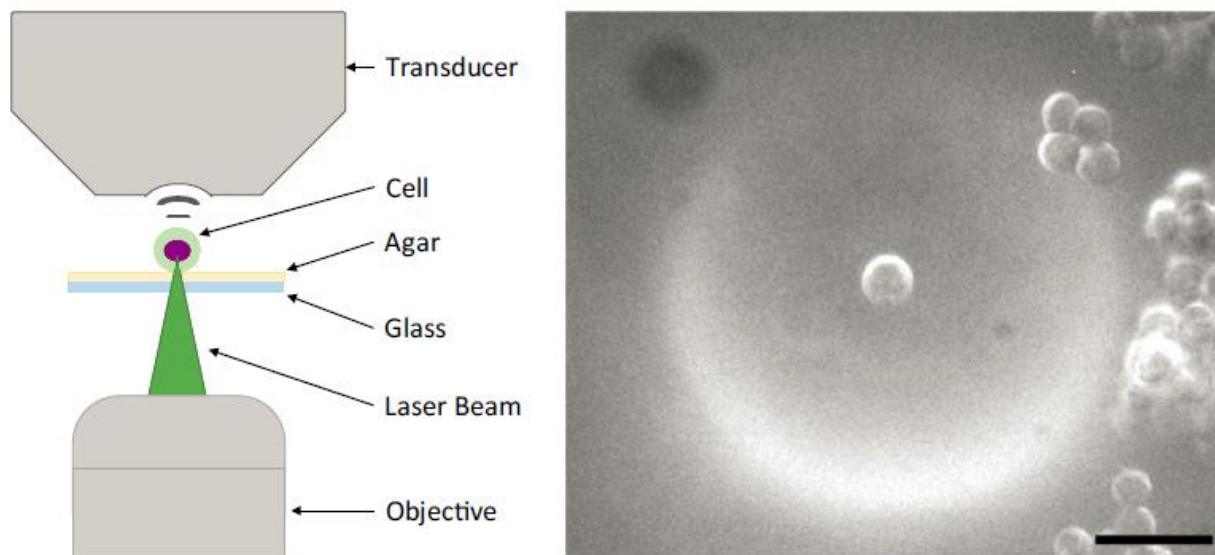


Figure 2.1: *Left* Schematic of the experiment setup. *Right* Optical image of a suspended MCF-7 cell, with the transducer cavity faintly visible in the background. The scale bar is $40\ \mu\text{m}$.

2.4.3 Signal Processing

Acquired US and PA A-lines were digitized using a 10-bit digitizer with an 8 GHz sampling frequency (DC252, Acqiris, USA). Acquired A-lines were averaged 200 times to

increase the signal-to-noise ratio (SNR). In general, performing an average of N signals increases the SNR by a factor of \sqrt{N} , thus, the signal averaging done here is equivalent to increasing the SNR of the A-lines by a factor of approximately 14. The A-lines were then time-gated so that they contained only the desired signal from the cell. A Hamming window with length equal to that of the time-gated signal was applied prior to zero-padding and Fast Fourier Transformation of the signal in MATLAB. A peak detection algorithm was used to locate maxima and minima in the normalized power spectra. These extrema were then used to determine a set of possible values for the radius, a , using Equations 2.2 and 2.9 for the cell and nucleus, respectively. The value of a that yielded the theoretical fit with the lowest root mean square error compared to the measured spectra was taken as the radius. In the fitting process it was assumed that the speed of sound was $1575 \text{ m}\cdot\text{s}^{-1}$ for all measured cells [116]. Finally, the N:C ratio was calculated as:

$$N:C = \frac{N}{C - N}, \quad (2.10)$$

where N is the cross-sectional area of the nucleus and C is the cross-sectional area of the cell. All cross-sectional areas were calculated based on the radii obtained by the fitting algorithm.

2.5 Results and Discussion

For this proof of concept study, 9 cells were interrogated: first with US and subsequently with PA. All measured signals were fit using the algorithm described in the previous section. Representative measured US and PA signals acquired from the same cell as well as the corresponding calculated and fit power spectra are shown in Figure 2.2.

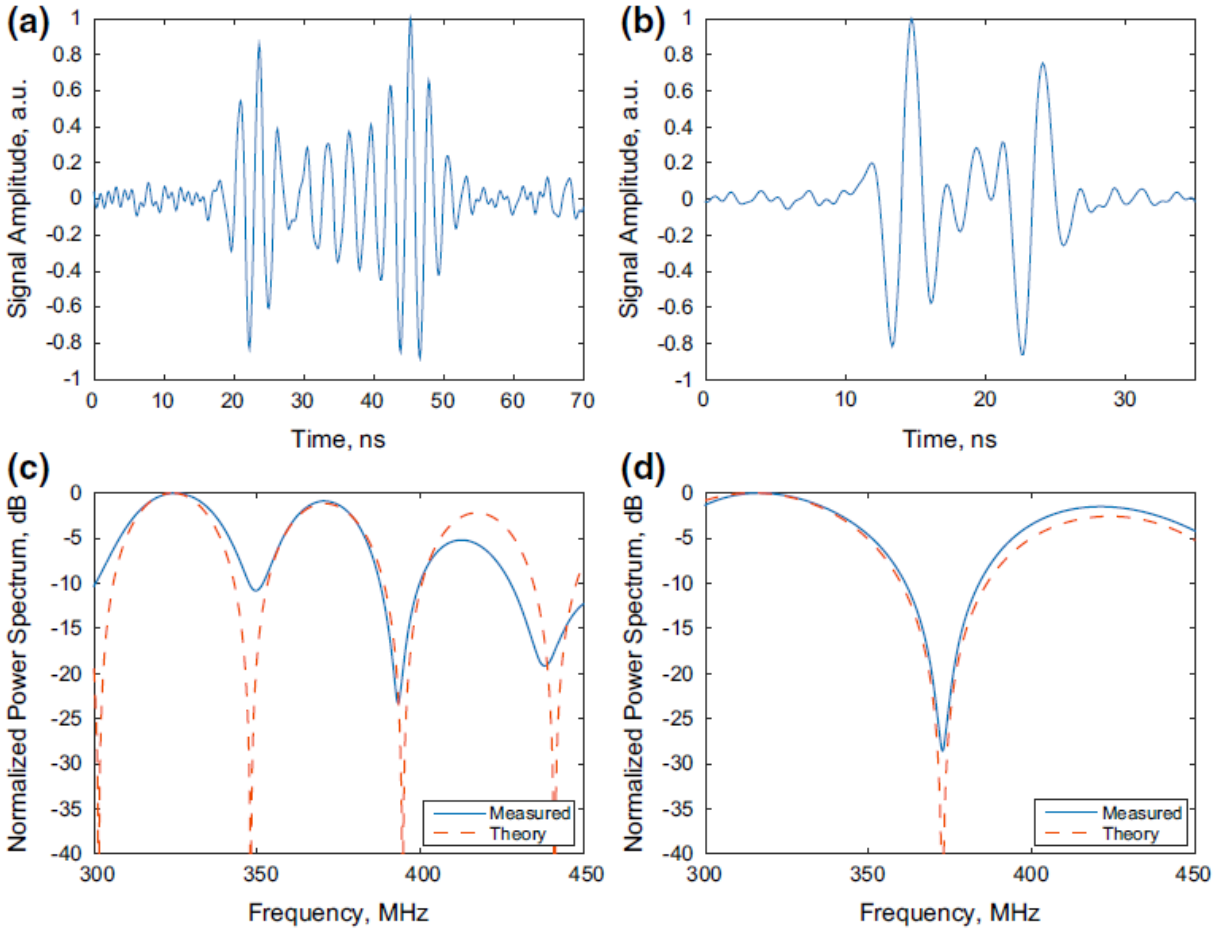


Figure 2.2: Measured A-lines from an US pulse backscattered by a cell (a) and PA signal emitted by the nucleus of the same cell (b). The power spectra of the backscattered US pulse and the best-fit spectrum generated using Equation 2.2 and photoacoustic signal and the fit power spectrum of Equation 2.9 are shown in (c, d), respectively. The power spectra were windowed to match the transducer bandwidth.

The US and PA spectral fitting techniques described in this work are sensitive to the assumed speed of sound within the cell and nucleus, respectively. The locations of the extrema predicted by Equations 2.2 and 2.9 are unique with respect to the argument a/v_s . Therefore, for a fixed value of v_s , there exists only one a which will yield the detected extrema in the measured signal power spectrum. Thus, there is an intrinsic uncertainty in a due to uncertainty in the assumed value of v_s . In previous studies, the standard deviation

in the speed of sound of MCF-7 cells throughout various phases of their cell cycle was found to be less than 1.5% of the mean calculated sound speed [116,117]. Therefore, an unstated uncertainty of 1.5% in each of the calculated values of a in this work can be assumed.

The time-domain US signal and its power spectrum are shown in Figure 2.2a and 2.2c, respectively, along with the closest matching analytical solution fit using Equation 2.2. Good agreement is observed between the locations of the spectral minima and maxima in both the measured and analytical power spectra. The average cell diameter determined using the US backscatter fitting process was $15.5 \mu\text{m} \pm 1.8 \mu\text{m}$. This is in good agreement with the reported MCF-7 cellular diameter of $16.2 \mu\text{m} \pm 3.0 \mu\text{m}$ found by Reile et al. [118]. Other studies have reported larger average MCF-7 diameters of $18 \mu\text{m} \pm 2.0 \mu\text{m}$ [119] and $19.1 \mu\text{m} \pm 8.4 \mu\text{m}$ [120]. Factors such as the type of growth medium and number of passages may be responsible for the variation in the reported MCF-7 diameters.

The PA power spectrum in Figure 2.2d was obtained by applying a Fourier transform to the measured PA signal shown in Figure 2.2b. The best-fit power spectrum generated using Equation 2.9 is shown in orange in Figure 2.2d. The average nucleus diameter as determined by fitting of the PA spectra originating from the stained nuclei was $12.0 \mu\text{m} \pm 1.3 \mu\text{m}$, which is comparable to the value of $9.2 \mu\text{m} \pm 2.9 \mu\text{m}$ reported by Dahle et al [121]. The average calculated N:C ratio calculated using Equation 2.10 was 1.9 ± 1.0 . This is in good agreement with the published N:C value of 1.8 ± 0.2 for the MCF-7 cell line [122]. For cells with an N:C ratio of 1.9, 53% of the cell volume is occupied by the

nucleus. In comparison, the nucleus of eukaryotic cells typically occupies 10% of the total cell volume [123].

In this proof of concept study, the cell size, nucleus size, and N:C ratio of MCF-7 breast cancer cells were calculated by comparing measured US and PA power spectra to simplified theoretical equations. This measurement method could aid pathologists in detection and classification of malignant and non-malignant cells in a blood or biopsy sample

2.6 Conclusion

A method for assessing the size of cells and cell nuclei as well as the N:C ratio using high-frequency US and PA has been developed. Simple analytical solutions were derived for the rapid determination of the US and PA signal power spectra minima and maxima. The mean cell and nucleus diameter for MCF-7 cells were calculated to be $15.5 \mu\text{m} \pm 1.8 \mu\text{m}$ and $12.0 \mu\text{m} \pm 1.3 \mu\text{m}$, respectively. The mean calculated N:C ratio of 1.9 ± 1.0 was consistent with other published data. In the future, this technique, which does not require optical imaging of sample cells, will be integrated into the software of a US/PA flow cytometer [124] and used to analyze blood samples for the presence of cancerous cells.

2.7 Acknowledgements

The authors would like to thank E. Berndl (Ryerson University) for her assistance with biological cell culturing. This research is supported in part by the Natural Sciences and Engineering Research Council of Canada, the Canadian Cancer Society, the Canadian Foundation for Innovation, and the Ontario Ministry for Research and Innovation.

Chapter 3

Photoacoustic Frequency Mode (F-Mode) Imaging: Scale-specific Contrast from Organelles to Organisms

3.1 Abstract

In photoacoustic (PA) imaging, time domain reconstruction techniques are the current gold standard for image formation. While these techniques provide high-resolution spatial maps of optical absorption, they neglect the abundance of structural information encoded in the frequency domain of the inherently broadband PA signals. In this work, we introduce a new frequency domain technique for PA image formation, termed F-Mode. By leveraging information contained in the frequency content of emitted PA signals, F-Mode can be used to generate images with scale-specific contrast. To demonstrate the robustness of our technique to system configuration, we apply F-Mode

This Chapter is based on a manuscript which has been submitted for publication as:

M. J. Moore, E. Hysi, M. N. Fadhel, S. El-Rass, Y. Xiao, X-Y. Wen, M. C. Kolios, “*Photoacoustic Frequency Mode (F-Mode) Imaging: Scale-specific Contrast from Organelles to Organisms*,” (Submitted for publication, *Communications Physics*, June 2018).

analysis to datasets acquired using both PA tomography and PA microscopy systems, utilizing linear array and single-element transducers with central frequencies ranging from 40 – 400 MHz. We show that the technique can be used to: differentiate between vessels and microspheres of different size in phantoms, enhance visualization of organelles in *in vitro* cultured cells, and selectively display single blood vessels *in vivo* in zebrafish larvae.

3.2 Introduction

Since its discovery by Alexander Graham Bell late in the 19th century [2], the photoacoustic (PA) effect has found many applications in fields ranging from spectroscopy [125], to non-destructive testing [126], and most recently, biomedicine [5,6,18,127,128]. The endogenous absorption of abundant biomolecules - including hemoglobin, melanin, and DNA - has enabled label-free imaging of complex biological structure ranging from nanometers to centimeters in scale. At opposite ends of this spectrum are the techniques of Photoacoustic Microscopy (PAM), which offers sub-cellular resolution that facilitates imaging of individual organelles including cell nuclei, melanosomes, and mitochondria [31,46,129]; and Photoacoustic Tomography (PAT), which is capable of non-invasive *in vivo* imaging of mouse organs [130,131] as well as human breast [16,19] and skin cancers [20].

The emission of a PA wave from an object occurs subsequent to optical excitation and non-radiative relaxation. After emission, PA waves are analogous to the mechanical waves employed in ultrasound (US) imaging. As such, there are numerous similarities between the two imaging techniques; including the use of ultrasonic transducers for the conversion of mechanical waves to electrical signals (henceforth referred to as RF-Lines),

and the algorithms used for image reconstruction. In addition to conventional US image reconstruction techniques (for example: B-Mode [132] and M-Mode [133]), the maximum amplitude projection (MAP) technique is widely used in PA imaging, especially in PAM. As the name implies, in MAP, the maximum value of the envelope of the RF-Line acquired at each spatial location is projected onto a 2D space for image formation. This technique produces striking spatial maps of chromophore distribution, but due to the nature of MAP, contains no information in the axial direction.

The aforementioned image reconstruction techniques are implemented in the time domain, and are heavily dependent upon the characteristics of the system and transducer used for acoustic detection. In general, PA systems can be regarded as being linear-time invariant (LTI), and thus, the detected PA signal can be expressed as a convolution of the emitted PA wave with the transducer impulse response [134,135]. However, this convolution causes distortion of the temporal profile in the resultant RF-Line due to the finite transducer bandwidth. This decreases the sensitivity to slight variations in absorber size and shape (Figure A.1) and presents a challenge when attempting to differentiate structures with comparable morphology. However, these variations in morphology, which would otherwise be undetectable in the time domain, are readily detected using spectral features in the frequency domain representation of the recorded PA signals [77,79] (Figure A.1). It has been demonstrated that this frequency encoded information readily lends itself to quantitative analysis techniques [31,85]. In particular, analysis of the power spectrum of acquired RF data at ultra-high frequencies (greater than 100 MHz) has enabled studies of the size and shape of both inorganic [78,80,82,136] and biological [85,87,88]

samples. Quantitative frequency domain analysis of PA signals acquired at lower ultrasonic frequencies (less than 100 MHz) has been used for monitoring tumour response to cancer therapy [137], and assessing red blood cell aggregation [138].

We hypothesized that these unique spectral signatures could be further leveraged for frequency based image reconstruction, analogous to the parametric images used for defect detection in scanning acoustic microscopy [139]. By appropriately subdividing the power spectra of the RF data into bands, spectral features within the divisions can be isolated and used as a mechanism for generating image contrast. Displaying the contents of one such band at each location in the scan dataset results in images that are highly sensitive to small deviations in object size and shape. Furthermore, due to the inherently broadband nature of photoacoustic signals, rich contrast can be achieved over many length scales. Adopting the nomenclature from traditional US techniques, we have termed these images ‘frequency mode’ or F-Mode images.

In this work we introduce the F-Mode technique and apply it to data acquired using both PAT and PAM imaging systems. We show the robustness of F-Mode over a wide range of transducer configurations and central frequencies, ranging from pre-clinical linear array transducers (40 MHz) to ultra-high frequency single element transducers (400 MHz). We then demonstrate the ability of the technique to selectively isolate structures spanning orders of magnitude difference in scale, including: macrovasculature mimicking vessels in a phantom, individual organelles in cultured biological cells, and perfused blood vessels in a live zebrafish larva.

3.3 Description of the F-Mode Technique

In this section we detail the steps required for the generation of F-mode images. This methodology is identical for both PAT and PAM implementations. A diagrammatic overview of the technique is provided in Figure 3.1. First, each RF-line of length l in a three dimensional PA dataset of size $l \times m \times n$ is converted to its frequency domain representation via the Fast Fourier Transform (FFT). The number of points, $K \in N$, in the FFT is set to be:

$$K = \frac{f_s}{\Delta f}, \quad (3.1)$$

where f_s is the system sampling frequency, and Δf is the desired resolution of the resultant frequency domain spectrum. The corresponding power spectra are then computed, and partitioned into Q discrete frequency bands with length equal to an integer multiple of Δf . The total power in each band is then calculated via summation, and stored in a vector of length Q .

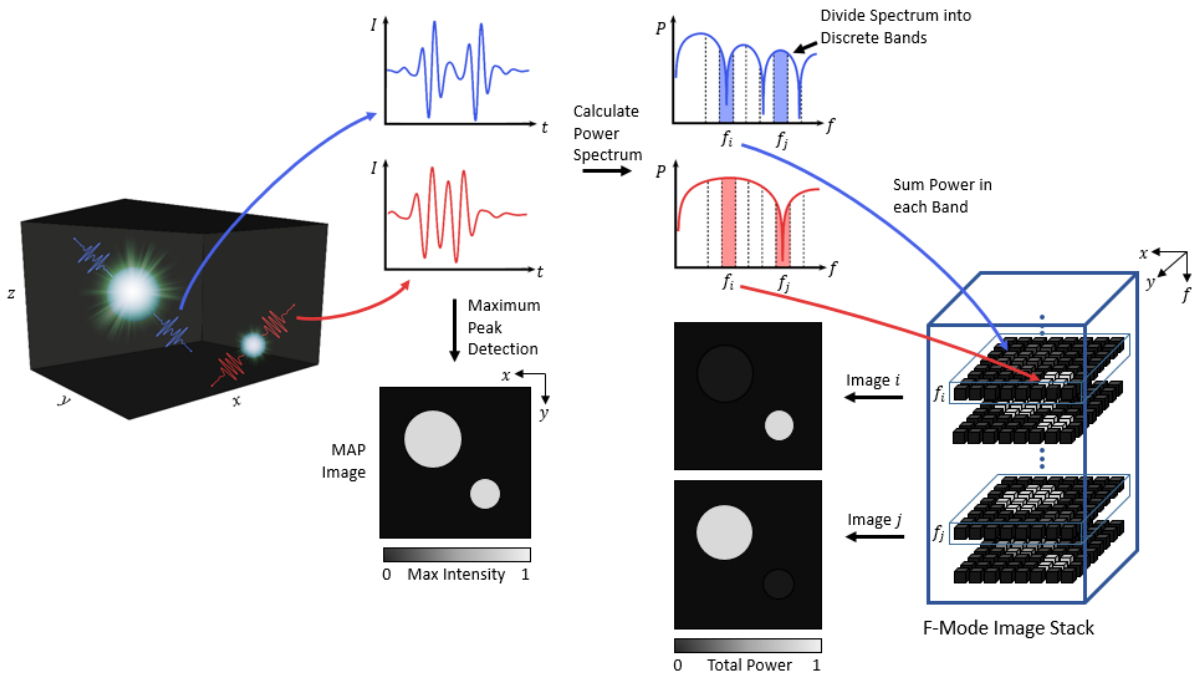


Figure 3.1: An overview of the F-Mode technique. Photoacoustic waves are generated due to laser absorption and subsequent non-radiative relaxation. The blue waveform is from the large sphere and the red is from the small sphere. Recorded time domain signals can be used directly to create a MAP image. In the F-Mode technique, the power spectrum of each RF signal is computed and divided into discrete frequency bands of uniform spectral width. The power within each band is added at each spatial coordinate and stored in an array, preserving spatial organization. Each row in the array can be used to form an independent F-Mode image. Depending on the spectral features in the selected frequency band, objects of certain size will exhibit enhanced contrast in some bands, while being nearly indistinguishable from the background in others.

Applying this algorithm to each RF-line in the dataset results in a new array of size $Q \times m \times n$, which can be thought of a stack of Q distinct F-Mode images, each of size $m \times n$. The intensity of a given pixel in an F-Mode image is determined by the relative magnitude of its summed power in relation to all other pixels within the same band. For this reason, each F-Mode image has a unique dynamic range, with signal to noise ratio (SNR) robust to large changes in transducer sensitivity. In each F-Mode image, pixels from an object which exhibit minima in a selected frequency band may be indistinguishable from the

background, effectively concealing the object while greatly enhancing the visibility of the objects that remain. However, due to the oscillating power spectra (Figure 3.1), these same pixels may contain the highest summed power in a different frequency band, and hence will be the brightest pixels in the corresponding F-Mode image. The contrast of a pixel within a given object is thus constantly changing with respect to pixels from other objects. Animations created from the entire F-Mode image stack provide visual displays of the local power as a function of frequency (Movie A.1) and can be used to display the size specific contrast dynamically.

3.4 Methods

3.4.1 Photoacoustic Tomography System

The commercially available VevoLAZR (Fujifilm-VisualSonics, Toronto, Canada) was used for all PAT measurements. The system was equipped with the LZ550 probe, which has central frequency and -6dB bandwidth of 40 MHz and 15 MHz, respectively. A pulsed OPO laser with a Nd:YAG pump and 20 Hz pulse repetition frequency (PRF) was tuned to a wavelength of 710 nm and used to illuminate the sample. Signal acquisition was performed at a sampling frequency of 1064 MHz, and RF data was averaged 4 times to increase SNR. The raw recorded PA data was beamformed offline in MATLAB using a standard delay and sum algorithm. All measurements were performed at room temperature, with deionized water to provide acoustic coupling.

3.4.2 Photoacoustic Microscopy System

A modified SASAM scanning acoustic microscope (Kibero, Saarbruken, Germany) was used for all PAM measurements. The SASAM is customizable, and allows major system components (e.g. transducer, focusing objective, laser source) to be interchanged. In these experiments, two lasers were used: a 532 nm Nd:YAG laser (Teem Photonics, Meylan, France), operating at a PRF of 4 kHz with a pulse width of 330 ps; and a UV Nd:YAG laser (Bright Solutions, Pavia, Italy) with wavelength of 266 nm, PRF of 10 kHz, and pulse width of 500 ps.

When the 532 nm laser was used, the laser was attenuated using a variable neutral density filter (Thorlabs, New Jersey, USA) and coupled into an optical fiber (Coastal Connections, California, USA). The fiber output was collimated using a fiber coupler (Schafter + Kirchhoff, Hamburg, Germany), directed off a dichroic mirror (Chroma Technology, Vermont, USA), and focused through a 10X optical objective (Olympus, Tokyo, Japan) onto the sample. For the 266 nm illumination pathway, the laser was first directed through a beam expander to increase the beam width. This laser emits both 266 nm and 532 nm beams collinearly, thus the 266 nm wavelength was isolated using a 4th harmonic Nd:YAG laser line mirror (Thorlabs, New Jersey, USA). The UV beam was directed into a dichroic mirror (Chroma Technology, Vermont, USA) and focused onto the sample using a 10X UV objective (Thorlabs, New Jersey, USA).

One of three different single element transducers (Kibero, Saarbruken, Germany) was used to record the PA waves: an 80 MHz transducer with -6 dB bandwidth of 90 MHz, a 200 MHz transducer with -6 dB bandwidth of 120 MHz, or a 400 MHz transducer

with -6dB bandwidth of 180 MHz. All recorded PA signals were digitized at a rate of 8 GS/s with a 10-bit digitizer (Aquiris, USA). Signal averaging for the 80, 200, and 400 MHz transducer was performed at 400, 200, and 100 times, respectively. Unless otherwise stated, all PAM experiments were performed at 37°C, with acoustic coupling provided by 1X PBS.

3.4.3 The F Mode Algorithm

Acquired RF data was imported into MATLAB for processing. The RF datasets were transformed into their frequency domain representations by applying the MATLAB 1D Fast Fourier Transform (FFT) to each individual RF-line. The RF-Lines were zero padded to a length of $K = \frac{f_s}{1E5}$, where f_s is the sampling frequency of the system used for signal acquisition, to ensure that the spacing between points in the transformed spectrum was equal to 100 kHz. To satisfy Parseval's theorem, the frequency spectra were then scaled by a factor of $\frac{1}{f_s}$. The signal power spectrum was then estimated by taking the squared magnitude of the scaled frequency spectrum. An F-Mode matrix was generated by partitioning each power spectrum into discrete spectral bands and computing the total power in each band for every spectrum. Due to the large difference in transducer bandwidths, a spectral band size of 0.2 MHz was used for the PAT acquired data, and a band size of 1 MHz was used for the PAM data.

3.4.4 Preparation and Imaging of Vessel Phantom

For the VevoLAZR experiment, a gelatin phantom composed of 10% (w/v) porcine skin gelatin was prepared. Briefly, the gelatin powder was slowly added to degassed water

which had been heated to 35°C. The mixture was magnetically stirred until it reached 65°C and the gelatin was entirely dissolved. The molten gelatin mixture was then poured into a custom-made mold containing three taught fishing lines with diameters of 250, 200, and 150 μm , respectively, and was kept at 4°C for 24 hours. Prior to imaging, the fishing lines were gently removed and the cavities filled with a 70% (v/v) ethanol in water mixture containing Sudan Black B (Sigma-Aldrich Canada, Oakville, Canada).

The vessel phantom was scanned with a 40 MHz central frequency linear array transducer (LZ550) probe. The imaging plane was oriented orthogonally to the long axis of the vessels. The resultant PA data was beamformed using MATLAB, and the F-Mode algorithm was applied. A representative F-Mode spectrum from each vessel was used to identify the spectral bands which exhibited the greatest contrast between the vessels.

3.4.5 Preparation and Imaging of Bead Phantom

A glass bottom petri dish (MatTek, Massachusetts, USA) was filled with 300 μL of molten 0.5% (w/v) low melting point agarose (Sigma Aldrich, USA) dissolved in PBS. The agarose was allowed to solidify in the dish for 30 minutes at room temperature. In the meantime, 1 mL of molten agarose was pipetted into an aliquot along with 2 μL of PBS solution containing black polystyrene microspheres with 6 μm diameter (Polysciences, USA), and 2 μL of another PBS solution containing black polystyrene microspheres with 10 μm diameter (Polysciences, USA). The aliquot was vortexed, and then 40 μL of the bead laden agarose was pipetted on top of the solidified agarose layer in the petri dish. The dual layer phantom was allowed to cool for 20 minutes at 4°C. The sample was raster scanned with the SASAM using the 400 MHz transducer and the 532 nm laser. For display purposes,

the spectra shown in Figure 3.3c were smoothed using a lowpass filter to remove high frequency oscillations due to the system response.

3.4.6 Culturing and Imaging of CAKI-2 Cells

The coverslip of a glass-bottom petri dish (MatTek, Massachusetts, USA) was removed and a UV-Grade fused silica cover slip (Esco Optics, New Jersey, USA) was epoxied in its place. The epoxied cover slip was coated with Poly-D-Lysine prior to cell plating to promote cellular adhesion. Briefly, 1 mL of Poly-D-Lysine was pipetted onto the cover slip surface. After 5 minutes, excess Poly-D-Lysine was rinsed off using deionized water and the dish was allowed to dry for 2 hours. CAKI-II cells were then plated, covered with 2 mL of McCoy's 5A media, and were allowed to adhere to the substrate overnight. Prior to scanning, the cell media was aspirated, and the dish was flooded with 2 mL of ice cold methanol for 3 minutes. The sample was finally rinsed twice with 2 mL of Milli-Q water immediately before imaging. The cells were scanned in the SASAM with the 200 MHz transducer and 266 nm laser in a raster pattern, with a fast and slow step size of 1 μm . For display purposes, the transducer response of the 200 MHz transducer was smoothed using a lowpass filter to remove high frequency oscillations due to the system response. Both the MAP and F-Mode images created from the resultant dataset were smoothed using a 2D 2 point averaging filter, and interpolated using 2D 1 point linear interpolation.

3.4.7 Preparation and Imaging of Zebrafish Larvae

Five day-post-fertilization mutant casper zebrafish larvae were anesthetized using a 0.003% (w/v) solution of tricane (Sigma, Cat. #A5040) and pipetted into a solution of

molten 1.5% (w/v) low melting point agarose in PBS at 40°C. A glass-bottom petri dish coated with a flat layer of 1.5% (w/v) agarose was prepared as in the previous section. A drop of the molten agarose was pipetted onto the dish along with the anesthetized larva. A pipette tip was used to position the specimen in the still molten agarose so that the sagittal plane of the fish was visible under optical microscopy. Once the larva was correctly positioned, the agarose was allowed to solidify for 30 minutes at room temperature. The dish was then filled with approximately 4 mL of egg water, and scanned using the 80 MHz transducer and the 532 nm laser focused through a 4X optical objective. Raster scans were performed with a step size of 2 μm in both the fast and slow scan directions. Both the MAP and F-Mode images created from the resultant dataset were smoothed using a 2D 2 point averaging filter, and interpolated using 2D 1 point linear interpolation. Zebrafish studies were performed under animal protocol ACC660 of St. Michael's Hospital.

3.5 F-Mode Imaging in Photoacoustic Tomography

To demonstrate proof-of-concept for our F-Mode technique, we imaged a gelatin phantom containing cylindrical, ink-filled vessels with a commercial PAT system equipped with a 40 MHz central frequency linear array transducer. Vessel diameters of approximately 150 μm , 200 μm , and 250 μm , were chosen to mimic the sizes of subcutaneous small arteries in humans [140]. Assessment of sub-millimeter changes in vessel diameter is an important indicator of diseases including hypertension, which is associated a reduction in lumen diameter; in some cases on the order of 100 μm [140–142].

The MAP image from the time domain RF data is shown in Figure 3.2a, and depicts the 250 μm , 200 μm , and 150 μm vessels from top to bottom, respectively. Despite the fact that the lateral resolution of the commercial system is 120 μm [132], it is difficult to ascertain relative vessel size from the MAP image alone. A B-Mode image of the phantom is shown in Figure 3.2b, with the 250 μm vessel situated on the left side of the image. B-Mode sacrifices information in the scanning direction to provide an indication of relative vessel diameter in the axial direction. However, accompanying this is a misrepresentation of the vessel cross-sectional area due to beamforming artifacts introduced as a result of the poor lateral resolution beyond the transducer's acoustic focus, and the limited-view geometry of the linear array transducer [143–145]. Thus, while both MAP and B-Mode techniques are capable of resolving complementary structural aspects of the vessels, neither provides satisfactory indication of all information concurrently.

A representative power spectrum from each vessel is shown in Figure 3.2c. Comparing the three graphs, the location and number of spectral features (i.e. the spacing between adjacent minima) increases with decreasing vessel diameter. This finding is consistent with theoretical solutions of the PA wave equation for cylindrical absorbers [80,136]. The frequency bands used to generate the F-Mode images shown in Figure 3.2d – 3.2i are denoted by symbols Figure 3.2c. An F-Mode animation demonstrating the dynamic transition in image appearance between frequency bands is provided in Movie A.2.

If each vessel is regarded as being in either a 'visible' or 'non-visible' state, there are 8 possible combinations of vessels which can be depicted in an F-Mode image. Here we ignore the cases in which all vessels are visible (as in the MAP image) and all vessels are

not-visible (no detected PA signal). The remaining images demonstrate the capability of F-Mode to specifically target vessels of different size, or combinations thereof. In Figure 3.2d - 3.2f only one of the three vessels is in the visible state. This occurs when a frequency band contains a local maximum for one vessel and local minima for the other two. In Figure 3.2g - 3.2i, two of the vessels are visible, while the spectral power of the third is comparable to the background and thus too low for its visualization. In all F-Mode images it was observed that as the frequency increased, the apparent width of the vessels decreased. This was expected, as in an acoustic resolution PAT system such as the VevoLAZR, the frequency response of the transducer determines the spatial resolution of the images, with finer resolution occurring at higher acoustic frequencies [146].

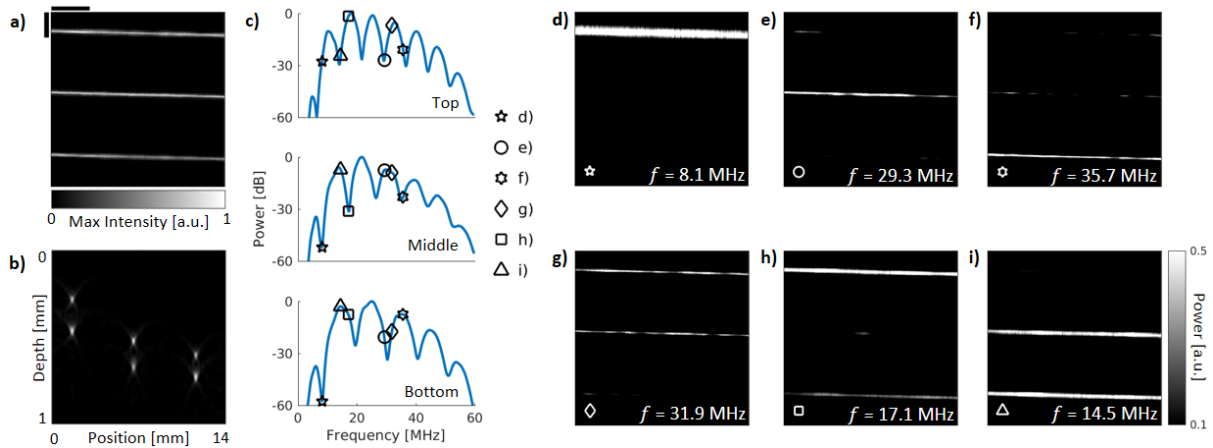


Figure 3.2: a) Maximum amplitude projection (MAP) image of a gelatin vessel phantom acquired with a 40 MHz linear array transducer. The vessels have diameters of 250 μm, 200 μm, and 150 μm, from top to bottom, respectively. The vertical and horizontal scale bars are both 2 mm. b) A PA B-Mode image showing a cross-sectional view of the vessels through the center of a). The 250 μm vessel is to the leftmost side of the image, and the 150 μm vessel is to the rightmost side. c) The averaged F-Mode power spectra from a ROI within each vessel. There is a clear distinction between the vessel power spectra due to the change in vessel diameter. Each shape overlaid on the power spectra corresponds to a frequency band which was used to generate an F-Mode image. d) – i). F-Mode images depicting different permutations of the vessels. Images d) – f) show individual vessels, while images g) – i) show two vessels and exclude the third. The vertical and horizontal scale bars in a) are applicable to all F-Mode images.

The results of this section demonstrate the capacity of the F-Mode technique for generating images which contain information both in the plane orthogonal to the transducer central axis (as in MAP) and in the axial direction (as in B-Mode). We envision that the selective isolation of vessels of specific diameter demonstrated here would be useful when visualizing PA data acquired from complex biological systems; such as the chaotic vasculature of tumours [147], or the plexus of vessels in the mouse brain [37].

3.6 F-Mode Imaging in Photoacoustic Microscopy

As in PAT, the axial resolution of PAM is determined solely by the properties of the acoustic transducer used for signal acquisition, and becomes finer with increasing transducer bandwidth [64]. For this reason, transducers with high central frequency and large bandwidths are highly desirable and are employed in PAM experiments which require sub-cellular resolution [31]. Furthermore, since the number of observable spectral features increases directly with increased transducer bandwidth, the broadband RF data acquired by ultra-high frequency PAM systems readily lends itself to F-Mode analysis.

To demonstrate the robustness of our F-Mode technique with respect to both transducer configuration and frequency response, we scanned two samples with a modular PA microscope. Our PAM system allows the user to easily alternate between different transducers (frequency range 80 - 1200 MHz), optical objectives (from 4 - 40X), and laser sources (covering the UV-VIS-IR range). Additional system details can be found in [34,88].

3.6.1 F-Mode imaging of Polystyrene Microspheres

We first tested our F-Mode technique by acquiring a scan of an agarose phantom containing two populations of black polystyrene microspheres (diameters of 6 μm and 10 μm) as shown in Figure 3.3a. For this experiment, the modular PAM setup was comprised of a 400 MHz transducer, 10X optical objective, and a 532 nm Nd:YAG laser. A MAP image formed from the acquired RF data is shown in Figure 3.3b. Representative power spectra from a 6 μm and 10 μm sphere are shown in Figure 3.3c. At approximately 326 MHz, the summed power is equal for both spheres, with the 6 μm sphere dominating at lower frequencies and the 10 μm sphere dominating at higher frequencies. F-Mode images were formed using the spectral bands which demonstrated the relative greatest contrast for each sphere. The identified bands are indicated with vertical lines in Figure 3.3c. The corresponding F-Mode images are shown in Figure 3.3d and 3.3e.

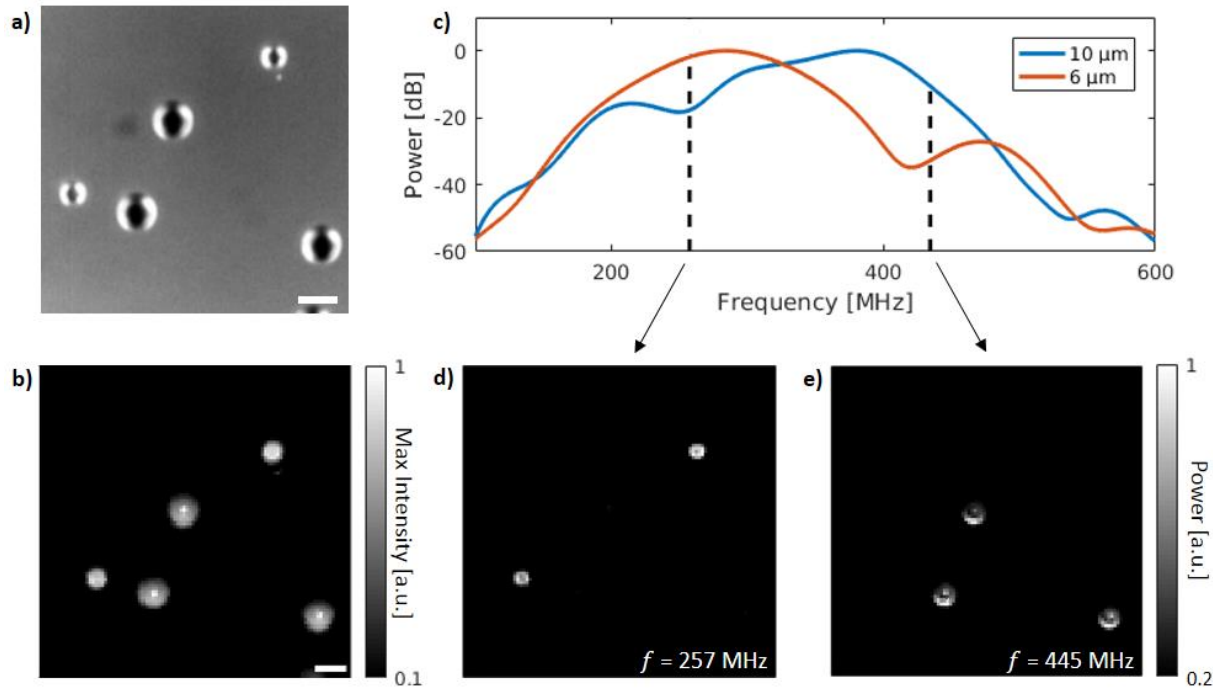


Figure 3.3: a) Optical micrograph of an agarose phantom containing black polystyrene beads with diameters of 6 μm and 10 μm . The scale bar is 10 μm . b) Maximum amplitude projection (MAP) image of the beads acquired with a 400 MHz single element transducer. c) Averaged PA power spectrum of a 10 μm (blue) and 6 μm (orange) bead. The vertical dashed lines correspond to the frequency bands which were used to generate F-Mode images d) and e). d) – e) F-Mode image formed using the 257 MHz and 445 MHz frequency bands, respectively. In d), only the 6 μm beads are visible, while only the 10 μm beads can be seen in e). The scale bar in b) is applicable to both F-Mode images.

In Figure 3.3d only the 6 μm spheres were visible, while in Figure 3.3e this trend is reversed, with only the 10 μm spheres being visible. In addition, the 10 μm spheres in Figure 3.3e appear to have a distinct patterning, which was observed to change as a function of spectral band (Movie A.3). By synchronizing the playback of F-Mode movies of individual spheres of different diameter as a function of ka (where k is the wavenumber corresponding to the acoustic frequency of the band, and a is the radius of the microsphere) it can be shown that the patterning exhibited by the spheres is identical for both bead sizes (Movie A.4). Unlike the other samples examined in this study, the

microspheres are solid and thus support transverse acoustic waves which can be accounted for when considering homogeneous illumination of the microsphere [81]. It is our hypothesis that the tight optical focusing of the objective results in an inhomogeneous heating profile in the microsphere, causing it to deviate from the monopole expansion predicted by theory, and support the propagation of surface waves. Specifically, we believe that the spatial patterns observed in F-Mode arise due to resonant modes excited on the surface of the spheres, as has been demonstrated for the case of US backscatter [148,149]. Preliminary investigations on individual beads (data not shown) for the same system setup with broad optical illumination support these assertions, and elucidation of the physics underlying these observations will be the focus of future work. To our knowledge this is the first time that a relationship between acoustic wavenumber and PA image appearance has been observed for solid microspheres, and opens up avenues for investigating fundamental behavior of surface waves and resonances with PAM.

3.6.2 In vitro imaging of unstained CAKI-2 Cells

Biological cells grown in culture are widely used in the study of drug efficacy [150], genome modification [151], and development of theranostic agents [152]. Adherent cells tend to have a ‘fried-egg’ appearance; with an increased thickness near the nucleus that tapers towards the cell periphery [153,154]. Traditional optical microscopy is the gold standard for 2D cell imaging; however, without the use of specialized techniques like confocal microscopy [155], Raman Imaging [156], or scanning acoustic microscopy [117,153], no indication of cell thickness is typically obtained.

Here we demonstrate the sensitivity of F-mode to micron-size structures and changes in the topology of cultured cells. The modular PA microscope, equipped with a 200 MHz transducer and a 266 nm Nd:YAG laser, was used to scan a population of unstained CAKI-2 renal carcinoma cells. In the deep-UV optical regime (<300 nm), the endogenous absorption of cells increases drastically due to the high extinction coefficient of amino acids (primarily tryptophan, tyrosine, phenylalanine) and nucleic acids [157]. This has previously enabled high resolution label-free imaging of single cells in both deep-UV microscopy [158–160], and deep-UV PAM [50,51] studies. A representative brightfield image and MAP image of an unstained CAKI-2 cell are shown in Figure 3.4a and 3.4c, respectively. The cell appears homogenous in the MAP image except for the non-absorbing vesicles and the strongly absorbing nucleoli (denoted by arrows 1 and 2 in Figure 3.4a, respectively). The MAP image representation agrees well with results obtained in deep-UV microscopy studies by Cheung and colleagues [158,159]. The authors observed uniform absorption throughout a majority of the cell at 260 nm due to uniform protein concentration in the cell cytoplasm and nucleus. The increased PA signal observed in the nucleoli in Figure 3.4c is consistent with previous microspectroscopy studies reporting increased absorption in the nucleoli compared to the remainder of the nucleus [161], and can be attributed to an increase in both the nucleic acid and protein content [158,159].

The frequency response of our 200 MHz transducer is shown in Figure 3.4b. The vertical dashed lines indicate the bands used for F-Mode image generation. It should be noted that for each selected frequency band, the sensitivity of the transducer was more than 20 dB lower than the sensitivity at the transducer's central frequency. Despite this,

high SNR was observed in all F-Mode images (Figure 3.4d–f). Compared to the MAP image, the F-Mode image from the frequency band centered at 90.5 MHz has a uniform distribution of intensities within the cell; the weakly absorbing vacuoles (denoted by the arrow) providing the dominant source of PA contrast in the cell interior. In comparison, the F-Mode image generated from the band centered at 390.5 MHz (Figure 3.4e) portrays a dark central region with a bright outer rim and good visualization of the nucleoli (arrows 2 and 3). We hypothesize that this contrast is due to increased thickness at the cell interior, where the nucleus and a majority of the other organelles are located [153]. Such topography would result in a significant difference in the summed spectral power in the central region of the cell, relative to the thin cell periphery and nucleoli. Finally, in the F-Mode image generated from the 490.5 MHz band, only the two nucleoli of the central cell are depicted (Figure 3.4f). The prominence of the nucleoli in this band is most likely due to a combination of two factors: the strong PA signal generated by the nucleoli, and the increased spectral power density for micron-sized structures such as nucleoli at high frequencies [31], which maximizes the F-Mode contrast relative to the rest of the cell.

The results of this section demonstrate the feasibility of translating the F-Mode technique to biological samples, enabling enhanced visualization of individual organelles. Furthermore, to our knowledge, this is the first time individual nucleoli have been clearly visualized with label-free PAM. In the future, we hope to use this technique to investigate the sequestering and aggregation of contrast agents, e.g. nanoparticles and porphyrin liposomes, within cultured cells [162,163].

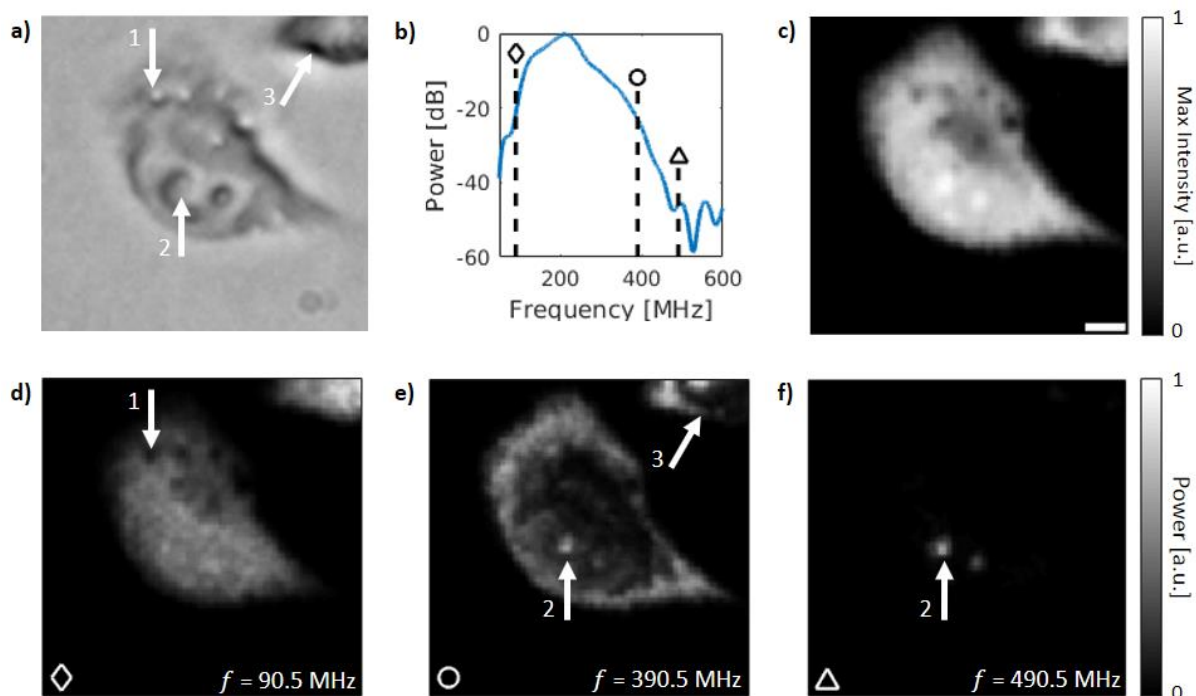


Figure 3.4: a) Optical micrograph of CAKI-2 renal carcinoma cells grown on a UV fused silica substrate. Arrows indicate features which are accentuated in F-Mode images. b) Frequency response of the 200 MHz transducer used to scan the sample. The vertical dashed lines with markers correspond to bands used to create F-Mode images. The difference in transducer sensitivity between the central frequency and each band exceeds 20 dB. c) Label-free MAP image of the cells acquired with a 266 nm Nd:YAG laser. The strongest signal is from the cell nucleoli, with relatively homogeneous intensity throughout the remainder of the cell. The scale bar is 10 μm . d) – f) F-Mode images generated using the 90.5 MHz, 390.5 MHz, and 490.5 MHz frequency bands, respectively. In d), the cell appears uniform with prominent dark vesicles. In e), the periphery of both cells is accentuated, with a dark region in the center of the cells. Finally, in f) only the nucleoli are apparent. The scale bar in c) can be applied to all F-Mode images.

3.7 In-vivo Imaging of Zebrafish Larva

To demonstrate the feasibility of translating the F-Mode technique to *in vivo* models, we imaged the vasculature of a five day-post fertilization (dpf) zebrafish larvae. Due to their low cost, ease of care, and large colony size, zebrafish are rapidly gaining popularity as biological models for drug discovery [164] and the study of disease modeling

[165]. Furthermore, early in their developmental stages, wild type zebrafish larvae have optical properties which are conducive to photoacoustic imaging [166,167]. In wild type zebrafish larvae, the dominant PA chromophores in the visible regime are melanin and hemoglobin. Isolation of PA signals from perfused vasculature can be achieved with the use of pigmentation blockers (e.g. 1-phenyl 2-thiourea (PTU)) [168], or by using mutant zebrafish lines (e.g. the casper fish) which express no pigmentation [169].

We used the modular PAM system, equipped with an 80 MHz transducer and 532 nm laser to image the trunk of a live mutant casper zebrafish larvae. The approximate scan region is denoted by a dashed box in Figure 3.5a, with a cartoon of the vasculature in the region shown in Figure 3.5b. A MAP image of the vessels denoted with a dashed box in Figure 3.5b is shown in Figure 3.5c. As has been shown in previous PA studies, there is excellent visualization of the vasculature at this illumination wavelength due to the endogenous absorption of hemoglobin within the fish erythrocytes [166,167]. The three main classifications of trunk vessel at five dpf are readily identified; namely the dorsal aorta (DA), posterior cardinal vein (PCV), and intersegmental vessels (ISV) [170]. In the standard MAP image, the ISV has a more granular appearance than the other vessels due to the intermittent flow of single erythrocytes through the vessel. In contrast, the flow within the DA and PCV is more uniform, leading to fewer fluctuations in the PA signal intensity during data acquisition, and a more homogeneous intensity in the resultant image. In the MAP image, all three vessels appear with a similar intensity, and selective isolation of individual vessels is not possible. The F-mode technique was capable of accentuating various combinations of vessels. Restricting analysis to the band centered at 12.5 MHz

produces an image depicting only the PCV at the ventral side of the fish (Figure 3.5d). The frequency band centered at 31.5 MHz shows both the DA and PCV (Figure 3.5e); however, the ISV is not discernable. Finally, the 97.5 MHz frequency band delineates the entire ISV, including its origin point on the PCV, which is indicated with an arrowhead (Figure 3.5f).

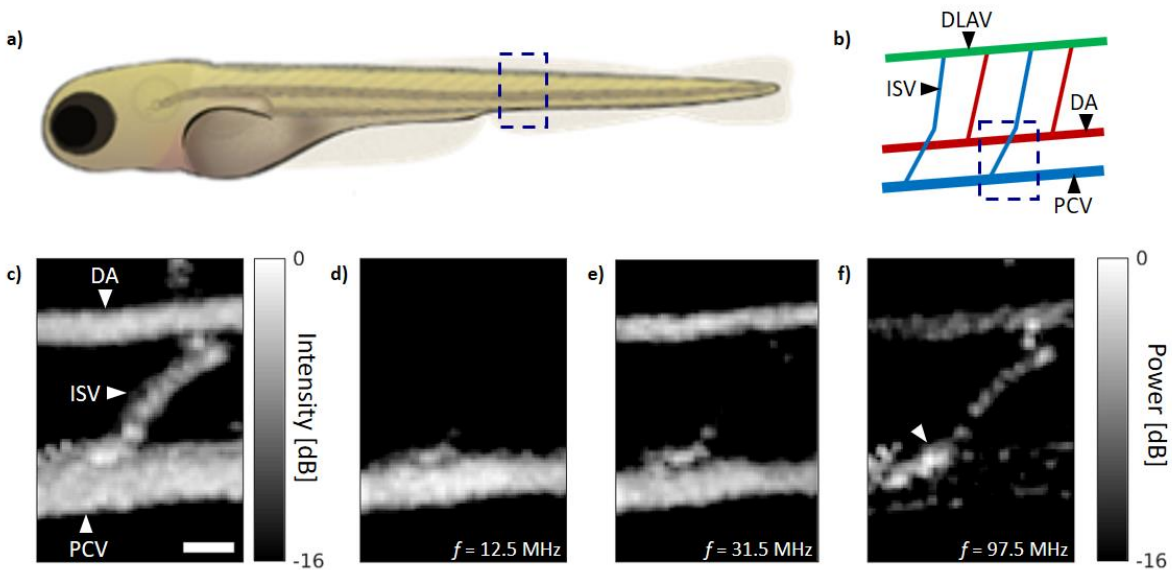


Figure 3.5: a) Cartoon depiction of a zebrafish larva b) Depiction of the vasculature in the region denoted by the dashed box in a). DLAV = Dorsal Longitudinal Anastomotic Vessel, ISV = Intersegmental Vessel, DA = Dorsal Aorta, PCV = Posterior Cardinal Vein. c) Label-free *in vivo* MAP image of the trunk vasculature denoted by the dashed box in b). The PCV and DA run horizontally, while the ISV runs diagonally between PCV and DA. d) – f) F-Mode images generated from the indicated frequency bands. In d) only the PCV can be seen, while in e) both the PCV and DA are visible. The ISV becomes the dominant structure in f). The scale bar in c) is 20 μm and can be applied to all F-Mode images.

The success of these preliminary *in vivo* studies points towards future application in larger animal models, and could ultimately be used in conjunction with deeply penetrating PAT to probe for vessels which have atypical lumen diameters, for example, those which contain atherosclerotic plaques [171]. The method could also be adapted to

new developed PA methods, such as microtomy-assisted photoacoustic microscopy (mPAM)[52], to provide scale specific contrast in 3D imaging of large tissue specimens.

3.8 Discussion & Conclusion

The F-Mode technique proposed in this study utilizes unique features in the frequency domain of PA RF-signals as a novel source of image contrast. Images generated with the technique surpass the capabilities of standard MAP reconstruction when differentiating between objects of different scale within phantoms (Figure 3.2, Figure 3.3). When used in conjunction with label-free PAM, F-Mode provides a dynamic way to selectively enhance the visualization of organelles in single cells (Figure 3.4) and vessels of different sizes in small *in vivo* animal models (Figure 3.5). In the future, we plan to apply F-Mode analysis to PA datasets acquired with functional PA to further enhance the selectivity of visualizing arteries and veins *in situ* [37]. Furthermore, due to the similarity between the two modalities, we plan to apply F-Mode analysis to datasets acquired with ultra-high frequency US techniques, such as those used for single cell imaging [34,153], to provide a dynamic source of contrast for samples with little deviation in local mechanical properties.

The F-Mode technique is still being refined and there is potential for further optimization of the algorithm. A current challenge is appropriate selection of the size of the frequency band size used for F-Mode analysis. If the selected band size is relatively wide compared to the spacing of the features in the frequency domain, it will capture several minima at once and decrease the technique's sensitivity to objects of similar size.

Conversely, if the band size is too narrow, the algorithm will become more resource intensive and the computational time will increase. The size of the F-Mode frequency band used in this work was fixed based on the central frequency of the imaging system's transducer. This tactic is effective when the scale of the structure being probed is known a priori; however, this information may not always be readily available, especially in *in vivo* implementations. In such cases, the FFT of a representative RF line from the object can be computed and used as an aid to select a band of appropriate size. Going forward, we will integrate this process into the algorithm workflow so that the selection of optimal band size becomes fully automated.

For objects with the same shape and acoustic properties, the distance between adjacent spectral minima is inversely related to the size of the object (Movie A.1). This imposes a limit on the minimum object size for which oscillations in the F-Mode intensity can be detected. For example, when considering a transducer with upper bandwidth limit f_{max} , the smallest radius, a , of a spherical object (such as a mammalian cell in suspension [88]) which would yield a spectral minimum in the transducer bandwidth is given by $a = \frac{4.49v_s}{2\pi f_{max}}$, where v_s is the speed of sound of the object. Objects smaller than this limit will not exhibit a dynamic change in contrast; however, they can still serve as useful standards for comparing the fluctuations observed in other objects present in the image.

Our F-Mode technique is applicable to data acquired from a wide range of PA imaging systems, operating at transducer frequencies ranging from the tens to hundreds of megahertz. As no modification to existing PA hardware is required for F-Mode analysis,

it can easily be implemented in tandem with other PA reconstruction techniques to provide additional structural information with minimal additional post-processing. We believe that due to its versatility, ease of implementation, and sensitivity to objects of different scale, F-Mode has the potential to develop into a valuable tool with a wide range of applications in the field of biomedical imaging.

3.9 Acknowledgements

The authors would like to thank Koroboshka Brand-Arzamendi for the larval zebrafish cartoon. This research was supported in part by: the Natural Sciences and Engineering Research Council of Canada, the Canadian Cancer Society, the Canadian Foundation for Innovation, the Ontario Ministry for Research and Innovation, and the Terry Fox Foundation Funding agencies.

Chapter 4

Triplex micron-resolution acoustic, photoacoustic, and optical transmission microscopy via Photoacoustic Radiometry

4.1 Abstract

We present a new sensing technique, termed photoacoustic radiometry (PAR), for mapping the optical attenuation properties of a sample. In PAR, laser pulses attenuated via transmission through the sample impinge on the ultrasound transducer and generate a photoacoustic (PA) signal within it. Spatial variation of the optical attenuation properties of the sample influences the amplitude of the PAR signal, providing image contrast. Performed simultaneously with pulse-echo ultrasound and PA imaging, this triplex imaging technique enables rapid characterization of samples with micrometer-resolution in a single scan. In this work, we demonstrate that the PAR technique can be easily integrated into existing PA microscopy systems, with applications in imaging thin

This Chapter is based on a manuscript which has been published as:

M. J. Moore, E. M. Strohm, M. C. Kolios, “*Triplex micron-resolution acoustic, photoacoustic and optical transmission microscopy via photoacoustic radiometry*,” *Optics Express*, vol. 26(17), 2018.

biological samples and non-destructive evaluation of optically-opaque materials such as silicon wafers.

4.2 Introduction

Mounting interest in high resolution, label-free, non-destructive imaging of biological and manufactured samples has led to a resurgence in the technique of photoacoustic (PA) microscopy (PAM) [36,172,173]. In typical optical-resolution PAM (OR-PAM), a nanosecond or picosecond pulsed laser is focused to a diffraction limited spot on the sample through a series of lenses or a microscope objective. Absorption of a portion of the incident beam results in a localized isochoric heating and subsequent thermoelastic expansion, leading to the emission of an acoustic wave that is typically detected using an ultrasound (US) transducer [31]. While the potential for simultaneous pulse-echo US imaging in current OR-PAM systems exists, most systems use US transducers with central frequencies in the 20-60 MHz range, resulting in large acoustic focal spots and poor resolution ultrasound images [33]. However, when using transducers with central frequencies in the hundreds of megahertz (MHz) range, such as those used in scanning acoustic microscopy, the lateral resolution achievable with US imaging approaches (and in some cases, surpasses) that of OR-PAM [61,174]. Furthermore, since the axial resolution in PAM is proportional to the transducer bandwidth [33,64], the use of ultra-high frequency (UHF) transducers also results in micron level axial resolution [44,175].

With UHF-PAM systems, sequential acoustic and PA imaging with is readily achievable [34]. While the PA image derives contrast from the spatial variation in the

sample's optical absorption properties, the contrast in US imaging is dependent upon the sample's mechanical properties (e.g. acoustic impedance, attenuation, speed of sound) [61]. We have previously demonstrated that the unique information contained in both image types can be used to differentiate between different kinds of leukocytes in a human blood smear [34]. By tuning the illumination wavelength in the PA measurements, unique absorption profiles for stained lymphocytes, neutrophils, and monocytes were obtained. Further, differences in the acoustic attenuation through each cell type suggested variation in the intracellular chromatin structure.

In some OR-PAM setups, triplex imaging can be realized without modification to existing hardware. For example, Subochev et al. reported a triplex reflection-mode PAM setup capable of simultaneous diffuse optical reflectance (DOR), PA, and US imaging [176–178]. In this system, photons from the PA excitation beam backscattered from the sample are detected through absorption in the 35 MHz PVDF transducer, providing a detectable signal dependent on the sample DOR. The same photons absorbed in the hemispherical PVDF result in the emission of a laser induced US wave, which propagates towards the sample and can be used for US imaging. However, due to the low central frequency of the PVDF transducer, the resolution of the PA, US, and DOR images is limited to 50 μm , 35 μm , and 3.5 mm, respectively, and thus the system is not suitable for imaging samples with micron level detail [176]. Furthermore, due to the mechanism of acoustic wave generation, the amplitude of the laser induced US pulse is directly coupled to the DOR signal, and therefore cannot not reliably be used to assess the mechanical properties of the sample.

Here we present a new method for simultaneously generating images that depict the mechanical, optical absorption, and optical attenuation properties of a sample with micron-level detail. Mechanical and absorption properties are assessed via UHF pulse-echo US and PAM, respectively, while the optical attenuation properties are provided by a novel sensing technique termed Photoacoustic Radiometry (PAR). The PAR technique is readily implemented in PAM setups in which the laser used for PA signal generation illuminates the transducer after passing through the sample. Optical attenuation of the laser beam by the sample influences the amplitude of the detected PAR signal, providing image contrast dependent on both optical absorption and scattering. In this work, we describe and characterize the PAR technique, and demonstrate its ability to acquire high-resolution images of optically transparent samples. We then demonstrate duplex micron-resolution PAR/PA imaging of single biological cells, and triplex PAR/PA/US imaging of a silicon wafer integrated circuit.

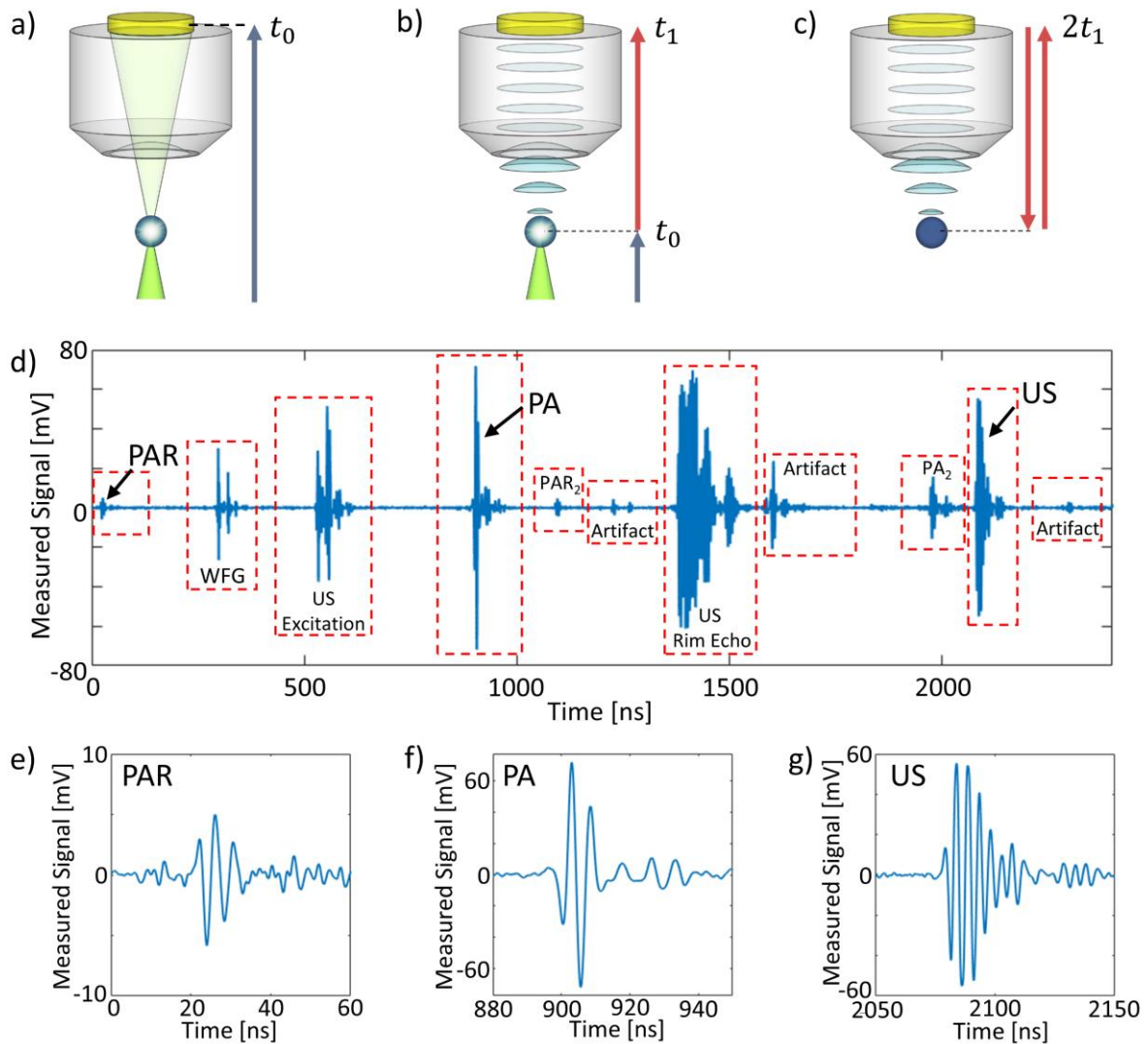


Figure 4.1: a) An illustration of the PAR technique. A laser pulse, having been attenuated by the sample, strikes the active element of the transducer, and produces a PAR signal at time t_0 . b) The typical scheme for photoacoustic signal generation. The PA signal is detected at time t_1 . c) The US pulse-echo signal is detected at time $2t_1$. d) A representative RF line acquired from a triplex scan of a permanent marker on a microscope slide. Various features of the signal, including excitation pulses from the Waveform Generator (WFG) and US pulser, are labelled. Multiple detections of reflected acoustic waves trapped within the transducer are denoted with subscripts. e) – g) Time-gated PAR, PA, and US signals, respectively.

4.3 Methods

4.3.1 Description of the PAR Technique

Typically there are two main components in single element UHF transducers: a multi-layer active element, used to generate the US plane wave; and a sapphire or quartz buffer rod, which is used to focus the resultant wave [61]. In these implementations the active element consists of a piezoelectric material (e.g. zinc oxide, ZnO), sandwiched between two thin metal films which are used as electrical contacts [61,179,180]. Application of a potential difference results in an expansion of the piezoelectric layer and the emission of an acoustic wave. Conversely, compression of the piezoelectric layer within the active element due either to backward propagating US waves (Figure 4.1c), or forward propagating PA waves (Figure 4.1b), results in a detectable voltage. In the PAR technique (Figure 4.1a), the portion of the excitation laser beam that is transmitted through the sample impinges directly upon the active element, generating a PA wave that is detected by the piezoelectric material. In this way, for every laser pulse emitted, two PA waves are generated simultaneously; one originating from the sample, and the other originating within the transducer. As ZnO is transparent to visible light [181], we hypothesize that the PAR signal is due to laser absorption in the metallic contacts. The PAR signal is directly proportional to the laser fluence at the active element, and is thus sensitive to both the optical absorption and scattering properties of the sample being interrogated.

4.3.2 System Specifications

The UHF-PAM setup consists of a SASAM acoustic microscope (Kibero GmbH, Germany) modified to include a pulsed laser source. A schematic representation of the

system is shown in Figure 4.2a. The SASAM operates in transmission mode, with a 10X optical objective with numerical aperture of 0.25 (Olympus, Japan) situated below the sample, and the transducer used for signal detection aligned confocally with the objective on the opposing side. The system was equipped with one of two interchangeable lasers: a 532 nm pulsed Nd:YAG laser (Teem Photonics, France) with a pulse width of 330 ps and pulse repetition frequency (prf) of 4 kHz, or a 1064 nm laser (Teem Photonics, France) with a pulse width of 500 ps and prf of 2 kHz. A 70:30 beam splitter (Thorlabs, USA) was used to sample the incident beam energy and direct it to a joulemeter (Gentec-EO, USA) for pulse energy measurement. Signal detection was performed using a 200 MHz transducer with a 30° semi-aperture angle, -6dB bandwidth of 120 MHz, and depth-of-field of 54 μm . All acquired signals were digitized at a rate of 8 GS/s with a 10-bit digitizer (Agilent, USA). In experiments where only PAR images were generated, 100x signal averaging was used to maximize SNR. All data acquisition was performed at 37°C, and MilliQ water was used to provide acoustic coupling between the transducer and sample when PA or US signals were acquired in addition to the PAR signal.

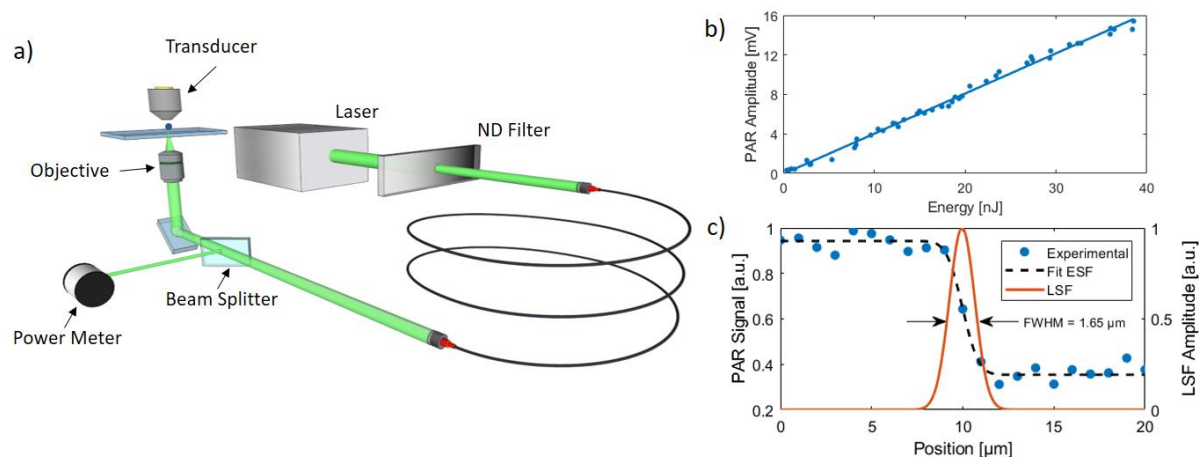


Figure 4.2: a) Experimental system setup, consisting of a PA microscope in transmission mode, equipped with an UHF transducer. b) Amplitude of the recorded PAR signal as a function of incident laser pulse energy for direct transducer illumination. c) FWHM of the ESF, demonstrating the lateral resolution of the system.

4.3.3 PAR Imaging of a Transparent Sample

A glass bottom petri dish with etched alphanumeric patterning (MatTek, USA) was scanned with the 532 nm laser. The glass was composed of borosilicate and had a thickness of approximately 170 μm . For the first scan, the transducer and dish were separated by an air gap. Immediately after this non-contact scan, a drop of Microscope Immersion Oil (Olympus, USA) with refractive index of 1.516 was added, completely filling the air gap between the etched glass and transducer. A second scan was then performed over the same region of interest. Both raster scans were 600x600 μm in size with a step size of 4 μm in both fast and slow directions. Maximum amplitude projection (MAP) images of the PAR signals were formed for each scan.

4.3.4 Simultaneous PAR and PA Imaging of Biological Samples

CAKI-2 renal carcinoma cells (ATTC, USA) were cultured in a glass bottom petri dish (MatTek, USA) in McCoy's 5A medium supplemented with 10% fetal bovine serum.

The media was aspirated, and the dish was rinsed with 1X PBS. The cells were then fixed with 2 mL of ice cold methanol for 10 minutes. The methanol was aspirated, and a second PBS rinse was performed. A 1:200 dilution of DRAQ5 dye (BioStatus, UK) in PBS was added to the fixed cells to stain the cell nucleus. The cells were incubated in the dark with the dye solution for 10 minutes. To remove residual dye after the staining process, three PBS rinses were performed. Cells of interest were identified using brightfield microscopy, and PA/PAR measurements were performed using the SASAM and the 532 nm laser. Although DRAQ5 exhibits an absorption maximum at 647 nm, the dye absorbs at wavelengths as short as 488 nm [182], and thus can be excited in PAM with the 532 nm laser. After the scan, the sample was transferred to a Zeiss Axio-observer microscope where DIC and fluorescence images of the cell were acquired with a 40X, 0.6 NA objective, and an OrcaR2 CCD camera. DRAQ5 exhibits low photobleaching [183], and there was no observable decrease in fluorescence intensity for the scanned cell compared to other cells in the dish. The PAR and PA signals were isolated by time gating, and a MAP image was formed for each dataset. A binary mask for the PA MAP image was generated by computing the sum of the absolute value of the RF-line for each scan position, and then zeroing pixels with value lower than the interior of the cell nucleus.

4.3.5 Triplex Imaging of an Integrated Circuit

As a proof of concept for the triplex PAR/PA/US technique, an integrated circuit on top of a 400 μm thick silicon wafer die (TMS320C51 DSP, Texas Instruments, USA) was imaged using the 1064 nm laser. A TTL signal generated upon laser emission was used to trigger the US pulser for simultaneous pulse-echo US measurements. Nanosecond jitter in

the triggering of the pulser decreases the SNR of the US signal when high averaging is used, thus only 5x signal averaging was used for all triplex signal acquisition. The resultant scan dataset was time gated to isolate and generate MAP images for each of the PAR, PA, and US signals, respectively.

4.4 Results & Discussion

4.4.1 PAR Characterization

A representative triplex RF-line acquired from ink on a glass coverslip is shown in Figure 4.1d. The PAR, PA, and US signals are labelled with arrows. In addition to the signals used for image generation, several other features are noted. Excitation pulses from both the waveform generator (WFG) and US pulser are observed after detection of the PAR signal, but before detection of the PA signal. The large impedance mismatch between the buffer rod and coupling medium results in a strong echo of the generated US pulse from the transducer rim. This mismatch also causes multiple reflections of acoustic waves within the transducer. Finally, there are some unidentified artifacts in the RF-line; however, the time at which these artifacts occur is invariant, and thus they do not compromise the signals containing information about the sample. As demonstrated in Figure 4.1e-g, each of the PAR, PA, and US signals has high signal-to-noise ratio (SNR) and can be isolated through time gating. The amplitude of the PAR signal as a function of laser pulse energy was assessed by removing the sample stage and directly illuminating the transducer. The maximum PAR signal amplitude as a function of laser pulse energy is shown in Figure 4.2b. The PAR signal amplitude increased linearly ($R^2 = 0.994$) with increasing laser energy, supporting the hypothesis that the PAR signal is due to PA

excitation. Signals with SNR greater than 5 were obtained at pulse energies above 1 nJ. In addition to determining the minimum pulse energy required for a usable PAR signal, these measurements also demonstrate that the PAR signal originates completely within the transducer; i.e. that the detected signal is not the result of any PA or US waves which originate from the sample and are detected as multiple reflections (c.f. Figure 4.4 in Briggs [61]).

To determine the resolution of the PAR and PA imaging techniques, the edge of one of the elements on a USAF test target was scanned with a step size of 0.2 μm . The resultant edge spread function (ESF) is shown in Figure 4.2c. For enhanced visualization, only a subset of the scan points acquired are displayed on the graph. The ESF was fit to an error function, and the line spread function (LSF) was calculated via differentiation. The size of the acoustic focal spot for the 200 MHz transducer is approximately 8 μm , thus the 1.65 μm FWHM of the LSF can be taken as the lateral resolution for both PAR and PA techniques, and is close to the diffraction limit for a 0.25 NA objective with an incident wavelength of 532 nm.

4.4.2 PAR Imaging of a Transparent Sample

A brightfield image of the letters etched on the surface of the empty glass bottom dish is shown in Figure 4.3a, with the corresponding non-contact PAR image shown in Figure 4.3b. In both the brightfield and PAR images, optical absorption in the glass is negligible, and image contrast can be attributed to the scattering of light due to variations in geometry and refractive index. The most striking feature in the PAR image is the high contrast at the vertical edges of the etched channels. This can potentially be explained by

total internal reflection of a portion of the focused laser beam at the vertical channel wall. The maximum angle of incidence of the beam to a surface orthogonal to the objective's optical axis ($\approx 14.5^\circ$) is well below the critical angle for an air/glass interface ($\approx 41.3^\circ$); however, when the surface is parallel with the optical axis, as in the case of the vertical channel walls, the incident angle is 75.5° and a majority of the incident beam can be reflected back into the glass. Such a reflection would decrease the fluence at the transducer active element and in turn decrease the amplitude of the recorded PAR signal. Debris on the top surface of the glass appeared as dark spots in the PAR image with signal amplitude substantially lower than that of the background. In comparison, debris located on the bottom of the dish away from the objective focal plane (denoted with arrow heads) had a blurry appearance with higher PAR amplitude than those on the top. The PAR image acquired from the same scan region after the addition of immersion oil with index of refraction similar to the glass is shown in Figure 4.3c. The etched letters are no longer visible, as the refractive index mismatch at the channel wall has been eliminated. The only discernable features are the dark spots caused by the debris on the bottom of the dish. After the addition of the immersion oil, the mean signal amplitude in the image was observed to increase approximately by a factor of three. This could potentially be due to decreased refraction at the surface of the sample, and transducer rim, leading to an increase in the fluence at the transducer active element. In the future, we plan to investigate this phenomenon further with the use of Finite difference time domain (FDTD) or Finite Element Method simulations.

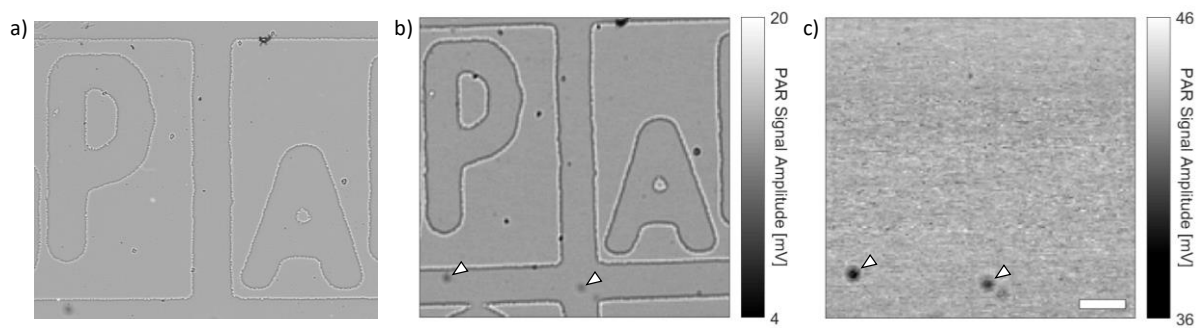


Figure 4.3: a) Brightfield image of an etched glass bottom petri dish. The letters “P” and “A” are shown. b) Non-contact PAR scan of the same letters shown in a). Excellent contrast is observed at the edges of the channel. Two out-of-focus pieces of debris on the bottom of the dish are indicated with arrowheads. c) PAR image of the same region after adding microscope immersion oil with a refractive index similar to the glass. The etched letters are no longer visible; however, the out-of-focus pieces of debris can still be seen clearly. The scale bar in c) is 100 μm and can be applied to all images.

4.4.3 Simultaneous PA and PAR Imaging of Single Biological Cells

A differential interference contrast (DIC) microscopy image of a representative CAKI-2 cell is shown in Figure 4.4a, with a fluorescence image of the same cell shown in Figure 4.4b. In the DIC image, an arrowhead denotes one of three nucleoli found in the interior of the cell nucleus, and an arrow denotes what is most likely a combination of the Golgi apparatus and endoplasmic reticulum in the perinuclear region [184]. The fluorescence image shows the sequestering of dye within the cell. With the exception of the dark rings at the periphery of the nucleoli, the fluorescence intensity is relatively uniform. Unlike some other common nucleic acid stains (e.g. Propidium Iodide), DRAQ5 exhibits highly specific binding to DNA, and does not require the use of RNase to limit fluorescence from nucleic acid in the cell cytoplasm [183]. Furthermore, DRAQ5 is known to have a low quantum yield [185], making it an ideal contrast agent for PAM. An overlay of the brightfield and fluorescence images shown in Figure 4.4c. The overlaid image

provides context for the fluorescence; demonstrating the localization of the stain within the nucleus.

PAR and PA images simultaneously acquired from the same cell are shown in Figure 4.4d and Figure 4.4e, respectively. The PAR and DIC images show similar features, with both the boundary of the cell cytoplasm and the internal structures denoted in Figure 4.4a readily identified. As cells have negligible absorption in the visible spectrum, structure in the unstained portion of the cell is likely due to a combination of changes in the cell topography and differences in organelle refractive index, e.g. between the nucleus and cytoplasm [186,187]. The PA image is in good agreement with the fluorescence image, with the dark rings at the periphery of the nucleoli readily discernable. A possible reason for these rings is an abundance of rRNA, which is not targeted by DRAQ5 [183], and thus would lead to a decrease in both fluorescence and PA signal. Furthermore, the PA image exhibits nuclear features not present in the standard fluorescence technique (denoted with arrowheads), perhaps indicative of variation in the nuclear chromatin distribution [188].

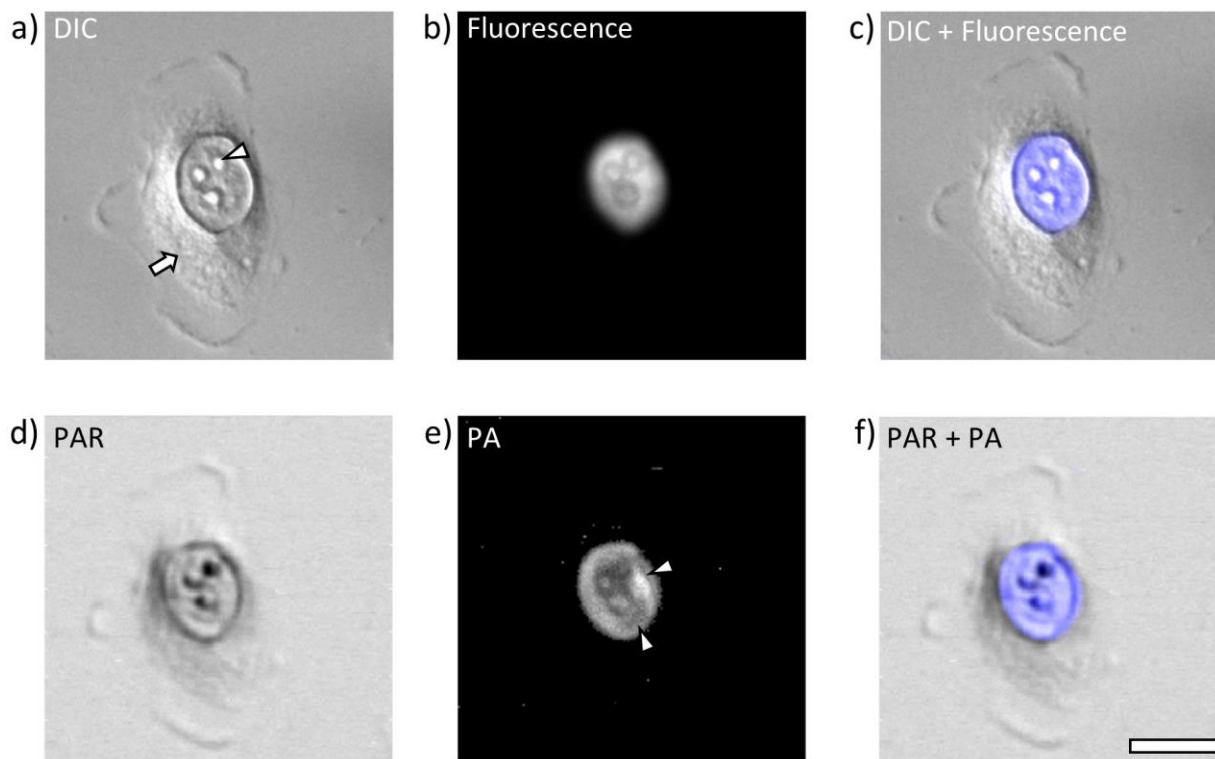


Figure 4.4: a) Differential Interference Contrast image of a CAKI-2 renal carcinoma cell. The arrowhead indicates one of three nucleoli in the nucleus, and the arrow indicates the Golgi apparatus and endoplasmic reticulum. b) Fluorescence image of the same cell. c) An overlay of the images in a) and b) provides context for the fluorescence image. d) PAR image and e) PA image of the cell in a) derived from a single scan. f) The overlay of the PAR and PA images agrees well with the optical microscopy overlay. The scale bar is 20 μm , and can be applied to all images.

The composite PAR/PA image is shown in Figure 4.4f, and bears striking similarity to the DIC/fluorescence composite image acquired with the 40X objective. It is prudent to note that the contrast in DIC is primarily due to gradients in the phase difference of light transmitted through the sample [189], and thus, while there appears to be an inversion of contrast in Figure 4.4f compared to Figure 4.4c, both images provide unique and complimentary information. While the direction of the shadows can be arbitrarily adjusted by adjusting the bias in the DIC image [189], the features of the PAR image are determined

by the attenuation properties of the sample, and in the current implementation can only be modified by changing the refractive index of the medium surrounding the cell.

The results of this section demonstrate the feasibility of applying the simultaneous PAR/PA imaging technique to a sample of stained biological cells. Overlaying the PA images on the PAR images provides context for the features observed in the PA image, and does not require co-registration of images acquired using different modalities. Furthermore, the composite PA/PAR images provide excellent agreement with well established techniques like DIC/fluorescence, and can be accomplished without the use of CCDs and additional optical components (e.g. condensers, prisms). In the future, we plan to generate label free PAR/PA images of biological cells by leveraging the endogenous absorption of erythrocytes and melanoma cells in the visible wavelengths, and of proteins and nucleic acids in the UV regime [51].

4.4.4 Triplex Imaging of Silicon Wafer

An optical micrograph of the top surface of the die is shown in Figure 4.5a. The images resulting from the simultaneous PAR/PA/US scan are shown in Figure 4.5b-d. Each image displays unique features dictated by the modality used for image generation. Comparing the simultaneously acquired images, regions which appeared bright in the PAR image (Figure 4.5b) appeared dark in the PA image (Figure 4.5c), and vice versa. Due to the low optical absorption of silicon in the near infrared [190], we hypothesize that this is due to the presence of strongly absorbing metallic components, such as aluminum, copper, or tungsten, which are deposited on the wafer surface during fabrication [191]. These metallized layers significantly decrease the detected PAR signal, but are known to yield

high PA signals in PAM [192]. Both PA and US are 3D imaging modalities, and can be used to generate depth-resolved B-Mode images depicting absorber/scatter distribution within the transducer DOF, respectively. In contrast, since the PAR signal is generated by direct optical excitation of the transducer active element, it is not possible to create depth-resolved images with the technique. However, as demonstrated in Figure 4.3, the PAR signal amplitude is directly affected by features at any point along the beam path which modulate the laser fluence at the active element. In this way, the 2D PAR images depict features which are well out of range of the transducer's acoustic DOF, and would otherwise be undetected. For example, diagonal tracks inscribed on the bottom of the wafer during the wafer backgrinding process [193] are readily apparent in Figure 4.5b (denoted by an arrow), but are not visible in either the PA or US images.

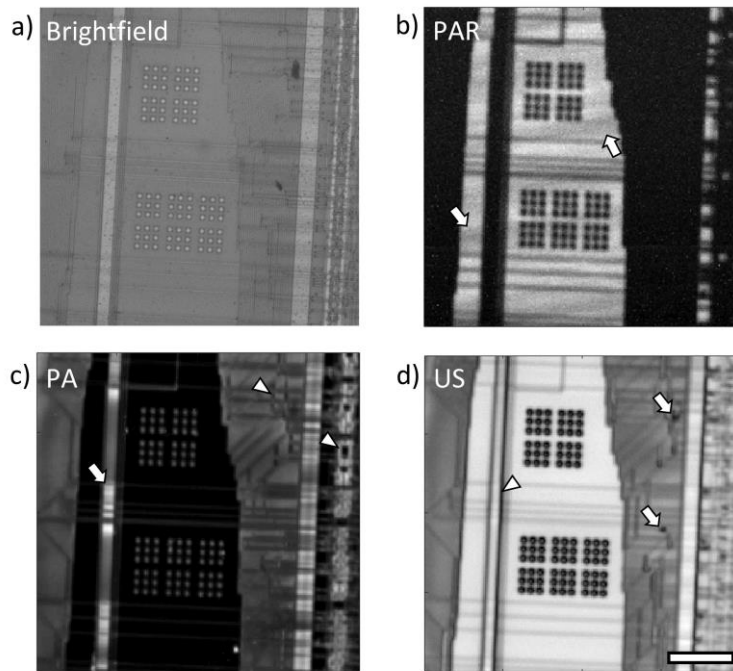


Figure 4.5: a) Optical image of the top of an integrated circuit die on a silicon wafer substrate. b) – d) PAR, PA, and US images acquired with triplex imaging, respectively. Features unique to each image are denoted with arrows and arrowheads. The scale bar is 100 μm .

Intricate surface patterns (denoted with arrowheads) are apparent in the metalized regions of the PA image. While these patterns are also visible in the US image, the contrast is greater with PA, potentially due to the presence of several different metallic components. The aforementioned surface features were not visible in the PAR image (Figure 4.5b); this is due to the low signal averaging used in this scan. However, as shown in Figure 4.6, when signal averaging was increased to 150x, similar patterns could be seen in the PAR image of a different die on the same wafer. Additional features which are unique to the PA image, such as those denoted by the arrows, are likely due to deviations in the thickness or composition of the metal surfaces, or to the quality of the surface bonding [192].

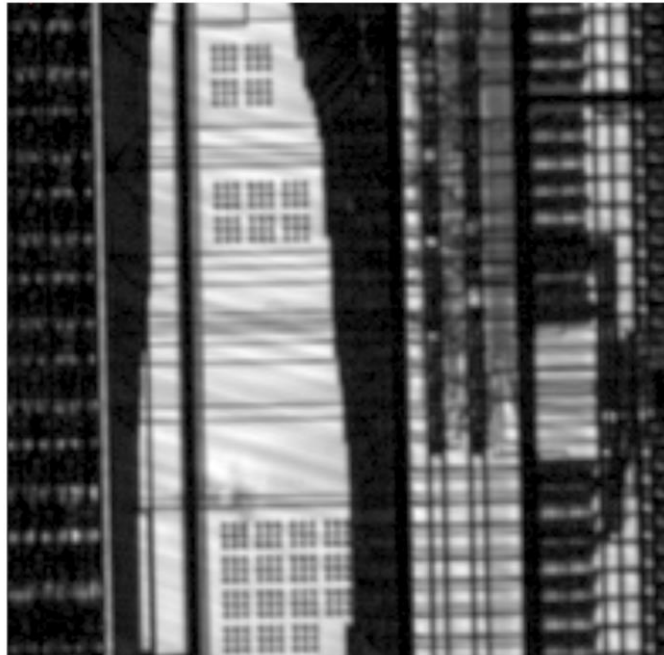


Figure 4.6: Non-contact PAR scan of a different die from the wafer shown in Figure 4.5. The higher signal averaging enhances SNR and makes additional features visible. The scan region is 1 mm x 1 mm.

High-frequency US images can be used to identify the quality of adhesion between the layers of integrated circuits, as well as identify changes to both surface topology and

detect subsurface cracks and voids [194]. Although no such subsurface features were detected in the present triplex US image, high contrast edges were observed at the boundary of the metallized layers on the die surface (arrowhead). The US image is the only image which showed indication of two imperfections on the top surface of the die (denoted by the two arrows in Figure 4.5d), which are also seen in the optical image. These could potentially be debris which have strong optical absorption in the visible regime, but negligible absorption in the near infrared, and are thus not detectable with the present IR setup. Due to the relatively larger size of the acoustic focal spot (approximately $8\ \mu\text{m}$) compared to the optical modalities, the US image has the poorest lateral resolution of the three images. Nevertheless, fine detail such as the 3 by 3 grids of $10\ \mu\text{m}$ square contacts on the top of the die are still easily resolved.

4.5 Conclusion

Our PAR imaging technique derives contrast from spatial variation in a sample's optical absorption and scattering properties. We demonstrate that in our transmission mode UHF-PAM setup, PAR can be performed simultaneously alongside high resolution PA and US imaging, and allows for the detection of features well outside the transducer's DOF. Additionally, we show that the technique can be used to resolve micron-sized objects which exhibit scant optical absorption in both biological and inert samples, provided that a refractive index mismatch between the target and its surroundings exists. With our current implementation, the lateral and axial resolutions of our triplex technique are limited by the low NA of the 10X optical objective, and the bandwidth of the acoustic transducer, respectively. Going forward, we plan to use a 0.45 NA objective with a 1 GHz

US transducer to push both lateral and axial resolutions to the $1\ \mu\text{m}$ range [34]. Further improvements will include the integration of a low-jitter US pulser into the system, allowing for higher signal averaging thereby increasing the SNR of all acquired signals. In the future, we plan to use this high-resolution triplex imaging technique to image thin biological samples, for example, cancer cells and zebrafish larvae, and compile co-registered datasets of endogenous absorption, attenuation, and mechanical properties.

4.6 Acknowledgements

The authors would like to thank Caterina Di Ciano-Oliveira for assistance with acquiring DIC and fluorescence microscopy of the biological samples in this work. This research was supported, in part, by: the Sciences and Engineering Research Council of Canada, the Canadian Cancer Society, the Canadian Foundation for Innovation, the Ontario Ministry for Research and Innovation, and the Terry Fox Foundation Funding agencies.

Chapter 5

Simultaneous Ultra-high Frequency Photoacoustic Microscopy and Photoacoustic Radiometry of Zebrafish Larvae *in vivo*

5.1 Abstract

With their optically transparent appearance, zebrafish larvae are readily imaged with optical-resolution photoacoustic (PA) microscopy (OR-PAM). Previous OR-PAM studies have mapped endogenous chromophores (e.g. melanin and hemoglobin) within larvae; however, anatomical features cannot be imaged with OR-PAM alone due to insufficient optical absorption. We have previously reported on the photoacoustic radiometry (PAR) technique, which can be used simultaneously with OR-PAM to generate images dependent upon the optical attenuation properties of a sample. Here we demonstrate application of the duplex PAR/PA technique for label-free imaging of the anatomy and vasculature of zebrafish larvae *in vivo* at 200 and 400 MHz ultrasound detection frequencies. We then use the technique to assess the effects of anti-angiogenic drugs on the development of the larval vasculature. Our results demonstrate the effectiveness of simultaneous PAR/PA for acquiring anatomical images of optically

transparent samples *in vivo*, and its potential applications in assessing drug efficacy and embryonic development.

5.2 Introduction

In recent years, there has been a rapid increase in the use of zebrafish as specimens for biomedical research [164]. The rapid adoption of zebrafish as an *in vivo* biological model has been facilitated by several factors, including their low cost, high fecundity, and short maturation time [195,196]. As small animal models, zebrafish have been used in studies investigating the progression of disease [165], drug screening and discovery [164,197], and embryonic development [197–199]. While adult wild-type zebrafish exhibit a characteristic striped patterning dictated by the three variants of pigmentation cells in their bodies (melanophores, xanthophores, and iridophores) [200,201], the larval fish are largely transparent, and their internal structures are easily viewed using conventional microscopy techniques. To further enhance optical clarity, chemicals such as 1 phenyl 2-thiourea (PTU) can be added early in the developmental cycle to inhibit melanophore production [168], or mutant fish which express limited pigmentation into adulthood are used [169].

Coupled with high optical transparency and abundant endogenous chromophores (i.e. melanin and hemoglobin) zebrafish larvae are also excellent candidates for imaging with photoacoustic microscopy (PAM). Conventional transmission-mode optical-resolution photoacoustic microscopy (OR-PAM) setups have been used to image the eye, vascular system, and heart [202] as well as cardio-cerebrovascular development [166] *in vivo* in pigment-suppressed zebrafish larvae. Other techniques, such as spatial

resolution-invariant PAM (SIR-PAM) have been used to acquire whole-body images of pigmentation in 3 day-post-fertilization (dpf) larvae over a lateral resolution-invariant axial range of 1.8 mm [203]. Multiview imaging techniques have also been employed in both PAM [134] and photoacoustic mesoscopy [66] setups to generate images with more isotropic resolution; however, these studies have only been performed with *ex vivo* specimens.

While PAM techniques yield high resolution maps of endogenous absorption, they contain no information pertaining to the gross anatomical tissue of the zebrafish, which has negligible absorption at illumination wavelengths typically used in PAM. For this reason, recent work has focused on creating hybrid systems combining several types of imaging modalities (e.g. as is commonly done with fluorescence and brightfield microscopy) with PAM to provide additional context for the acquired images. Rao et al. used an integrated photoacoustic, confocal, and two-photon microscope to acquire confocal fluorescence images of the spinal cord and posterior lateral line nerve as well as PAM images of vasculature *in vivo* in a transgenic larvae [204]. Soliman et al. used an integrated multi-photon and multi-scale photoacoustic microscope to acquire label free OR-PAM, as well as brightfield, and second, and third harmonic generation microscopy images of a 6 dpf wild-type zebrafish larvae [205]. The hybrid system was able to resolve melanin spots with PAM, as well as individual muscle fibrils and connective tissue within the trunk of the embryo with second and third harmonic generation microscopy, respectively. Finally, PAM systems incorporating optical coherence tomography detection have been used to image features including the larval eye, yolk, and swim bladder [206].

While each of these systems is capable of producing striking composite images depicting several unique anatomical features, each system requires specialized optical setups and the use of more than one laser. Furthermore, due to the different illumination pathways employed, no system was capable of simultaneous image acquisition.

We recently reported on a technique, termed photoacoustic radiometry (PAR), that can be used to simultaneously generate PA images as well as optical attenuation images using conventional transmission style OR-PAM [207,208]. In brief, in PAR imaging each laser pulse used to generate a PA signal is attenuated as it propagates through the sample. The attenuated pulse then impinges upon metallic components within the US transducer, generating an additional PA signal within it that can be gated and used to reconstruct images. The amplitude of the PAR signal is directly proportional to the amount of light which is transmitted through the sample and incident on the transducer [207,208]. Attenuation of the laser beam due to both optical absorption and scattering decreases signal amplitude, creating unique contrast in the resultant PAR images. Furthermore, since both PAR and PA signals are generated from a single laser pulse, both signals are acquired in the same RF-line and yield simultaneous co-registered images.

In this work, we demonstrate simultaneous label-free PAR and PA imaging of live zebrafish larvae. PAR images reveal structural features of the gross anatomy, while volumetric PA images depicted single red blood cells (RBC) and the vascular morphology. When merged, the PAR images provide useful landmarks for identifying the vasculature in the PA image. Finally, we applied the technique to study the effects of an anti-angiogenic drug that hinders the development of larval vasculature.

5.3 Methods

5.3.1 System setup

A schematic of the experimental system is shown in Figure 5.1. A SASAM scanning acoustic microscope (Kibero, Saarbruken) built on an Olympus IX-81 microscope modified to include a pulsed 532 nm laser with pulse repetition frequency (PRF) of 4 kHz and pulse width of 330 ps (TeemPhotonics, France) was used for sample scanning. The laser was directed through a variable optical density neutral density (ND) filter and coupled into a single-mode fiber with a 2.5 μm core diameter and NA of 0.13 (Coastal Connections, USA). The collimated laser beam at the fiber output was spatially filtered by an iris and passed through a second ND filter. A portion of the beam was sampled using a 70/30 (T/R) beamsplitter (Thorlabs, USA) and directed to a joulemeter for pulse-to-pulse energy measurement (Gentec-EO, Canada). The transmitted portion of the beam was directed through the right side port of the SASAM and reflected off a dichroic mirror (Chroma Technology Corp., USA) housed in the IX-81 fluorescence cube turret. It was then focused through a 4X optical objective with a NA of 0.1 (Olympus, Japan) onto the sample. The profile of the laser beam was measured using PAR with a knife-edge technique (Figure B.1), and the FWHM of the beam at the focal spot was found to be 5.3 μm . Transmission brightfield and fluorescence images of the samples were acquired by rotating the turret to a fluorescence cube with excitation and emission wavelengths of 480 nm and 520 nm, respectively, and using a CCD camera affixed to the IX-81 left side port for image acquisition. Two different single element transducers were used in this work: a 200 MHz transducer with -6dB bandwidth of 120 MHz, and a 400 MHz transducer with a -6dB

bandwidth of 180 MHz. The lateral/axial resolution of the transducers were calculated to be $8\ \mu\text{m}/11\ \mu\text{m}$ for the 200 MHz transducer, and $4\ \mu\text{m}/7.5\ \mu\text{m}$ for the 400 MHz transducer. PAR signals generated within the transducer and PA signals arriving from the sample were acquired in the same RF-line. Acquired RF-lines were digitized at a rate of 8 Gs/s using a 10 bit digitizer (Acquiris, USA), and were averaged 150 times to increase SNR.



Figure 5.1: Schematic of the experimental setup. A photograph of the components in the dashed box on the left is shown on the right hand side of the image. Abbreviations: ND, neutral density filter; M, mirror; FC, fiber coupler; I, iris; BS, beamsplitter; JM, joulemeter; DM, dichroic mirror; OBJ, objective; TX, transducer; S, brightfield light source.

5.3.2 Preparation of Zebrafish Larvae

The zebrafish were raised using the techniques outlined in [209]. For the present study, two variants of zebrafish larvae were used: the transgenic *Tg (flkl:GFP)* line, which exhibits GFP-expressing endothelial cells [210]; and the mutant *casper* line, which is largely devoid of melanocytes and iridophores [169]. All zebrafish strains were housed and maintained under standard husbandry conditions [196]. To prevent excess melanin production in the *Tg (flkl:GFP)* fish, the embryos were treated with $200\ \mu\text{M}$ of PTU [168]

at 10 hours post fertilization (hpf). For fish treated with the anti-angiogenic drug indirubin-3'-monoxime (I3M, or IRO), 4 μM was added to the zebrafish egg water at 8 hpf. All zebrafish experiments were conducted in accordance with St. Michael's Hospital Animal Care Committee approved protocol ACC403.

A glass-bottom petri dish (MatTek, USA) was filled with 300 μL of molten 1.5% low melting point agarose (Sigma, USA) at 40°C. The agarose was allowed to set in a 4°C fridge for 15 minutes. The zebrafish larvae were anesthetized using a 0.003% (w/v) solution of tricane (Sigma, USA), and pipetted onto the agarose filled petri dishes. Excess egg water was aspirated, and the fish was covered with 20 μL of the molten 40°C agarose. The dishes containing larvae were left to set at room temperature for 30 minutes prior to imaging.

5.3.3 Image formation

The acquired 3D scan datasets were time gated to isolate the PAR and PA signals. The signal envelope for each RF-line was computed, and maximum amplitude projection (MAP) images were generated separately for both the PAR and PA data. For display purposes, the MAP images were smoothed in MATLAB using the *imgaussfilt* function with a standard deviation of 0.75. The *interp2* function was then used for 1-point 2D linear interpolation of the smoothed images. Prior to smoothing, the PA MAP images from scans of *Tg (flk1:GFP)* fish were log compressed, thresholded, and a dilate mask (disk structuring element, radius 1 pixel) was applied to enhance visualization of the vasculature.

5.4 Results & Discussion

5.4.1 *In vivo* Imaging of Transgenic Zebrafish

To our best knowledge, there has been no direct comparison of PA images of the developing zebrafish vasculature with fluorescence microscopy images of the vasculature from the same larva. Towards this end, we acquired fluorescence and PAM images of the same 4 dpf *Tg (flk1:GFP)* zebrafish larvae. Figure 5.2a shows the GFP expressing endothelial cells in the larval zebrafish trunk. The vessels have been pseudo-coloured red to aid with comparison to the PA image. At this stage of development, the most prominent vessels in the trunk are the dorsal aorta (DA) and the posterior cardinal vein (PCV), which run horizontally, and the vertical intersegmental vessels (ISV), which merge at the dorsal side of the zebrafish to form the dorsal longitudinal anastomotic vessel (DLAV) [170]. Figure 5.2b shows the corresponding PA MAP image of the same scan region acquired with the 400 MHz transducer. There is good agreement between the vasculature presented in the fluorescence and PA MAP image, and fine structure like the presence of a bifurcation in one of the ISV's (indicated with an arrow) is preserved. Although the fish was exposed to PTU early in its development, the presence of strongly absorbing melanocytes is noted in the PA image (arrowheads). The signal from the melanin was upwards of 30 dB greater than the signal from the vessels, which may explain why the vasculature is not readily discernable in other PAM scans of wild type embryos [134,203]. When comparing the two images, it appears that PA is unable to resolve several of the vessels present in the fluorescence image, most noticeably the ones between the DA and PCV. However, while both images provide indication of the morphology of the vasculature, the origin of the

contrast in either is fundamentally different. The signal in the fluorescence image is due to GFP sequestered within the endothelial cells, and as such does not discriminate between partially developed and functional vasculature. In contrast, the signal in the PA image originates from RBCs within the vasculature, and therefore, shows only fully formed vessels with lumens that are capable of supporting blood flow (as assessed by RBC transit through the vessel). Taken together, these images provide a more complete overview of the development of the embryonic cardiovascular system, which would otherwise only be possible with double transgenic zebrafish lines expressing fluorescent proteins in both their endothelial cells and RBCs [211].

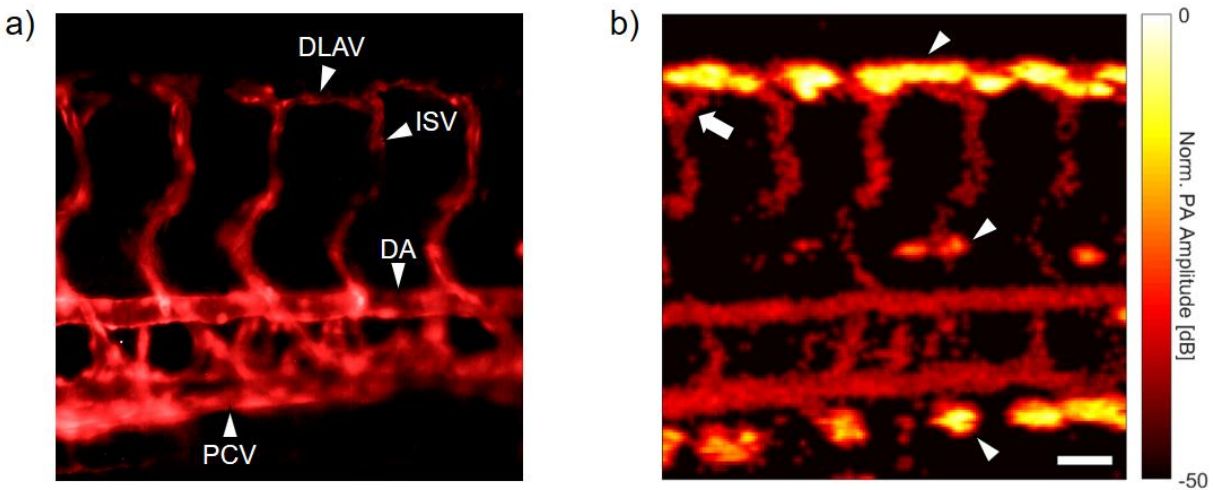


Figure 5.2: a) Fluorescence image of the GFP expressing endothelial cells in the trunk of a *Tg (flkl1:GFP)* larval zebrafish. b) PA image of the same fish. Erythrocytes within the lumenized vessels allow for visualization of perfused vasculature. The arrow denotes a bifurcation in one of the ISVs, while the arrowheads indicate melanin spots. The scale bar is 50 μm and can be applied to both images. DLAV = Dorsal longitudinal anastomotic vessel, ISV = Intersegmental vessel, DA = Dorsal aorta, PCV = Posterior cardinal vein.

In contrast to the homogeneous appearance of the melanophores, the vessels in the PA image have a granular texture, which is most prominent in the ISVs and to a lesser extent in the DA and PCV. The graininess is a result of the motion of the circulating RBCs. When scanning over a vessel, the total number of excited PA sources (i.e. RBCs) within the confocal detection region fluctuates as a function of time, modulating the amplitude of the resultant PA signal. In regions where the RBC flow is sporadic and single file (e.g. the ISVs), it is not guaranteed that any RBCs will enter the excitation zone during the transducer dwell time, resulting in no detectable signal at that segment of the vessel. While it would seem that the granular appearance of the PA image is a disadvantage of the technique, it may in fact present an opportunity to further enhance image resolution. Recently, Chaigne et al. reported a new technique which uses statistical analysis of fluctuations in PA signals resulting from absorber motion for super-resolution optical fluctuation imaging (SOFI) [212]. In contrast to super-resolution ultrasound techniques [213], the PA SOFI approach does not require extremely sparse source distribution, and is thus ideal when imaging samples with endogenous sources like RBCs in microvasculature. Application of the technique to the datasets here (either with endogenous or exogenous contrast agents) may help to further improve resolution of small vessels and reduce background noise.

5.4.2 Simultaneous Duplex Imaging of Zebrafish Larvae

To demonstrate our duplex PAR/PA imaging technique, we then imaged 5 dpf mutant *casper* zebrafish larvae. A brightfield image of the coronal view of a larval zebrafish head is shown in Figure 5.3a. To optimize contrast in the resultant PAR/PA images, we targeted the central region of the head between the eyes (indicated with a dashed box).

The simultaneously acquired PAR and PA images are shown in Figure 5.3b and Figure 5.3c, respectively. The contrast in the PAR image is due to both absorption and scattering of the excitation laser beam as it passes through the head, with dark regions indicating increased optical attenuation. There is good agreement of anatomical features between the brightfield and PAR images. The most apparent are the pharyngeal arches, which are observed at the periphery of the scan region (denoted with arrowheads). These cartilaginous structures offer support for the developing zebrafish jaw, and for the gills which will form between them [214]. The PA scan shown in Figure 5.3c was generated from the same scan data as Figure 5.3b. As in Figure 5.2b, the vessels have a granular appearance indicative of high blood flow. The scan reveals a symmetric distribution of vessels to either side of the image, with the heart at the bottom. The mandibular arch (M), opercular artery (OP), and branchial arches 1 - 4 (B1-4) are readily identifiable upon comparison to literature [170]. As both the PAR and PA images are acquired simultaneously, the two images can easily be overlaid without the need for image scaling or co-registration. An overlay of the PAR and PA images is shown in Figure 5.3d. The overlay provides useful landmarks and context for identifying features in the PA image; for example, demonstrating the expected interleaving of the aortic arches between adjacent pairs of pharyngeal arches [214].

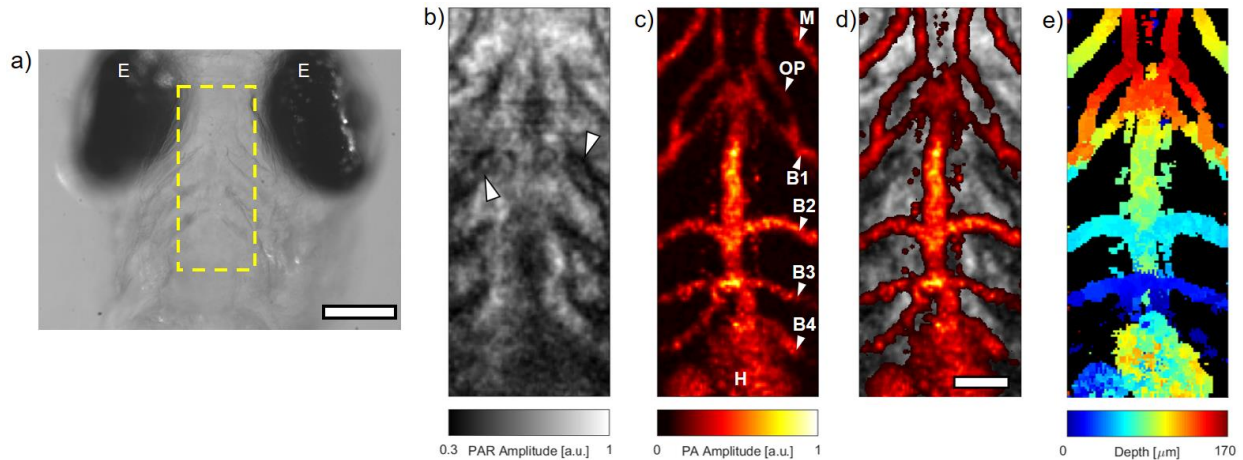


Figure 5.3: a) Brightfield image of the head of a *casper* zebrafish larva. The dashed box indicates the scan ROI. b) PAR image of the ROI. Arrowheads denote the pharyngeal arches. c) PA image acquired from the same dataset used to generate b). The presence of several vessels & the heart is noted. d) Composite PAR & PA image. e) Depth map of PA image. The scale bars in a) and d) are 150 μm and 50 μm , respectively. E = Eye, M = Mandibular arch, OP = Opercular artery, B1-4 = Branchial arches 1-4, H = Heart.

One of the advantages of using ultra high frequency (UHF) transducers is the fine lateral and axial resolution due to the high central frequency and large bandwidth, respectively [31,34,175]. This enables generation of high-resolution volumetric representations of the vascular data (Movie B.1) as well as striking depth-encoded images, such as the one shown in Figure 5.3e. The depth-encoded image displays the relative depth at which the maximal PA signal is found; structures which are closer to the transducer appear as dark blue, while those which are deeper within the larvae appear red. The results here indicate that the arches which are more distal from the heart slope down toward the ventral side of the fish, with the exception of the mandibular arches, which loop back towards the heart and the dorsal side. These results again can be verified by comparison with the expected vascular structure (cf. Figure 6E in [170]).

A scan of the trunk of a second live 5 dpf larvae, with the fish's sagittal plane orthogonal to the transducer, was then performed. The resultant PAR image is shown in Figure 5.4a. The image provides exceptional visualization of the different anatomical structures within the trunk. The rhomboid muscle segments of the trunk (myotomes, M) are separated by the connective tissue of the vertical myosepta (Ms) [214]. The notochord (N), which serves as the primary support structure for the larval fish, is clearly visible, with a slight indication of the central canal (C) segment of the neural tube running immediately dorsal. Finally, the yolk is readily identified at the ventral side of the fish due to its thick contouring and granular appearance.

The simultaneously acquired PA image is shown in Figure 5.4b. As in the case of the transgenic fish, the DA, PCV, ISVs – which have been separated into intersegmental arteries (SA) and veins (SV), and DLAV are all clearly identifiable. The SA and SV can be identified by their origin point, which is either on the DA or PCV, respectively. During angiogenesis, endothelial cells sprout from the DA near the myosepta to form the SA and DLAV; however, most have not yet lumenized and thus do not support circulation [215]. After these structures are established (at approximately 1.5 dpf), secondary sprouts emerge from the PCV and grow dorsally. In cases where these sprouts join with the SAs, the original connection between the SA and DA is severed, and the vessel, now identified as a SV, supports circulatory flow between the DA and the PCV [215]. Individual RBCs (arrows) can be observed in the interstitial space, especially between the DA and PCV in the so called caudal hematopoietic tissue (CHT) region, which is an active region of

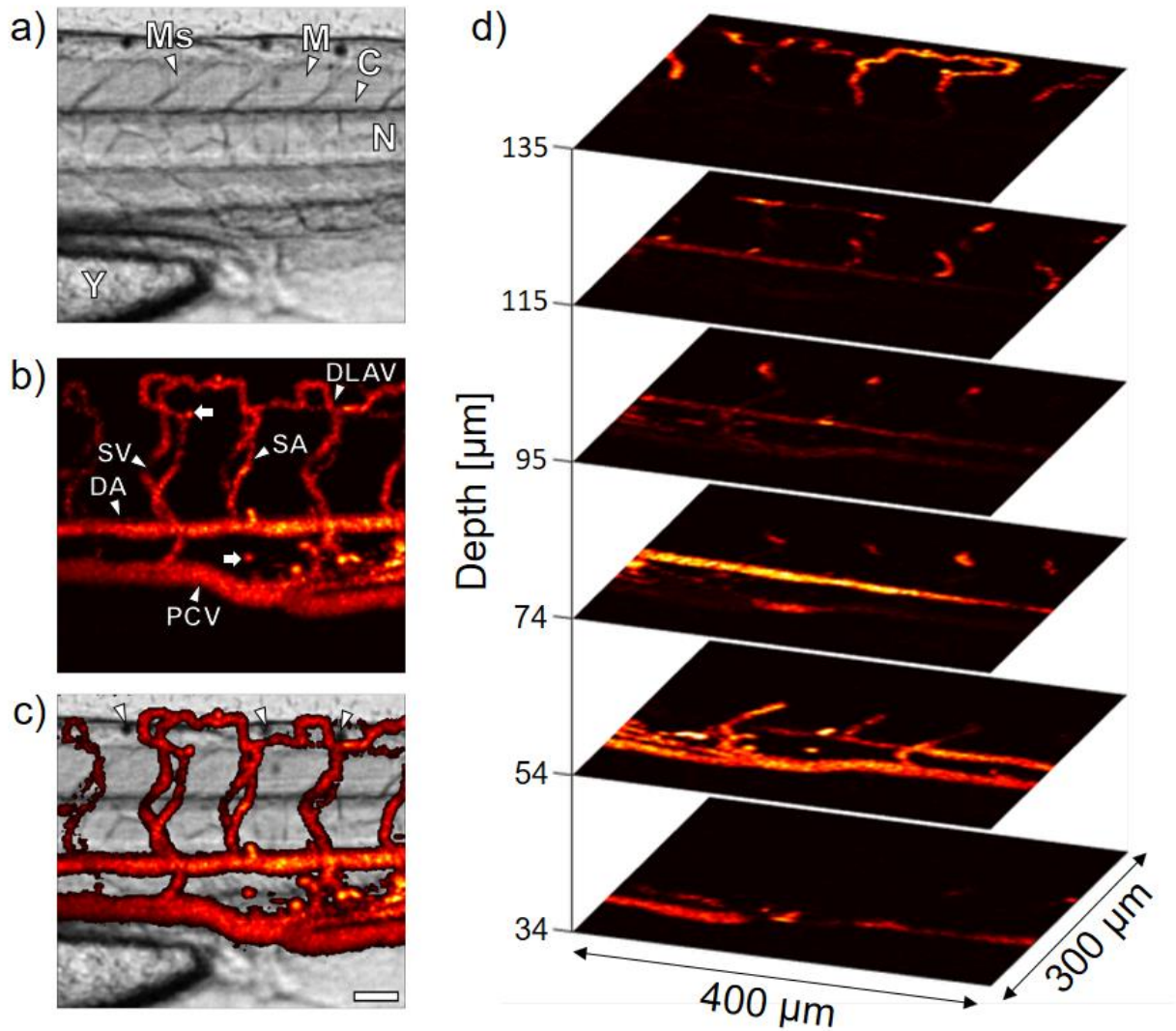


Figure 5.4: a) PAR image of the trunk of a 5 dpf *casper* zebrafish. b) PA image of the trunk vasculature acquired simultaneously with a). c) Composite PAR/PA image. d) PA images at different depths within the larva. The scale bar in c) is 50 μm . Ms = Myosepta, M = Myotome, C = Central canal, N = Notochord, Y = Yolk, DLAV = Dorsal longitudinal anastomotic vessel, SV = Intersegmental vein, SA = Intersegmental artery, DA = Dorsal aorta, PCV = Posterior cardinal vein.

hematopoiesis in the larval fish after 2 dpf [216–218]. Lateral and axial profiles taken through the centre of one such RBC (FWHMs of 10 and 12 μm , respectively) are shown in Figure B.2, and demonstrate the capabilities of the UHF PA technique for resolving individual cells *in vivo*. Owing to the fine lateral and axial resolution, 3D visualizations of the trunk vasculature are possible. A volumetric reconstruction of the PA data is shown in Movie B.2. Sagittal planes within the 3D PA dataset are presented in Figure 5.4d, demonstrating the arrangement of the functional trunk vasculature. Each slice is separated by $\sim 20 \mu\text{m}$ in the axial direction. In addition to making it easier to identify vasculature at different planes in the fish, the slices further demonstrate that the fish is tilted with respect to the transducer, with the PCV being closest and the DLAV furthest away.

As seen in Movie B.2, the ISVs form a shape reminiscent of a ‘Figure-8’ in the transverse cross section. The overlay of the PAR and PA images shown in Figure 5.4d, provides context for this configuration. With the overlay, it can be seen that the ISVs must be superficially rerouted around both the notochord (which is immediately dorsal to the DA) and the neural tube, which is further dorsal to the notochord. Without the landmarks provided in the PAR image, histological techniques, which require fixation of the fish, would be required to obtain these insights. Of particular interest in the overlaid image are three dark spots (arrowheads). As evidenced by the PAR image, these regions are highly attenuating to the incident laser beam; however, they were found to produce no detectable PA signal. We hypothesize that these dark spots are iridophores, which are a type of pigment cell responsible for the silvery appearance of the adult fish. Iridophores contain a large number of reflective crystalline platelets which effectively form a stack of thin-films

that scatter incident light [219,220]. It should be noted that casper zebrafish are expected to be completely devoid of iridophores [169]; however, several observations of the images in this and the proceeding section suggest that this may not always be the case. First, the location of the suspected iridophores in the PAR image is the dorsal side of the neural tube, which is where pigmentation cells develop in the larvae before migrating to their final location in the body [200,219]. Secondly, owing to their optical properties, iridophores were expected to be sources of strong contrast in PAR images but undetectable in PAM, consistent with Figure 5.4a and Figure 5.4b. Finally, the brightfield images of an equivalent dark region in the PAR image of a different *casper* zebrafish taken with the transducer blocking the central beam of the light source reveals that these spots are highly reflective. This is consistent with the expected appearance of the larval zebrafish iridophores under epi-illumination conditions (cf. Figures 1 and 3 in [221]).

5.4.3 Inhibition of Vascular Growth

It has previously been demonstrated that I₃M is a potent inhibitor of ISV angiogenesis in larval zebrafish models [222,223]. As demonstrated in Figure 5.5a, the number of ISVs in the trunk of the *Tg (flk1:GFP)* larvae decreases with increasing I₃M concentration. Typically, transgenic zebrafish lines expressing fluorescent proteins in their endothelial cells must be used to observe the effects of the anti-angiogenic drug; however, it would be useful to assess these effects in the easily accessible wild type larvae also. Towards this end, we imaged I₃M treated casper zebrafish larvae using the PAR/PA technique.

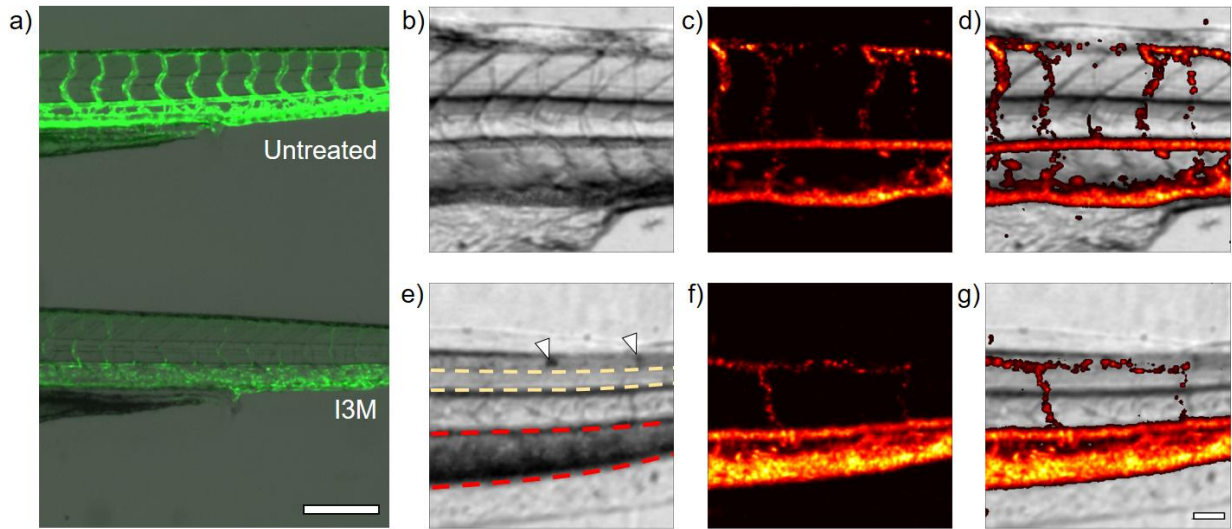


Figure 5.5: a) Fluorescence image of vasculature in the trunk of an untreated (top) and I₃M treated (bottom) *Tg (flk1:GFP)* larval zebrafish. I₃M is a potent inhibitor of angiogenesis, and fewer ISVs are formed in the treated fish. b) – d) PAR, PA, and composite images, respectively, of an untreated larva. Corresponding images for an I₃M treated fish are shown in e) – g). In e), arrowheads mark the location of iridophores, while the yellow contoured area is the neural tube, and the red contoured region has an excess of RBCs. The scale bar in a) is 250 μ m. The scale bar in g) is 50 μ m, and can be applied to b) – g).

Simultaneously acquired PAR, PA, and composite images of an untreated larva are shown in Figure 5.5b–d, respectively. Equivalent images of an I₃M treated larva are shown in Figure 5.5e–g. Comparing the PAR images, the myosepta are much more prominent in the untreated larva, while the neural tube (yellow contour) is more readily visible in the treated fish. As I₃M only affects developing vasculature, these differences could potentially be attributed to different focusing of the optical objective within the fish trunk. In the treated fish, a conspicuous dark region ventral to the notochord is observed (red contour), along with iridophores (arrowheads), whose presence is verified with brightfield microscopy (Figure B.3). There appear to be two major differences in the appearance of the PA images of treated vs. untreated fish. First, as expected, the treated fish has fewer

ISVs in the scan ROI than the untreated fish. Second, while the appearance of the DA is similar in both images, the appearance of the PCV is markedly different even though both scans were acquired near the same anatomical location. One possible explanation for this is the expansion of the vessel to accommodate a larger RBC load due to loss of supporting ISV vasculature. In addition to showing the organization of the vasculature, the composite images reveal that the dark region noted in Figure 5.5e is a result of the increased attenuation due to the enlarged PCV size.

It should be noted that I₃M has a deep red colour, which dyes the zebrafish yolk sac [222] and causes it to produce strong PA signals (data not shown). This limits the PAR/PA technique to ROIs that are devoid of yolk, which would otherwise overwhelm the PA signal from the vessels. Nevertheless, the results of this preliminary investigation indicate that our dual modality technique could be an effective tool for assessing the effects of antiangiogenic drugs on zebrafish larvae. In the future we plan to assess the impact of higher I₃M concentrations on both the anatomy and vasculature of developing wild type zebrafish, as well as investigate the effects of other drugs such as statins, which may be involved in vascular stability and intracerebral hemorrhages [224–226].

5.5 Conclusion

The PAR images made it possible to identify anatomical structures including the myotomes, notochord and yolk; while the PA images made it possible to visualize the head and trunk vasculature with single cell resolution. While this represents the first time simultaneous images of this nature have been acquired using only OR-PAM, there are

some inherent limitations to our technique. First, as with all UHF studies, high acoustic attenuation limits the depth at which high SNR signals can be acquired [31]. This restricts the described dual modality technique to whole-body imaging of larval fish, or to regions less than 100 μm deep at higher frequencies (e.g. 1 GHz) in older fish. Another limitation of the current system is the scanning time. A 160×160 point raster scan currently takes approximately 30 minutes; however, we plan to reduce this scan time by incorporating a laser with a higher PRF. In summary, we have demonstrated a simultaneous label-free technique for imaging the anatomy and vasculature of transgenic and mutant *casper* zebrafish larvae *in vivo* with single cell resolution. We believe that our technique will find applications in studying gold nanoparticle aggregation in the tissue, and the progression of cancer metastasis.

5.6 Acknowledgements

The authors would like to thank Eno Hysi and Eric Strohm for their helpful conversations. This research was supported, in part, by: the Natural Sciences and Engineering Research Council of Canada [grant numbers RGPIN-2017-06496 (MCK) & RGPIN 05389-14 (XYW)], the Canadian Cancer Society [grant number 702161 (MCK)], the Canadian Foundation for Innovation [grant number 30994 (MCK) & 26233 (XYW)], the Ontario Ministry for Research and Innovation [grant number 30994 (MCK)], and the Terry Fox Foundation [grant number 1034 (MCK)].

Chapter 6

Conclusions and Future Work

6.1 Summary of Findings

The techniques described in this dissertation represent contributions to the areas of photoacoustic single-cell analysis as well as PA imaging and image reconstruction techniques. This section summarizes the findings and contributions of the preceding four Chapters.

6.1.1 Assessment of the N:C Ratio of single cells

This Chapter investigated the use of quantitative frequency domain analysis techniques for determining the morphological parameters of cancer cells and their organelles. An UHF-PAM system was used to interrogate live MCF-7 breast cancer cells which had been stained with the DRAQ5 nuclear stain. A transducer with a central frequency of 375 MHz was used in pulse-echo mode to insonify individual cells and record the backscattered US waves. The cell radius was determined by comparing the power spectrum of the recorded echoes to well established analytical solutions for US backscatter from spherical droplets. A 532 nm laser was then used to illuminate the same cell, resulting in the production of PA waves from the cell nucleus by virtue of the nuclear dye. A new derivation for the power spectrum of the PA wave generated by a liquid droplet suspended in a coupling medium with similar acoustic properties was presented. This formalism was then used to ascertain the radius of the cell nuclei by matching the location of spectral

minima in the experimentally measured power spectra to the theoretical model. The mean cell radius as determined by US was $15.5 \mu\text{m} \pm 1.8 \mu\text{m}$, and the mean nucleus radius determined by PA was $12.0 \mu\text{m} \pm 1.3 \mu\text{m}$; both values were in agreement with previously reported cell and nucleus sizes for this cell type. A nucleus-to-cytoplasmic (N:C) ratio was calculated for each individual cell using the cell and nucleus diameters derived from the fits to the experimental data. The mean N:C ratio was 1.9 ± 1.0 , corresponding to nuclei which occupy approximately 50% of the total cell volume compared to the standard 10% for normal cells.

The microscopy techniques prevalently used for the assessment of N:C ratios in histology are time consuming at both the sample preparation and measurement stages, and are subject to an inherent operator bias [227]. In addition, N:C values derived from histology are based upon thin cross-sections of the cells, which may not provide accurate representations of the true 3D cell morphology. In this regard, the sound-based US and PA approaches for cell and nucleus sizing are advantageous, as the described spectral fitting techniques are sensitive to the 3D structures of the cell and nucleus, respectively. Further, while the measurements on the stationary cells presented in this Chapter do not offer a distinct benefit in rapid analysis times, future work (discussed in Chapter 6.2.1) involves incorporating the described analysis techniques into an acoustic/photoacoustic flow cytometry system capable of high-throughput cell measurement. We postulate that this flow technique could be used to rapidly differentiate between normal and cancerous cells, or to detect the presence of cancerous cells in a blood

sample based on the cell size, nucleus size, and N:C ratio. The signal analysis techniques developed in this Chapter are critical for achieving this.

6.1.2 F-Mode Imaging

The image formation techniques currently used in PAM are implemented in the time domain, and as a result, cannot be used to easily extract the rich structural information that is encoded in the power spectra of the broadband PA waves. Techniques like maximum amplitude projection discard all data in the time domain, resulting in 2D representations of chromophore distribution which lack structural information in the axial dimension. As shown in Chapter 2, the frequency domain power spectra of PA signals are extremely sensitive to sub-resolution variations in 3D absorber morphology; however, this sensitivity *has never been leveraged for image reconstruction purposes*. This Chapter demonstrates an approach that utilizes spectral features as a source of structure and scale dependent image contrast in PA imaging.

The developed F-Mode technique was applied to PA scans of phantoms and biological samples with varying structure and scale. To demonstrate robustness to the technique used for PA data acquisition, F-Mode was implemented on data obtained using both a PAT system (40 MHz transducer central frequency) and a UHF-PAM system (80, 200, and 400 MHz transducer central frequencies). After data acquisition, the PA power spectra were computed as in Chapter 2 for the RF data acquired at each scan location. Each of the resultant power spectra were partitioned into discrete bands, and the power in each band was computed. F-Mode images were created for each frequency band using the relative power at each scan location as a means of generating image contrast.

In the PAT experiments, a gelatin phantom containing cylindrical vessels with diameters of 150, 200, and 250 μm was scanned. With the conventional MAP reconstruction, all vessels appeared with little variation in appearance and similar intensity in the resultant image. After application of the F-Mode technique, instances where only one of the three vessels, or where specific combinations of the vessels, were visible were identified in the image stack. These images occurred when the selected frequency band had a significant difference in the computed power for either one or two of the vessels with respect to the others. Not only do these results demonstrate that the F-Mode technique can be applied to data acquired with linear array transducers at pre-clinical frequencies (40 MHz), but it also points towards potential application of the technique to other vessels with the same approximate diameter, such as subcutaneous arteries in humans.

For the UHF-PAM measurements, three samples were scanned with transducers having different central frequencies. To investigate the applicability of F-Mode at higher frequencies, first a gelatin phantom (transducer central frequency of 400 MHz) containing a heterogeneous population of black microspheres with diameters of 6 and 10 μm was scanned. Microspheres are commonly used as calibration targets in microscopic imaging systems, and due to their size and coloration, are ideal candidates for F-Mode. As in the vessel phantom, with the conventional MAP technique alone it was not possible to isolate either population of microspheres in the resultant image. Application of F-Mode made isolation and selection possible. The power spectra from the beads was approximately equal at 326 MHz, with the larger bead dominating at lower frequencies, and the smaller bead dominating at higher frequencies.

After the proof-of-concept phantom applications, the F-Mode technique was applied to data acquired from PAM scans of biological samples. F-Mode images of unstained biological cells (acquired with a transducer central frequency of 200 MHz) demonstrated that organelles such as the nucleoli could be accentuated in the images through selection of the appropriate frequency band for image generation. Finally, the F-Mode images of data acquired from UHF-PAM scans of live zebrafish larvae (transducer central frequency 80 MHz) were generated. Images which accentuated the different vessels of the larval trunk – the dorsal aorta, posterior cardinal vein, and an intersegmental vessel – were generated. The visualization of objects of interest in biomedical images is often confounded by the presence of other intervening structures, noise, or poor contrast. In some cases, windowing or thresholding can be applied to reduce image clutter; but this is not always possible for complex geometries. With F-Mode, it is possible to generate dynamic displays of structural information that cannot be achieved with conventional PA reconstruction techniques. This makes it possible to isolate (or exclude) absorbers of different scale from image datasets to generate new contrast that was previously inaccessible with other PA approaches. Ultimately, the F-Mode technique presented in this Chapter could have applications in the selective enhancement of features or structures of different size (e.g. arteries vs capillaries, nuclei vs nucleoli) in other small animal models (e.g. rodents), or superficial vessels in humans.

6.1.3 Description and Applications of PAR Imaging

In this Chapter, a new technique for sensing and constructing images based on the optical attenuation properties of microscopic samples was presented. In our transmission-

mode UHF-PAM setup, each laser pulse generates both a PAR and a PA signal which are detected in the same RF-line. By simultaneously operating the transducer in pulse-echo mode, triplex PAR/PA/US imaging can be achieved. While the exact source of the PAR signal within the transducer cannot be determined with certainty through non-destructive methods, it is hypothesized that it is caused by direct PA excitation of the transducer active element. This claim is supported by the following observations. First, PAR signals can be generated via direct illumination of the transducer, even when no sample is present. Thus, the PAR signal must be generated within the transducer itself. Second, the PAR signal is detected almost immediately after the laser is fired. If the signal was generated by an inclusion within the buffer rod (or on its surface), there would be a significant time delay while the resultant acoustic waves propagate to the active element to be detected. Going forward, we plan to compare the sensitivity of the PAR signal to that of other optical detectors, such as photodiodes and joulemeters, to further characterize the PAR sensing technique.

Direct illumination of the transducer was used for characterization purposes; determining the sensitivity (>1 nJ pulse energy for $\text{SNR} > 5$) and lateral resolution ($1.64 \mu\text{m}$ for a 532 nm laser and 0.25 NA objective) of the technique. After characterization, an etched glass-bottom petri dish was scanned to show that the contrast in PAR images is derived from optical attenuation, and not solely absorption as in the case of PAM. Even though the optical absorption in the glass is negligible at the laser illumination wavelengths used, high fidelity images of the alpha-numeric lettering on the dish could be resolved, with particularly high contrast at the edges of the etched channels. This

demonstrates that the PAR technique can generate images of samples with negligible optical absorption at the incident laser wavelength; a feat which cannot be achieved when using conventional PAM imaging alone.

Multiplex imaging using the PAR technique was then explored. First, a CAKI-2 cancer cell stained with the nuclear targeting DRAQ5 dye was scanned with simultaneous PAR and PA acquisition. Intracellular organelles such as the cell nucleus, nucleoli, and endoplasmic reticulum were identified in the resultant PAR image, along with the periphery of the cell membrane. The signal in the simultaneously acquired PA image was localized to the cell nucleus due to the DNA specificity of the dye uptake. When merged, the appearance of the combined PAR and PA image was in good agreement with a combined DIC and fluorescence microscopy image. Next, a simultaneous triplex PAR/PA/US image of a silicon wafer die was acquired using the 200 MHz transducer and a 1064 nm laser. Each modality generated images with micron-scale resolution and unique image contrast that accentuated different features of the integrated circuit. PAR was sensitive to imperfections on the bottom of the wafer, while PA exhibited the most detail within the metallized regions, and US showed surface features and regions of high contrast the edges of the metallized regions.

Conventional PAM techniques can only be used to image samples containing features that have optical absorption significant enough to yield detectable PA signals. In comparison, the unique way in which the PAR signal is generated means that optically attenuating features previously undetectable with PAM (e.g. the cytoplasm of unstained biological cells) are now readily imaged in a co-registered manner with the PAM signal.

While simultaneous high-resolution PAR/PA/US scanning is only achievable with UHF-PAM systems, in principle, PAR/PA imaging can be implemented in any transmission mode OR-PAM setup with no modification to existing hardware. In conclusion, this multiplex imaging technique opens up new possibilities for analysis of both biological and fabricated samples, and is highly advantageous when imaging samples – such as the zebrafish larvae in Chapter 5 – with scant optical absorption.

6.1.4 Zebrafish Imaging

In this Chapter the duplex PAR/PA imaging technique presented in Chapter 4 was used to image live zebrafish larvae. In addition to demonstrating the efficacy of the simultaneous imaging technique, this is the first study utilizing frequencies above 200 MHz for *in vivo* PAM. The advantage of using UHF transducers for *in vivo* PAM studies is that they provide axial resolution on the order of a single-cell, enabling high-resolution 3D PA reconstructions of the larval vasculature. Furthermore, when combined with the PAR imaging techniques introduced in Chapter 4, the resulting composite images include anatomical features which can serve as indicators which aid in the identification of specific vessels.

Transgenic larvae treated with a pigment suppressing drug (PTU), as well as transparent *casper* larvae were imaged using a 532 nm laser focused through a 4X optical objective. The ability to resolve the zebrafish vasculature with UHF-PAM was assessed by comparing the PA MAP images to GFP fluorescence images in transgenic fish. The fluorescence image shows the endothelial cells forming the vasculature, while the MAP image derives contrast from the RBCs within it; nevertheless, good agreement between the

two images was observed. Furthermore, since only the vessels containing RBCs produce a PA signal, the MAP images enable distinction of vessels which support blood flow from those which are not yet functional.

Simultaneous PAR/PA images were then acquired for both the larval head and trunk. Attenuation of the laser by the zebrafish tissue resulted in PAR images which showed anatomical features including cartilage, muscle segments, and the notochord. The PA images of the same regions revealed the 3D structure of the vasculature. The combined PAR/PA images allowed for visualization of the vasculature *in situ* within the context of the fish anatomy. When applied to zebrafish treated with an anti-angiogenic drug, the dual technique revealed atypical vascular organization, as well as the reduced number of intersegmental vessels in the fish trunk. This pioneering study paves the way for future work investigating tumour development and metastasis *in vivo* (to be described further in the Chapter 6.2.2).

6.2 Future Work

6.2.1 High-throughput N:C assessment

The results from Chapter 2 demonstrate that frequency domain techniques can be used to determine the N:C ratio of living cells. As discussed in that Chapter, it would be of great interest to be able to use these techniques to identify different cell populations, such as circulating tumour cells (CTC), in a human blood sample [228]. As CTC numbers are sometimes as low as 1 CTC per 1 billion RBCs [229], the manual nature of the UHF-PAM measurements, which results in long acquisition times, small sample sizes, and inherent

operator bias, are inadequate. High throughput measurement techniques are necessary. Towards this end, our lab has been developing and testing an acoustic/photoacoustic flow cytometer (APFC) [124] which is capable of acquiring US and PA signals at a rate of hundreds of cells per minute. Here I present preliminary data on UHF-PAM measurements, and then compare these to measurements using APFC and Imaging Flow Cytometry (IFC).

Before the system can be used for detecting anomalous cells in a blood sample, the ability of the UHF-PAM technique to differentiate between different types of nucleated cells, and further, the ability of the flow system to employ these techniques to acquire accurate population statistics must be ascertained. To test the former, three different cell types, MCF7 breast cancer ($n = 37$), PC3 prostate cancer ($n = 43$) and MDA-MB-231 (MDA) breast cancer ($n = 43$), were measured using the techniques of Chapter 2. The results are summarized in Figure 6.1. The mean cell and nucleus diameters were: $15.2 \pm 3.5 \mu\text{m}$ and $10.2 \pm 3.5 \mu\text{m}$, respectively for the MCF-7 cells; $15.5 \pm 2.9 \mu\text{m}$ and $10.2 \pm 3.6 \mu\text{m}$, respectively, for the PC3 cells, and $14.2 \pm 3.0 \mu\text{m}$ and $7.5 \pm 2.9 \mu\text{m}$, respectively for the MDA cells. A two-sample t-test was used to test for similarity between the means of the three populations. A statistically significant difference ($p < 0.05$) was observed between the mean diameter of the PC3 and MDA cells; however, no statistically significant difference was observed when the other combinations of cell types were compared. In contrast, a significant difference ($p < 0.001$) was observed for the means of the nucleus diameter when comparing either the MCF-7 or PC3 populations with the MDA.

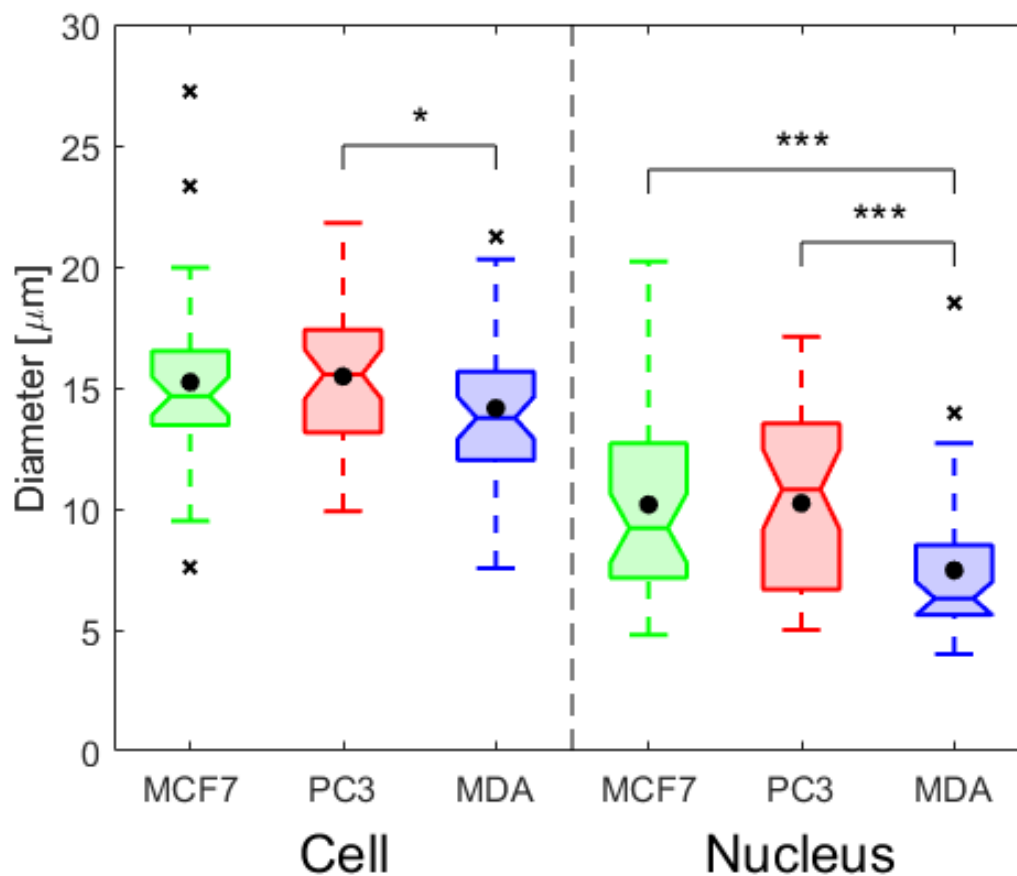


Figure 6.1: Box-and-whisker plots of the calculated cell and nucleus diameters for MCF-7 (green) PC₃ (red) and MDA-MB-231 (blue) cells. The median values for each dataset are indicated by notched horizontal lines, while the mean values are indicated with black circles, and outliers with black x's.

Using the measured values for the cell and nucleus diameters, the N:C ratio was calculated on a cell-by-cell basis. The mean N:C ratios for the MCF-7, PC₃ and MDA cells were found to be 2.9 ± 5.9 , 1.9 ± 2.9 , and 1.3 ± 3.3 , respectively. The large standard deviation for these values can be attributed to outliers in the data, as shown in Figure 6.2a. For these data points, the fit nucleus diameter was above 90% of the cell diameter, causing instability in the denominator of Equation 2.10. The high N:C ratios that result skew the population mean and increase the variance in the N:C data. Alternatively, if the N:C ratio is calculated

as the ratio of the measured nucleus diameter to that of the measured cell diameter, the mean N:C ratios become 0.68 ± 0.19 , 0.66 ± 0.19 , and 0.54 ± 0.19 for the MCF-7, PC₃, and MDA cells, respectively. Box-and-whisker plots showing the resultant distribution of N:C ratios are shown in Figure 6.2b. While no statistically significant differences were observed between the mean N:C ratios derived using Equation 2.10, significant differences ($p < 0.01$) were found when comparing the nucleus/cell diameter ratios for the MCF-7 and MDA, and PC₃ and MDA cells. A summary of all stationary cell measurements is provided in Table 6.1.

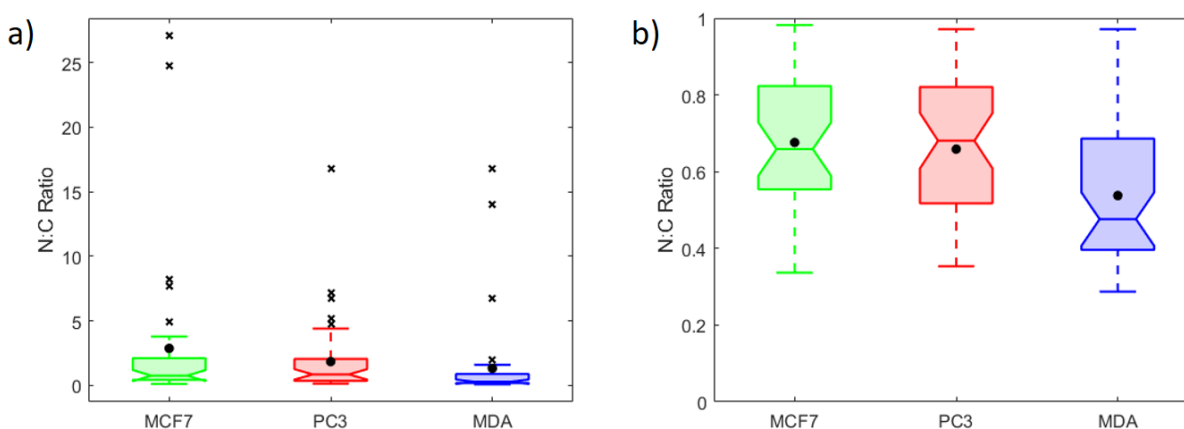


Figure 6.2: a) Box-and-whisker plot of the N:C ratios calculated using Equation 2.10. b) Box-and-whisker plot of the N:C values calculated as the ratio of nucleus diameter to cell diameter.

Due to the similarity in the cell diameters, cell size alone could not be used as a reliable metric for identification of cell type. However, when the nucleus and N:C are also considered, differentiation of the MDA cells from the other two cell lines becomes feasible. While this limits the applications of the US/PA differentiation technique for discriminating between different malignant cell lines, it should not greatly affect the technique's ability to detect CTCs in a blood sample. Most leukocytes in the blood are

between 8 – 11 μm in diameter, enabling the detection of CTCs in the blood by size based techniques (e.g. filtration) alone [230,231]. However, techniques based solely on cell size can misclassify large leukocytes and small CTCs. Consideration of additional metrics such as the nucleus size and N:C ratio could further improve the sensitivity of current size-based techniques.

<i>Cell Line</i>	<i>Cell Diameter [μm]</i>	<i>Nucleus Diameter [μm]</i>	<i>N:C Ratio</i>
<i>MCF-7</i> (<i>n = 37</i>)	15.2 \pm 3.5	10.2 \pm 3.5	0.68 \pm 0.19
<i>PC3</i> (<i>n = 43</i>)	15.5 \pm 2.9	10.2 \pm 3.6	0.66 \pm 0.19
<i>MDA-MB-231</i> (<i>n = 43</i>)	14.2 \pm 3.0	7.5 \pm 2.9	0.54 \pm 0.19

Table 6.1: The mean values for the cell diameter, nucleus diameter, and N:C ratio calculated for the three different cell lines.

Next, a three-way comparison study between the static SASAM measurements, the APFC, and an IFC was performed. The IFC is capable of simultaneously acquiring brightfield and fluorescence images of cells flowing single file through a target region [99–101]. Through the use of masks, cross sectional areas of the cell (brightfield) and nucleus (fluorescence) can be calculated for thousands of cells in a matter of minutes [101]. For this experiment, the IFC was used as a means for optically determining the mean cell and nucleus diameters, and validating the values derived from the spectral fitting techniques.

For both flow systems, the PC₃ cells from the same passage as the static experiments were stained with DRAQ5. The IFC measurements (n = 4654) reported mean

cell and nucleus diameters of 18.3 ± 2.2 and 12.2 ± 1.9 , respectively. Again calculating the N:C ratio as the ratio of the nucleus diameter to the total cell diameter, the mean IFC derived N:C ratio was 0.67 ± 0.07 . Using the APFC, US and PA signals were acquired from a total of 793 cells. Using the techniques of Chapter 2, the mean cell and nucleus diameter values were found to be 16.9 ± 3.9 and $8.5 \pm 2.5 \mu\text{m}$, respectively. The mean N:C ratio was 0.53 ± 0.2 . Currently, optical techniques are the standard means of assessing cell/nucleus morphology and N:C ratio. The good agreement between the APFC and IFC results presented here serves as a demonstration of the applicability of our high-throughput acoustic and photoacoustic technique for reliably determining cell and nucleus diameter.

<i>System</i>	<i>Cell Diameter [μm]</i>	<i>Nucleus Diameter [μm]</i>	<i>N:C Ratio</i>
SASAM (<i>n</i> = 43)	15.5 ± 2.9	10.2 ± 3.6	0.66 ± 0.19
APFC (<i>n</i> = 793)	16.9 ± 3.9	8.5 ± 2.5	0.53 ± 0.2
IFC (<i>n</i> = 4654)	18.3 ± 2.2	12.2 ± 1.9	0.67 ± 0.07

Table 6.2: Comparison of the cell diameter, nucleus diameter, and N:C ratio determined using different systems from the same population of PC₃ cells.

This proof of concept experiment is promising; however, further refinement of the APFC device is required before whole blood samples can be considered. Currently the sensitivity of the APFC system is low – approximately 5% of cells which are flowed through the device are detected. Of those detection events, approximately half contain both US and PA signals with SNR great enough to be used for signal analysis. Modification of the system to be more robust to alignment of the US transducer and laser focus, as well as

improvements to flow focusing techniques for increased detection yield is an area of current focus [232–235]. Integration of higher PRF lasers (in the tens of kHz) into the system is also an area being investigated. This is beneficial as it would allow for the acquisition of a higher number of PA signals while the cells are in the confocal US/PA detection region, in turn increasing the SNR in the RF data through higher signal averaging.

6.2.2 Future Directions in UHF-PAM of Zebrafish Larvae

The work of Chapters 3 and 5 demonstrates that zebrafish larvae can be used as *in vivo* models for UHF-PAM studies. The main focus of these Chapters was to assess the applicability of novel UHF-PAM techniques (i.e. F-Mode and PAR) *in vivo*; however, zebrafish models are highly versatile and there are several opportunities for future work aimed at obtaining a better understanding of basic biological processes. For example, Chapter 5 showed the effects of an anti-angiogenic drug on the zebrafish vasculature; however, other drug studies which examine toxic side effects, and drug induced developmental abnormalities have also been undertaken [236]. In particular, the multiplex imaging techniques described in Chapters 4 and 5 may be useful for studying abnormal formation of the central nervous system, and organs like the heart, and ear [237].

Xenotransplantation of human cancer cells for the purposes of investigating cancer progression and the efficacy of chemotherapeutic drugs is also an area of interest which can be explored with the techniques described in this dissertation. For the first 4 - 6 weeks of their life, zebrafish do not have a fully developed adaptive immune system response [238], and therefore immunocompromised animals need not be used as in the case of

murine models. To date, successful xenografts of human breast cancer, leukemia, melanoma, and prostate cancers, among others, have been demonstrated [236]. In some cases, tumour cells were able to proliferate and migrate through the circulation to form micrometastases elsewhere in the fish body as early as 24 hours post injection [239]. Using transparent zebrafish like the *casper* mutant, and transplanting cancer cells with endogenous pigmentation (such as melanoma cells [169]), opens up opportunities for investigating both cancer cell proliferation, metastasis, and treatment response with UHF-PAM. A main goal of future work will be leveraging the single-cell resolution of UHF-PAM to monitor the development of tumours and metastasis with the imaging techniques presented in Chapters 3 - 5.

Finally, while the potential of using the APFC for *ex vivo* CTC detection in blood samples was discussed, *in vivo* detection of CTCs with photoacoustic flow cytometry is also an area of developing interest. Several works using targeted and label-free PA detection of CTCs have already been performed in murine models [107], and it is the author's hypothesis that these techniques can be extended to zebrafish models as well. Due to the low central frequency of the transducers used in previous PAFC implementations (<40 MHz), the systems are restricted to classifying detected signals as originating from CTCs based solely on the amplitude of the detected PA signals. As such, these systems are binary and can only provide CTC counts. By combining the UHF-PAM techniques of Chapter 2 with the zebrafish xenograft model, an *in vivo* PAFC technique where the morphological properties of individual CTCs flowing in zebrafish capillaries can be determined may be achievable,

potentially increasing both the sensitivity and specificity of current photoacoustic flow cytometry techniques.

6.3 Conclusions

The work presented in this dissertation opens the door to new research possibilities in the field of PAM. The described frequency domain spectral analysis techniques enable non-optical assessment of cell and nucleus morphology, and can be translated to high-throughput UHF cell classification systems. On the other hand, the image reconstruction and acquisition techniques developed utilize contrast mechanisms never before leveraged in PAM imaging; expanding the sensitivity of the technique to absorbers of different scale, and enabling label-free imaging of biological specimens with scant optical absorption. Applications of the described techniques for the purposes of CTC detection, and for monitoring cancer metastasis and treatment response were discussed, and will be explored further in future work.

Appendix A – Supplementary Information for Chapter 3

The following Figures and Movies were included as supplementary information for the manuscript that Chapter 3 is based on. (*M. J. Moore, et al., “Photoacoustic Frequency Mode (F-Mode) Imaging: Scale-specific Contrast from Organelles to Organisms,” (Submitted for publication, Communications Physics, June 2018)*).

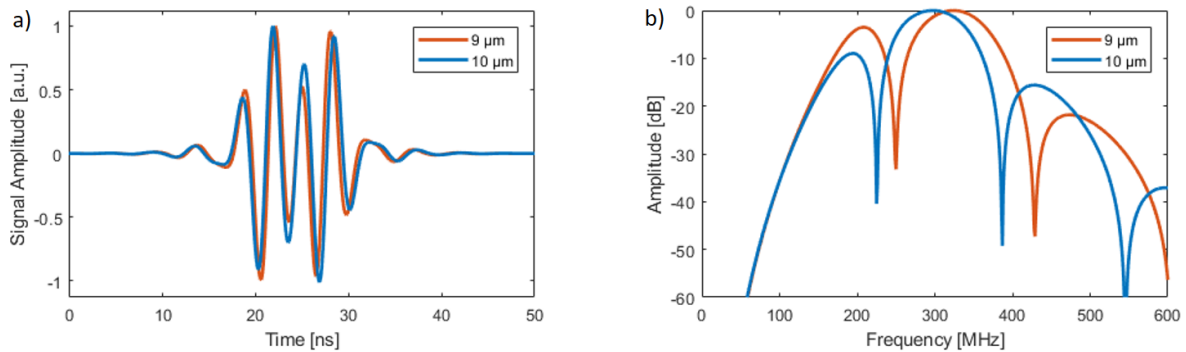
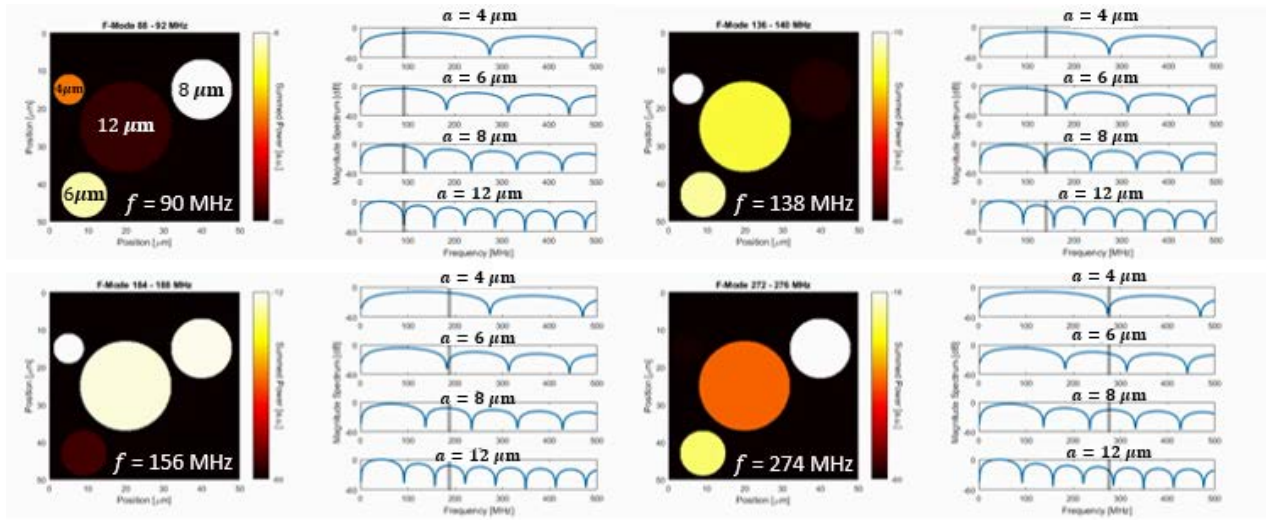
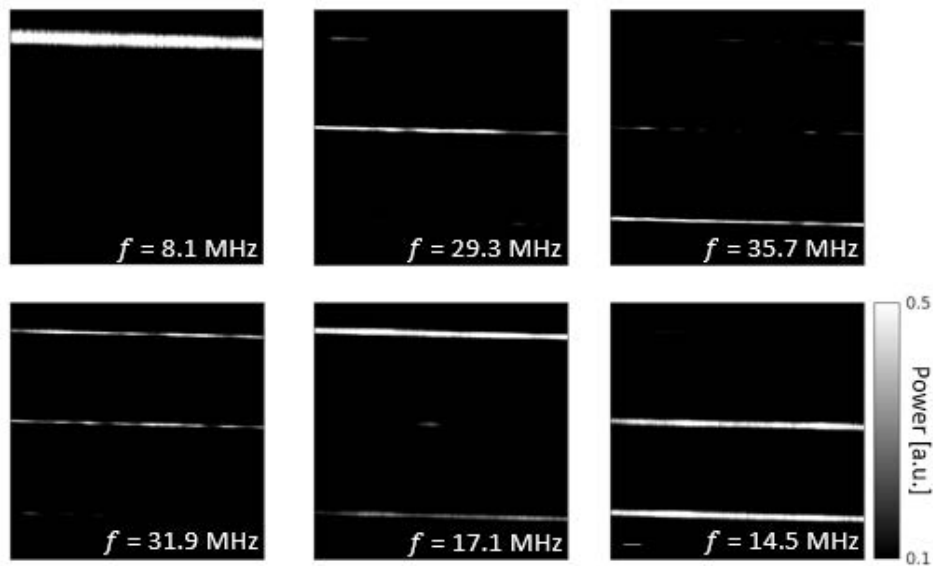


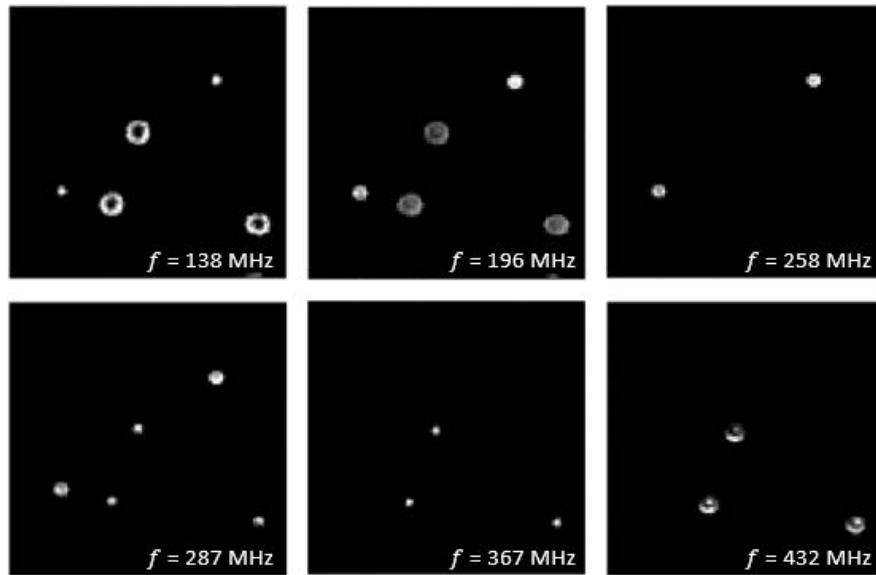
Figure A.1: a) The PA emission from a 9 μm liquid droplet (orange) 10 μm liquid droplet (blue). Analytical waveforms were filtered using a frequency domain bandpass filter centered at 400 MHz with -6dB bandwidth of 200 MHz to simulate the bandpass effects of the receiving transducer. It is extremely difficult to differentiate the two beads in the time domain. b) The FFT of the waveforms shown in a). There is significant difference in the location of spectral minima in the frequency domain, allowing the two beads to be distinguished.



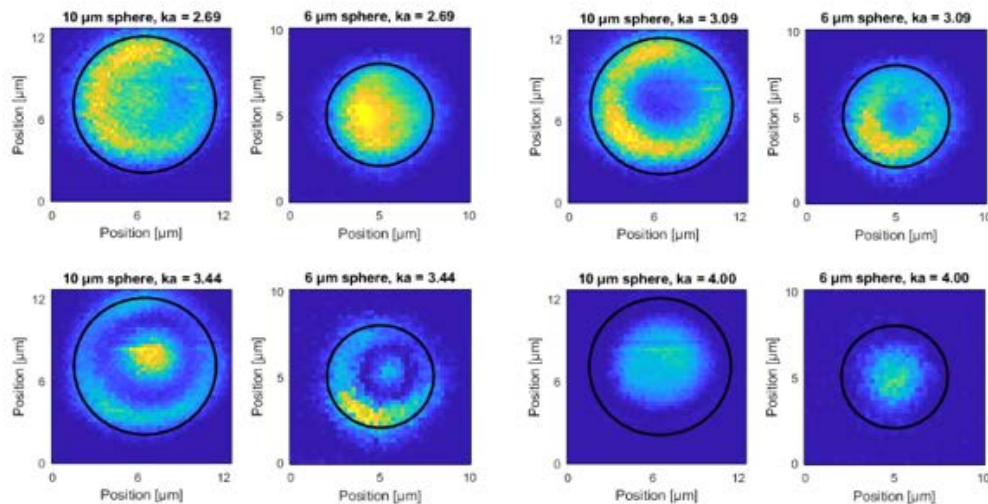
Movie A.1: Click to play movie (electronic version only). Stills from the movie are shown in the static image. *Left:* An example F-Mode animation from liquid spheres of various sizes. The spheres have radii of 4, 6, 8, and 12 μm , respectively. The animation plays as a function of increasing frequency band, as indicated at the top of the image. *Right:* The corresponding power spectra for the spheres. The black rectangle indicates the band used to generate the F-Mode image on the left. When the band captures a spectral minima for one sphere, but not for others, that sphere will darken in the corresponding F-Mode image.



Movie A.2: Click to play movie (electronic version only). Stills from the movie are shown in the static image. An F-Mode animation comprised of all individual F-Mode images from the vessel phantom data. The F-Mode images in the animation are played as a function of increasing spectral band. In each image, the vessel with the highest visibility changes due to the presence of size-dependent features in the power spectra.



Movie A.3: Click to play movie (electronic version only). Stills from the movie are shown in the static image. An F-Mode animation comprised of all individual F-Mode images from the polystyrene microsphere data. Drastic changes in the spatial patterning of the 10 μm sphere are observed as a function of spectral band. Similar variation can be seen in the 6 μm sphere, but to a lesser extent due to the scanning step size.



Movie A.4: Click to play movie (electronic version only). Stills from the movie are shown in the static image. F-Mode animations from an individual 10 μm polystyrene microsphere (Left) and a 6 μm microsphere (Right). The animations are synchronized to play as a function of ka , where k is the wavenumber and a is the sphere radius. When the animations are synchronized in this manner, it is apparent that both spheres attain similar spatial patterning at the same ka value. The black circles indicate the approximate diameter of the microsphere for reference.

Appendix B – Supplementary Information for Chapter 5

The following Figures and Movies were included as supplementary information for the manuscript that Chapter 5 is based on. (*M. J. Moore, et al., “Simultaneous Ultra-high Frequency Photoacoustic Microscopy and Photoacoustic Radiometry of Zebrafish Larvae in vivo,” (Submitted for publication, Photoacoustics, July 2018).*)

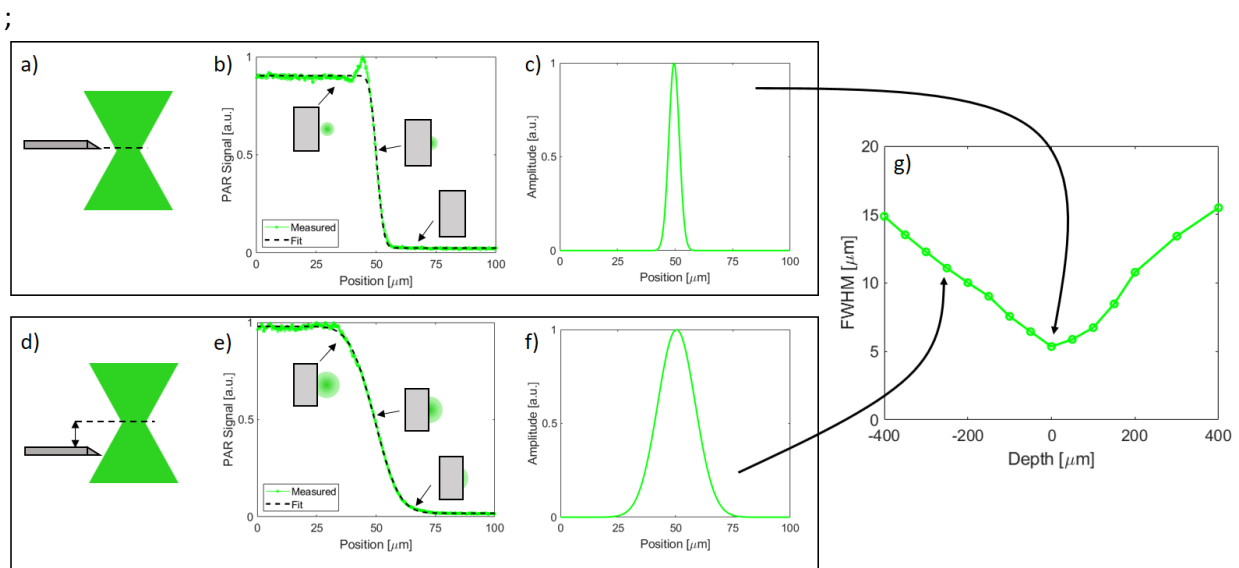


Figure B.1: Overview of the knife-edge technique for assessing the beam profile. A razor blade is translated through the focused laser beam at a specified axial depth. A schematic of the razorblade positioned at the beam waist (a) and $250\ \mu\text{m}$ below the waist (d) are shown. Axial positioning of the laser beam is achieved by translating the focusing objective. b) & e) The PAR signal as a function of razor blade position is measured and the resulting datapoints fit to an erf function. The view of the razor blade (gray rectangle) along the propagation direction of the laser beam is shown at various scan positions. c) & f) The fit curves are differentiated, and the FWHM of the resultant Gaussian is found. g) The FWHM is plotted as a function of axial position within the laser beam. The FWHM at the beam waist for this experiment was $5.3\ \mu\text{m}$.

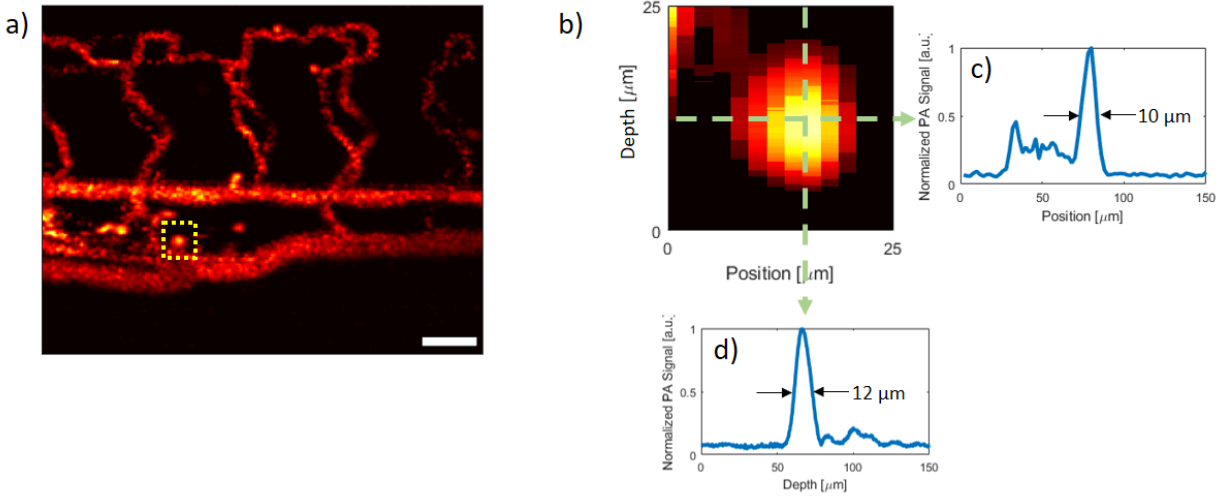


Figure B.2: a) PA MAP image from Figure 5.4b with a dashed region indicating a single RBC. b) The zoomed in B-Mode view of the same RBC in a). The lateral and axial profiles through the RBC are shown in c) and d), respectively. The scale bar in a) is 50 μm .

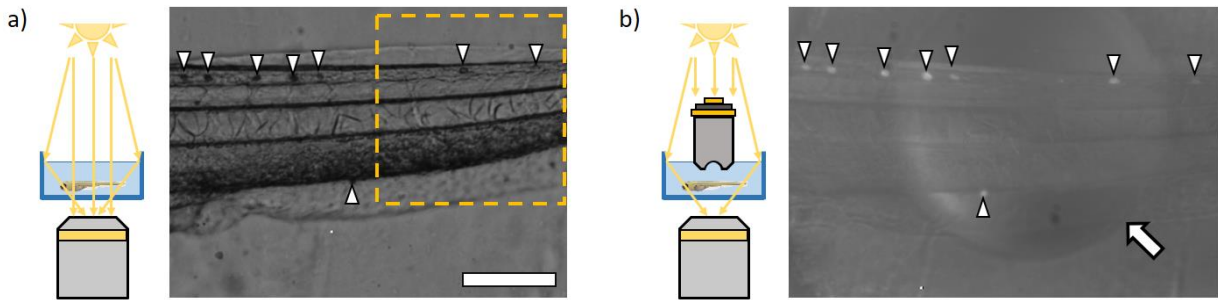
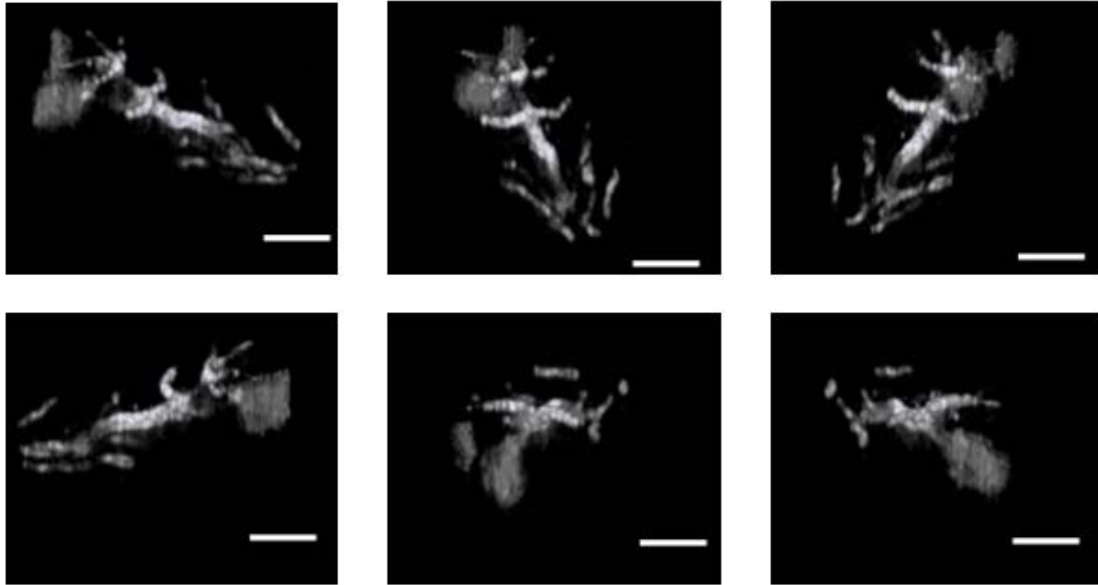
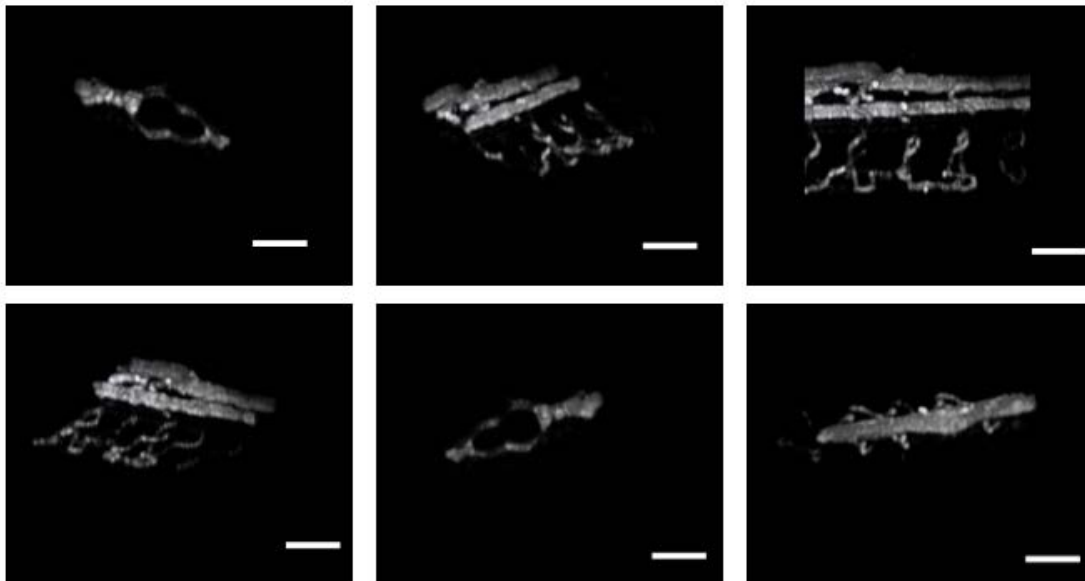


Figure B.3: a) Transmission brightfield microscopy images of a casper zebrafish without (a) and with (b) the US transducer in place between the sample & brightfield light source. With the transducer blocking the central portion of the light source, only oblique illumination occurs. This causes the scattering iridophores (arrowheads) to become highly visible. The dashed box in a) indicates the region scanned in Figure 5.5e-g). The rim of the transducer is indicated with an arrow in b). The scale bar in a) is 200 μm and can be applied to both images.



Movie B.1: Click to play movie (electronic version only). Stills from the movie are shown in the static image. 3D PA volume rendering of the vasculature depicted in Figure 5.3c. The scale bar is 100 μm .



Movie B.2: Click to play movie (electronic version only). Stills from the movie are shown in the static image. 3D PA volume rendering of the zebrafish trunk vasculature depicted in Figure 5.4b. The scale bar is 100 μm .

References

- [1] W.C. Röntgen, On a New Kind of Rays, *Science* (80-.). 3 (1896) 227–231.
- [2] A.G. Bell, On the Production and Reproduction of Sound by Light, *Am. J. Sci.* 20 (1880) 305–324.
- [3] A.G. Bell, The Production of Sound By Radiant Energy, *Science* (80-.). 2 (1881) 242–253. doi:10.1126/science.08-2.49.242.
- [4] S. Manohar, D. Razansky, Photoacoustics: a historical review, *Adv. Opt. Photonics.* 8 (2016) 586–617.
- [5] L. V. Wang, S. Hu, Photoacoustic Tomography: In Vivo Imaging from Organelles to Organs, *Science* (80-.). 335 (2012) 1458–1462. doi:10.1126/science.1216210.
- [6] P. Beard, Biomedical photoacoustic imaging, *Interface Focus.* 1 (2011) 602–631. doi:10.1098/rsfs.2011.0028.
- [7] A. Rosencwaig, Photoacoustic spectroscopy of biological materials, *Science.* 181 (1973) 657–658.
- [8] R. a Kruger, P. Liu, Y.R. Fang, C.R. Appledorn, Photoacoustic ultrasound (PAUS)--reconstruction tomography., *Med. Phys.* 22 (1995) 1605–1609. doi:10.1118/1.597429.
- [9] C.G.A. Hoelen, F.F.M. de Mul, R. Pongers, A. Dekker, Three-dimensional photoacoustic imaging of blood vessels in tissue, *Opt. Lett.* 23 (1998) 648–650.
- [10] X. Wang, X. Xie, G. Ku, L. V. Wang, G. Stoica, Noninvasive imaging of hemoglobin concentration and oxygenation in the rat brain using high-resolution photoacoustic tomography, *J. Biomed. Opt.* 11 (2006) 024015. doi:10.1117/1.2192804.
- [11] E.Z. Zhang, J.G. Laufer, R.B. Pedley, P.C. Beard, In vivo high-resolution 3D photoacoustic imaging of superficial vascular anatomy., *Phys. Med. Biol.* 54 (2009) 1035–1046. doi:10.1088/0031-9155/54/4/014.

- [12] J.M. Yang, C. Favazza, R. Chen, J. Yao, X. Cai, K. Maslov, Q. Zhou, K.K. Shung, L. V. Wang, Simultaneous functional photoacoustic and ultrasonic endoscopy of internal organs in vivo, *Nat. Med.* 18 (2012) 1297–1302. doi:10.1038/nm.2823.
- [13] B. Wang, A. Karpouk, D. Yeager, J. Amirian, S. Litovsky, R. Smalling, S. Emelianov, In vivo Intravascular Ultrasound-guided Photoacoustic Imaging of Lipid in Plaques Using an Animal Model of Atherosclerosis, *Ultrasound Med. Biol.* 38 (2012) 2098–2103. doi:10.1016/j.ultrasmedbio.2012.08.006.
- [14] L. Nie, Z. Guo, L. V. Wang, Photoacoustic tomography of monkey brain using virtual point ultrasonic transducers, *J. Biomed. Opt.* 16 (2011) 076005. doi:10.1117/1.3595842.
- [15] C. Huang, L. Nie, R.W. Schoonover, Z. Guo, C.O. Schirra, M.A. Anastasio, L. V. Wang, Aberration correction for transcranial photoacoustic tomography of primates employing adjunct image data, *J. Biomed. Opt.* 17 (2012) 066016. doi:10.1117/1.JBO.17.6.066016.
- [16] X.L. Dean-Ben, T.F. Fehm, M. Gostic, D. Razansky, Volumetric hand-held photoacoustic angiography as a tool for real-time screening of dense breast, *J. Biophotonics.* 9 (2016) 253–259. doi:10.1002/jbio.201500008.
- [17] L. Lin, P. Hu, J. Shi, C.M. Appleton, K. Maslov, L. V. Wang, Clinical photoacoustic computed tomography of the human breast in vivo with a single breath hold, *Proc SPIE.* 10494 (2018) 104942X-1. doi:10.1117/12.2290987.
- [18] S. Mallidi, G.P. Luke, S. Emelianov, Photoacoustic imaging in cancer detection, diagnosis, and treatment guidance, *Trends Biotechnol.* 29 (2011) 213–221. doi:10.1016/j.tibtech.2011.01.006.
- [19] S.A. Ermilov, T. Khampirad, A. Conjusteau, M.H. Leonard, R. Lacewell, K. Mehta, T. Miller, A.A. Oraevsky, Laser photoacoustic imaging system for detection of breast cancer, *J. Biomed. Opt.* 14 (2009) 024007. doi:10.1117/1.3086616.

- [20] A.B.E. Attia, S.Y. Chuah, D. Razansky, C.J.H. Ho, P. Malempati, U.S. Dinish, R. Bi, C.Y. Fu, S.J. Ford, J.S.S. Lee, M.W.P. Tan, M. Olivo, S.T.G. Thng, Noninvasive real-time characterization of non-melanoma skin cancers with handheld optoacoustic probes, *Photoacoustics*. 7 (2017) 20–26. doi:10.1016/j.pacs.2017.05.003.
- [21] S.Y. Chuah, A.B.E. Attia, V. Long, C.J.H. Ho, P. Malempati, C.Y. Fu, S.J. Ford, J.S.S. Lee, W.P. Tan, D. Razansky, M. Olivo, S. Thng, Structural and functional 3D mapping of skin tumours with non-invasive multispectral optoacoustic tomography, *Ski. Res. Technol.* 23 (2017) 221–226. doi:10.1111/srt.12326.
- [22] J. Aguirre, M. Schwarz, N. Garzorz, M. Omar, A. Buehler, K. Eyerich, V. Ntziachristos, Precision assessment of label-free psoriasis biomarkers with ultra-broadband optoacoustic mesoscopy, *Nat. Biomed. Eng.* 1 (2017) 1–8. doi:10.1038/s41551-017-0068.
- [23] R.G.M. Kolkman, M.J. Mulder, C.P. Glade, W. Steenbergen, T.G. van Leeuwen, Photoacoustic imaging of port-wine stains, *Lasers Surg. Med.* 40 (2008) 178–182. doi:10.1002/lsm.20612.
- [24] K. Jansen, A.F.W. van der Steen, H.M.M. van Beusekom, J.W. Oosterhuis, G. van Soest, Intravascular photoacoustic imaging of human coronary atherosclerosis, *Opt. Lett.* 36 (2011) 597–599. doi:10.1364/OL.36.000597.
- [25] J. Xia, J. Yao, L. V Wang, *Photoacoustic Tomography : Principles and Advances*, *Prog. Eletromagnic Res.* 147 (2014) 1–22.
- [26] R.A. Kruger, R.B. Lam, D.R. Reinecke, S.P. Del Rio, R.P. Doyle, Photoacoustic angiography of the breast, *Med. Phys.* 37 (2010) 6096–6100. doi:10.1118/1.3497677.
- [27] S. Manohar, S.E. Vaartjes, J.C.G. van Hespén, J.M. Klaase, F.M. van den Engh, W. Steenbergen, T.G. van Leeuwen, Initial results of in vivo non-invasive cancer imaging in the human breast using near-infrared photoacoustics, *Opt. Express*. 15 (2007) 12277. doi:10.1364/OE.15.012277.

- [28] Y. Zhou, D. Wang, Y. Zhang, U. Chitgupi, J. Geng, Y. Wang, Y. Zhang, T.R. Cook, J. Xia, J.F. Lovell, A phosphorus phthalocyanine formulation with intense absorbance at 1000 nm for deep optical imaging, *Theranostics*. 6 (2016) 688–697. doi:10.7150/thno.14555.
- [29] G.P. Luke, D. Yeager, S.Y. Emelianov, Biomedical applications of photoacoustic imaging with exogenous contrast agents, *Ann. Biomed. Eng.* 40 (2012) 422–437. doi:10.1007/s10439-011-0449-4.
- [30] V. Ntziachristos, Going deeper than microscopy: the optical imaging frontier in biology., *Nat. Methods*. 7 (2010) 603–614. doi:10.1038/nmeth.1483.
- [31] E.M. Strohm, M.J. Moore, M.C. Kolios, Single Cell Photoacoustic Microscopy: A Review, *IEEE J. Sel. Top. Quantum Electron.* 22 (2016). doi:10.1109/JSTQE.2015.2497323.
- [32] G.S. Kino, *Acoustic Waves: Devices, Imaging, and Analog Signal Processing*, Prentice Hall PTR, 1987.
- [33] J. Yao, L. V. Wang, Photoacoustic microscopy, *Laser Photon. Rev.* 7 (2013) 758–778. doi:10.1002/lpor.201200060.
- [34] E.M. Strohm, M.J. Moore, M.C. Kolios, High resolution ultrasound and photoacoustic imaging of single cells, *Photoacoustics*. 4 (2016) 36–42. doi:10.1016/j.pacs.2016.01.001.
- [35] L. V Wang, L. Gao, *Photoacoustic Microscopy and Computed Tomography: From Bench to Bedside.*, 2013. doi:10.1146/annurev-bioeng-071813-104553.
- [36] H.F. Zhang, K. Maslov, G. Stoica, L. V Wang, Functional photoacoustic microscopy for high-resolution and noninvasive in vivo imaging., *Nat. Biotechnol.* 24 (2006) 848–851. doi:10.1038/nbt1220.
- [37] J. Yao, L. Wang, J.-M. Yang, K.I. Maslov, T.T.W. Wong, L. Li, C.-H. Huang, J. Zou, L. V Wang, High-speed label-free functional photoacoustic microscopy of mouse

- brain in action, *Nat. Methods*. 12 (2015) 407–410. doi:10.1038/nmeth.3336.
- [38] J. Yao, K.I. Maslov, Y. Zhang, Y. Xia, L. V. Wang, Label-free oxygen-metabolic photoacoustic microscopy in vivo, *J. Biomed. Opt.* 16 (2011) 076003. doi:10.1117/1.3594786.
- [39] S. Hu, K. Maslov, L. V Wang, Second-generation optical-resolution photoacoustic microscopy with improved sensitivity and speed., *Opt. Lett.* 36 (2011) 1134–1136. doi:10.1364/OL.36.001134.
- [40] P. Hajireza, A. Forbrich, R. Zemp, In-vivo functional optical-resolution photoacoustic microscopy with stimulated Raman scattering fiber-laser source, *Biomed. Opt. Express*. 5 (2014) 539–546. doi:10.1364/BOE.5.000539.
- [41] K. Maslov, H.F. Zhang, S. Hu, L. V Wang, Optical-resolution photoacoustic microscopy for in vivo imaging of single capillaries., *Opt. Lett.* 33 (2008) 929–931. doi:10.1364/OL.33.000929.
- [42] C. Zhang, K. Maslov, L. V Wang, Subwavelength-resolution label-free photoacoustic microscopy of optical absorption in vivo., *Opt. Lett.* 35 (2010) 3195–3197. doi:10.1364/OL.35.003195.
- [43] Y. Wang, K. Maslov, Y. Zhang, S. Hu, L. Yang, Y. Xia, J. Liu, L. V Wang, Fiber-laser-based photoacoustic microscopy and melanoma cell detection., *J. Biomed. Opt.* 16 (2011) 011014. doi:10.1117/1.3525643.
- [44] E.M. Strohm, E.S.L. Berndt, M.C. Kolios, High frequency label-free photoacoustic microscopy of single cells, *Photoacoustics*. 1 (2013) 49–53. doi:10.1016/j.pacs.2013.08.003.
- [45] C. Zhang, Y.S. Zhang, D.-K. Yao, Y. Xia, L. V Wang, Label-free photoacoustic microscopy of cytochromes., *J. Biomed. Opt.* 18 (2013) 20504. doi:10.1117/1.JBO.18.2.020504.
- [46] A. Danielli, K. Maslov, A. Garcia-Uribe, A.M. Winkler, C. Li, L. Wang, Y. Chen,

- G.W. Dorn, L. V Wang, Label-free photoacoustic nanoscopy., *J. Biomed. Opt.* 19 (2014) 86006. doi:10.1117/1.JBO.19.8.086006.
- [47] M.J. Moore, P.M. Schygulla, E.M. Strohm, M.C. Kolios, Single red blood cell oxygenation saturation imaging with multispectral photoacoustic microscopy, in: *Proc. IEEE Int. Ultrason. Symp.*, 2016. doi:10.1109/ULTSYM.2016.7728869.
- [48] B. Dong, H. Li, Z. Zhang, K. Zhang, S. Chen, C. Sun, H.F. Zhang, Isometric multimodal photoacoustic microscopy based on optically transparent micro-ring ultrasonic detection, *Optica*. 2 (2015) 169. doi:10.1364/OPTICA.2.000169.
- [49] L. Wang, K. Maslov, L. V. Wang, Single-cell label-free photoacoustic flowoxigraphy in vivo, *Proc. Natl. Acad. Sci.* 110 (2013) 5759–5764. doi:10.1073/pnas.1215578110.
- [50] D.-K. Yao, K. Maslov, K.K. Shung, Q. Zhou, L. V Wang, In vivo label-free photoacoustic microscopy of cell nuclei by excitation of DNA and RNA., *Opt. Lett.* 35 (2010) 4139–4141. doi:10.1364/OL.35.004139.
- [51] D. Yao, R. Chen, K. Maslov, Q. Zhou, L. V Wang, Optimal ultraviolet wavelength for in vivo photoacoustic imaging of cell nuclei, *J. Biomed. Opt.* 17 (2012) 056004–7. doi:10.1117/1.JBO.17.5.056004.
- [52] T.T.W. Wong, R. Zhang, C. Zhang, H.C. Hsu, K.I. Maslov, L. Wang, J. Shi, R. Chen, K.K. Shung, Q. Zhou, L. V. Wang, Label-free automated three-dimensional imaging of whole organs by microtomy-assisted photoacoustic microscopy, *Nat. Commun.* 8 (2017) 1–8. doi:10.1038/s41467-017-01649-3.
- [53] Y.S. Zhang, J. Yao, C. Zhang, L. Li, L. V. Wang, Y. Xia, Optical-resolution photoacoustic microscopy for volumetric and spectral analysis of histological and immunochemical samples, *Angew. Chemie - Int. Ed.* 53 (2014) 8099–8103. doi:10.1002/anie.201403812.
- [54] L. Gao, C. Zhang, C. Li, L. V. Wang, Intracellular temperature mapping with fluorescence-assisted photoacoustic-thermometry, *Appl. Phys. Lett.* 102 (2013) 1–5.

doi:10.1063/1.4807140.

- [55] J. Yao, K. Maslov, S. Hu, L. V. Wang, Evans blue dye-enhanced capillary-resolution photoacoustic microscopy in vivo, *J. Biomed. Opt.* 14 (2009) 054049. doi:10.1117/1.3251044.
- [56] Y.S. Zhang, Y. Wang, L. Wang, Y. Wang, X. Cai, C. Zhang, L. V. Wang, Y. Xia, Labeling human mesenchymal stem cells with gold nanocages for in vitro and in vivo tracking by two-photon microscopy and photoacoustic microscopy, *Theranostics*. 3 (2013) 532–543. doi:10.7150/thno.5369.
- [57] J.R. Cook, W. Frey, S. Emelianov, Quantitative photoacoustic imaging of nanoparticles in cells and tissues, *ACS Nano*. 7 (2013) 1272–1280. doi:10.1021/nn304739s.
- [58] S. Yang, F. Ye, D. Xing, Intracellular label-free gold nanorods imaging with photoacoustic microscopy, *Opt. Express*. 20 (2012) 10370. doi:10.1364/OE.20.010370.
- [59] M.-L. Li, J.C. Wang, J.A. Schwartz, K.L. Gill-Sharp, G. Stoica, L. V. Wang, In-vivo photoacoustic microscopy of nanoshell extravasation from solid tumor vasculature, *J. Biomed. Opt.* 14 (2009) 010507. doi:10.1117/1.3081556.
- [60] W. Song, W. Zheng, R. Liu, R. Lin, H. Huang, X. Gong, S. Yang, R. Zhang, L. Song, Reflection-mode in vivo photoacoustic microscopy with subwavelength lateral resolution., *Biomed. Opt. Express*. 5 (2014) 4235–4241. doi:10.1364/BOE.5.004235.
- [61] A. Briggs, *Acoustic Microscopy*, Oxford University Press, New York, 1992.
- [62] K. Maslov, G. Stoica, L. V Wang, In vivo dark-field reflection-mode photoacoustic microscopy., *Opt. Lett.* 30 (2005) 625–627. doi:10.1364/OL.30.000625.
- [63] J. Yao, L. V. Wang, Sensitivity of photoacoustic microscopy, *Photoacoustics*. 2 (2014) 87–101. doi:10.1016/j.pacs.2014.04.002.
- [64] C. Zhang, K. Maslov, J. Yao, L. V. Wang, In vivo photoacoustic microscopy with 7.6- μm axial resolution using a commercial 125-MHz ultrasonic transducer, *J. Biomed.*

- Opt. 17 (2012) 116016. doi:10.1117/1.
- [65] E.W. Stein, K. Maslov, L. V. Wang, Noninvasive, in vivo imaging of the mouse brain using photoacoustic microscopy, *J. Appl. Phys.* 105 (2009) 1020271–5. doi:10.1063/1.3116134.
- [66] M. Omar, J. Rebling, K. Wicker, T. Schmitt-Manderbach, M. Schwarz, J. Gateau, H. López-Schier, T. Mappes, V. Ntziachristos, Optical imaging of post-embryonic zebrafish using multi orientation raster scan optoacoustic mesoscopy, *Light Sci. Appl.* 6 (2017) 1–6. doi:10.1038/lssa.2016.186.
- [67] M. Omar, D. Soliman, J. Gateau, V. Ntziachristos, Ultrawideband reflection-mode optoacoustic mesoscopy., *Opt. Lett.* 39 (2014) 3911–4. doi:10.1364/OL.39.003911.
- [68] M. Schwarz, A. Buehler, J. Aguirre, V. Ntziachristos, Three-dimensional multispectral optoacoustic mesoscopy reveals melanin and blood oxygenation in human skin in vivo, *J. Biophotonics.* 9 (2016) 55–60. doi:10.1002/jbio.201500247.
- [69] M. Omar, M. Schwarz, D. Soliman, P. Symvoulidis, V. Ntziachristos, Pushing the Optical Imaging Limits of Cancer with Multi-Frequency-Band Raster-Scan Optoacoustic Mesoscopy (RSOM), *Neoplasia.* 17 (2015) 208–214. doi:10.1016/j.neo.2014.12.010.
- [70] G. Paltauf, P.E. Dyer, Photomechanical processes and effects in ablation, *Chem. Rev.* 103 (2003) 487–518. doi:10.1021/cr010436c.
- [71] E. Hysi, E.M. Strohm, M.C. Kolios, Probing Different Biological Length Scales Using Photoacoustics: From 1 To 1000 MHz, in: A.H.-P. Ho, D. Kim, M.G. Somekh (Eds.), *Handb. Photonics Biomed. Eng.*, Springer Netherlands, 2014: pp. 1–18.
- [72] J.W. Valvano, J.R. Cochran, K.R. Diller, Thermal conductivity and diffusivity of biomaterials measured with self-heated thermistors, *Int. J. Thermophys.* 6 (1985) 301–311. doi:10.1007/BF00522151.
- [73] F.A. Duck, *Physical Properties of Tissue: A Comprehensive Reference Book*,

Academic Press Inc., 1990.

- [74] E. V. Petrova, A.A. Oraevsky, S.A. Ermilov, Red blood cell as a universal optoacoustic sensor for non-invasive temperature monitoring, *Appl. Phys. Lett.* 105 (2014). doi:10.1063/1.4894635.
- [75] Y.S. Chen, W. Frey, S. Aglyamov, S. Emelianov, Environment-dependent generation of photoacoustic waves from plasmonic nanoparticles, *Small.* 8 (2012) 47–52. doi:10.1002/smll.201101140.
- [76] P. Westervelt, R. Larson, Laser-excited broadside array, *J. Acoust. Soc. Am.* 54 (1973) 121–122. doi:10.1121/1.1913551.
- [77] G.J. Diebold, M.I. Khan, S.M. Park, Photoacoustic “signatures” of particulate matter: optical production of acoustic monopole radiation., *Science.* 250 (1990) 101–104. doi:10.1126/science.250.4977.101.
- [78] E.M. Strohm, I. Gorelikov, N. Matsuura, M.C. Kolios, Acoustic and photoacoustic characterization of micron-sized perfluorocarbon emulsions, *J. Biomed. Opt.* 17 (2012) 096016. doi:10.1117/1.JBO.17.9.096016.
- [79] G.J. Diebold, T. Sun, M.I. Khan, Photoacoustic monopole radiation in one, two, and three dimensions, *Phys. Rev. Lett.* 67 (1991) 3384–3387. doi:10.1103/PhysRevLett.67.3384.
- [80] M.I. Khan, T. Sun, G.J. Diebold, Photoacoustic waves generated by absorption of laser radiation in optically thin cylinders, *J. Acoust. Soc. Am.* 94 (1993) 931–940. doi:10.1121/1.408195.
- [81] M.I. Khan, G.J. Diebold, The photoacoustic effect generated by an isotropic solid sphere, *Ultrasonics.* 33 (1995) 265–269.
- [82] G.J. Diebold, P.J. Westervelt, The photoacoustic effect generated by a spherical droplet in a fluid, *J. Acoust. Soc. Am.* 84 (1988) 2245–2251.
- [83] Y. Li, H. Fang, C. Min, X. Yuan, Analytic theory of photoacoustic wave generation

- from a spheroidal droplet, *Opt. Express*. 22 (2014) 19953. doi:10.1364/OE.22.019953.
- [84] Y. Li, H. Fang, C. Min, X. Yuan, Simulating photoacoustic waves produced by individual biological particles with spheroidal wave functions, *Sci. Rep.* 5 (2015) 14801. doi:10.1038/srep14801.
- [85] E.M. Strohm, E.S.L. Berndl, M.C. Kolios, Probing Red Blood Cell Morphology Using High-Frequency Photoacoustics, *Biophys. J.* 105 (2013) 59–67. doi:10.1016/j.bpj.2013.05.037.
- [86] E.M. Strohm, L.A. Wirtzfeld, G.J. Czarnota, M.C. Kolios, High frequency ultrasound imaging and simulations of sea urchin oocytes, *J. Acoust. Soc. Am.* 142 (2017) 268–275. doi:10.1121/1.4993594.
- [87] E.M. Strohm, M.C. Kolios, Classification of blood cells and tumor cells using label-free ultrasound and photoacoustics, *Cytom. Part A*. 87A (2015) 741–749. doi:10.1002/cyto.a.22698.
- [88] M.J. Moore, E.M. Strohm, M.C. Kolios, Assessment of the Nucleus-to-Cytoplasmic Ratio in MCF-7 Cells Using Ultra-high Frequency Ultrasound and Photoacoustics, *Int. J. Thermophys.* 37 (2016). doi:10.1007/s10765-016-2129-y.
- [89] M.J. Moore, E.M. Strohm, M.C. Kolios, Evaluation of the morphological parameters of cancer cells using high-frequency ultrasound and photoacoustics, in: 2015 IEEE Int. Ultrason. Symp., 2015: pp. 1–4. doi:10.1109/ULTSYM.2015.0246.
- [90] B. Stewart, C. Wild, *World Cancer Report 2014*, International Agency for Research on Cancer, 2014.
- [91] C. Fletcher, *Diagnostic Histopathology of Tumors*, 4ed., Saunders/Elsevier, 2013.
- [92] J.A. Swanson, M. Lee, P.E. Knapp, Cellular dimensions affecting the nucleocytoplasmic volume ratio, *J. Cell Biol.* 115 (1991) 941–948. doi:10.1083/jcb.115.4.941.
- [93] M.J. Doughty, Reliability of nucleus-to-cell and nucleus-to-cytoplasm calculations

- for conjunctival impression cytology specimens., *Curr. Eye Res.* 37 (2012) 583–91. doi:10.3109/02713683.2012.655397.
- [94] E. Cosatto, M. Miller, H.P. Graf, J.S. Meyer, Grading nuclear pleomorphism on histological micrographs, 2008 19th Int. Conf. Pattern Recognit. (2008) 8–11.
- [95] S. Petushi, F.U. Garcia, M.M. Haber, C. Katsinis, A. Tozeren, Large-scale computations on histology images reveal grade-differentiating parameters for breast cancer, *BMC Med. Imaging.* 6 (2006) 1–11. doi:10.1186/1471-2342-6-14.
- [96] P. Balasubramanian, L. Yang, Confocal images of circulating tumor cells obtained using a methodology and technology that removes normal cells, *Mol. Pharm.* 6 (2009) 1402–1408.
- [97] V. Nandakumar, L. Kelbauskas, K.F. Hernandez, K.M. Lintecum, P. Senechal, K.J. Bussey, P.C.W. Davies, R.H. Johnson, D.R. Meldrum, Isotropic 3D nuclear morphometry of normal, fibrocystic and malignant breast epithelial cells reveals new structural alterations, *PLoS One.* 7 (2012). doi:10.1371/journal.pone.0029230.
- [98] V. Nandakumar, L. Kelbauskas, R. Johnson, D. Meldrum, Quantitative characterization of preneoplastic progression using single-cell computed tomography and three-dimensional karyometry., *Cytom. Part A.* 79 A (2011) 25–34. doi:10.1002/cyto.a.20997.
- [99] T.C. George, D. a. Basiji, B.E. Hall, D.H. Lynch, W.E. Ortyn, D.J. Perry, M.J. Seo, C. a. Zimmerman, P.J. Morrissey, Distinguishing modes of cell death using the ImageStream® multispectral imaging flow cytometer, *Cytom. Part A.* 59A (2004) 237–245. doi:10.1002/cyto.a.20048.
- [100] T.C. George, S.L. Fanning, P. Fitzgerald-Bocarsly, R.B. Medeiros, S. Highfill, Y. Shimizu, B.E. Hall, K. Frost, D. Basiji, W.E. Ortyn, P.J. Morrissey, D.H. Lynch, Quantitative measurement of nuclear translocation events using similarity analysis of multispectral cellular images obtained in flow, *J. Immunol. Methods.* 311 (2006) 117–129. doi:10.1016/j.jim.2006.01.018.

- [101] D. a. Basiji, W.E. Ortyn, L. Liang, V. Venkatachalam, P. Morrissey, Cellular Image Analysis and Imaging by Flow Cytometry, *Clin. Lab. Med.* 27 (2007) 653–670. doi:10.1016/j.cll.2007.05.008.
- [102] V.P. Zharov, E.I. Galanzha, V. V Tuchin, Photothermal image flow cytometry in vivo, 30 (2005) 628–630.
- [103] V.P. Zharov, E.I. Galanzha, V. V Tuchin, Integrated photothermal flow cytometry in vivo, *J. Biomed. Opt.* 10 (2005) 0515021-13. doi:10.1117/1.2070167.
- [104] V.P. Zharov, E.I. Galanzha, V. V. Tuchin, In vivo photothermal flow cytometry: Imaging and detection of individual cells in blood and lymph flow, *J. Cell. Biochem.* 97 (2006) 916–932. doi:10.1002/jcb.20766.
- [105] E.I. Galanzha, E. V. Shashkov, P.M. Spring, J.Y. Suen, V.P. Zharov, In vivo, noninvasive, label-free detection and eradication of circulating metastatic melanoma cells using two-color photoacoustic flow cytometry with a diode laser, *Cancer Res.* 69 (2009) 7926–7934. doi:10.1158/0008-5472.CAN-08-4900.
- [106] E.I. Galanzha, E. V Shashkov, T. Kelly, J. Kim, L. Yang, V.P. Zharov, In vivo magnetic enrichment and multiplex photoacoustic detection of circulating tumour cells, *Nat. Nanotechnol.* 4 (2009) 855–860. doi:10.1038/nnano.2009.333.
- [107] E. Galanzha, V. Zharov, Circulating Tumor Cell Detection and Capture by Photoacoustic Flow Cytometry in Vivo and ex Vivo, *Cancers (Basel)*. 5 (2013) 1691–1738. doi:10.3390/cancers5041691.
- [108] D.A. Nedosekin, M.A. Juratli, M. Sarimollaoglu, C.L. Moore, N.J. Rusch, M.S. Smeltzer, V.P. Zharov, E.I. Galanzha, Photoacoustic and photothermal detection of circulating tumor cells , bacteria and nanoparticles in cerebrospinal fluid in vivo and ex vivo, 533 (2013) 523–533. doi:10.1002/jbio.201200242.
- [109] Strohm E.M., M.C. Kolios, Circulating tumor cell detection using high frequency ultrasound and photoacoustics, *Cytom. Part A.* (n.d.).

- [110] E.M. Strohm, E.S.L. Berndl, M.C. Kolios, Probing red blood cell morphology using high frequency photoacoustics, *Biophys. J.* 105 (2013) 59–67.
- [111] E. Moeendarbary, L. Valon, M. Fritzsche, A.R. Harris, D. a Moulding, A.J. Thrasher, E. Stride, L. Mahadevan, G.T. Charras, The cytoplasm of living cells behaves as a poroelastic material., *Nat. Mater.* 12 (2013) 253–261. doi:10.1038/nmat3517.
- [112] V.C. Anderson, Sound scattering from a fluid sphere, *J. Acoust. Soc. Am.* 22 (1950) 426–431. doi:10.1121/1.381326.
- [113] H.G. Frey, R.R. Goodman, Acoustic Scattering from Fluid Spheres, *J. Acoust. Soc. Am.* 40 (1966) 417–420. doi:10.1121/1.1937298.
- [114] L. V Wang, Tutorial on photoacoustic microscopy and computed tomography, *IEEE J. Sel. Top. Quantum Electron.* 14 (2008) 171–179. doi:10.1109/JSTQE.2007.913398.
- [115] A. Siegman, *Lasers*, University Science Books, California, 1986.
- [116] M.C. Kolios, E.M. Strohm, G.J. Czarnota, Acoustic Microscopy of Single Cells, in: J. Mamou, M. Oelze (Eds.), *Quant. Ultrasound Soft Tissues*, Springer, 2013: pp. 315–341.
- [117] M.M. Pasternak, E.M. Strohm, E.S.L. Berndl, M.C. Kolios, Properties of cells through life and death - an acoustic microscopy investigation, *Cell Cycle.* 14 (2015) 2891–2898. doi:10.1080/15384101.2015.1069925.
- [118] H. Reile, G. Bernhardt, M. Koch, H. Schonenberger, M. Hollstein, F. Lux, Chemosensitivity of human MCF-7 breast cancer cells to diastereoisomeric diaqua(1,2-diphenylethylenediamine) platinum(II) sulfates and specific platinum accumulation, *Cancer Chemother. Pharmacol.* 30 (1992) 113–122. doi:10.1007/BF00686402.
- [119] S.K. Arya, K.C. Lee, D. Bin Dah’alan, Daniel, A.R.A. Rahman, Breast tumor cell detection at single cell resolution using an electrochemical impedance technique,

- Lab Chip. 12 (2012) 2362. doi:10.1039/c2lc21174b.
- [120] D.L. Adams, P. Zhu, O. V. Makarova, S.S. Martin, M. Charpentier, S. Chumsri, S. Li, P. Amstutz, C.-M. Tang, The systematic study of circulating tumor cell isolation using lithographic microfilters, RSC Adv. 4 (2014) 4334–4342. doi:10.1039/C3RA46839A.
- [121] J. Dahle, E. Kalanxhi, N. Tisnek, Dosimetry of a ^{238}Pu -based α -particle irradiator and its biological application in a study of the bystander effect, Anticancer Res. 31 (2011) 2113–2120.
- [122] I. Haque, S. Banerjee, A. De, G. Maity, S. Sarkar, M. Majumdar, S.S. Jha, D. McGrigor, S.K. Banerjee, CCN5/WISP-2 promotes growth arrest of triple-negative breast cancer cells through accumulation and trafficking of p27Kip1 via Skp2 and FOXO3a regulation, Oncogene. 34 (2015) 3152–3163. doi:10.1038/onc.2014.250.
- [123] B. Alberts, A. Johnson, J. Lewis, D. Morgan, M. Raff, K. Roberts, P. Walter, Molecular Biology of the Cell, Garland Science, 2014. doi:10.1093/acprof.
- [124] E.M. Strohm, V. Gnyawali, M. Van De Vondervoort, Y. Daghighi, S.S.H. Tsai, M.C. Kolios, Classification of biological cells using a sound wave based flow cytometer, in: Proc SPIE, 2016: p. 97081A1-6. doi:10.1117/12.2211740.
- [125] A. Rosencwaig, Photoacoustic spectroscopy of solids, Opt. Commun. 7 (1973) 305–308. doi:10.1063/1.3069155.
- [126] A.C. Tam, Applications of photoacoustic sensing techniques, Rev. Mod. Phys. 58 (1986) 381–431. doi:10.1103/RevModPhys.58.381.
- [127] L. V. Wang, Multiscale photoacoustic microscopy and computed tomography, Nat. Photonics. 3 (2009) 503–509. doi:10.1109/JSTQE.2007.913398.
- [128] M. Xu, L. V. Wang, Photoacoustic imaging in biomedicine, Rev. Sci. Instrum. 77 (2006) 041101. doi:10.1063/1.2195024.
- [129] C. Zhang, Y.S. Zhang, D.-K. Yao, Y. Xia, L. V Wang, Label-free photoacoustic

- microscopy of cytochromes., *J. Biomed. Opt.* 18 (2013) 20504.
doi:10.1117/1.JBO.18.2.020504.
- [130] L. Li, L. Zhu, Y. Shen, L. V. Wang, Multiview Hilbert transformation in full-ring transducer array-based photoacoustic computed tomography, *J. Biomed. Opt.* 22 (2017) 076017. doi:10.1117/1.JBO.22.7.076017.
- [131] H.-P. Brecht, R. Su, M. Fronheiser, S.A. Ermilov, A. Conjusteau, A.A. Oraevsky, Whole-body three-dimensional photoacoustic tomography system for small animals., *J. Biomed. Opt.* 14 (2009) 064007. doi:10.1117/1.3259361.
- [132] A. Needles, A. Heinmiller, J. Sun, C. Theodoropoulos, D. Bates, D. Hirson, M. Yin, F.S. Foster, Development and initial application of a fully integrated photoacoustic micro-ultrasound system, *IEEE Trans. Ultrason. Ferroelectr. Freq. Control.* 60 (2013) 888–897. doi:10.1109/TUFFC.2013.2646.
- [133] H. Fang, L. V. Wang, M-mode photoacoustic particle flow imaging., *Opt. Lett.* 34 (2009) 671–673. doi:10.1364/OL.34.000671.
- [134] L. Zhu, L. Li, L. Gao, L. V. Wang, Multiview optical resolution photoacoustic microscopy, *Optica.* 1 (2014) 217–222. doi:10.1364/OPTICA.1.000217.
- [135] L. Wang, H. Wu, *Biomedical Optics: Principles and Imaging*, John Wiley & Sons, 2007.
- [136] M.I. Khan, G.J. Diebold, The photoacoustic effect generated by laser irradiation of an isotropic solid cylinder, *Ultrasonics.* 34 (1996) 19–24. doi:10.1016/0041-624X(95)00128-P.
- [137] E. Hysi, L. a. Wirtzfeld, J.P. May, E. Undzys, S.D. Li, M.C. Kolios, Photoacoustic signal characterization of cancer treatment response: Correlation with changes in tumor oxygenation, *Photoacoustics.* 5 (2017) 25–35. doi:10.1016/j.pacs.2017.03.003.
- [138] E. Hysi, R.K. Saha, M.C. Kolios, Photoacoustic ultrasound spectroscopy for assessing red blood cell aggregation and oxygenation, *J. Biomed. Opt.* 17 (2012)

- 1250061–10. doi:10.1109/ULTSYM.2012.0349.
- [139] S. Tismer, S. Brand, S. Klengel, M. Petzold, P. Czurratis, Acoustic imaging of bump defects in flip-chip devices using split spectrum analysis, *IEEE Int. Ultrason. Symp. IUS.* (2013) 950–953. doi:10.1109/ULTSYM.2013.0244.
- [140] A.M. Heagerty, C. Aalkjaer, S.J. Bund, N. Korsgaard, M.J. Mulvany, Small artery structure in hypertension. Dual processes of remodeling and growth, *Hypertension.* 21 (1993) 391–397. doi:10.1161/01.HYP.21.4.391.
- [141] D. Rizzoni, E. Porteri, G.E.M. Boari, C. De Ciuceis, I. Sleiman, M.L. Muiesan, M. Castellano, M. Miclini, E. Agabiti-Rosei, Prognostic Significance of Small-Artery Structure in Hypertension, *Circulation.* 108 (2003) 2230–2235. doi:10.1161/01.CIR.0000095031.51492.C5.
- [142] M.J. Mulvany, Small artery remodelling in hypertension, *Basic Clin. Pharmacol. Toxicol.* 110 (2012) 49–55. doi:10.1111/j.1742-7843.2011.00758.x.
- [143] Y. Xu, L. V Wang, G. Ambartsoumian, P. Kuchment, Reconstructions in limited-view thermoacoustic tomography, *Med. Phys.* 31 (2004) 724–733. doi:10.1118/1.1644531.
- [144] R.G.M. Kolkman, W. Steenbergen, T.G. van Leeuwen, In vivo photoacoustic imaging of blood vessels with a pulsed laser diode, *Lasers Med. Sci.* 21 (2006) 134–9. doi:10.1007/s10103-006-0384-z.
- [145] S. Preisser, N.L. Bush, A.G. Gertsch-Grover, S. Peeters, A.E. Bailey, J.C. Bamber, M. Frenz, M. Jaeger, Vessel orientation-dependent sensitivity of optoacoustic imaging using a linear array transducer, *J. Biomed. Opt.* 18 (2013) 26011. doi:10.1117/1.JBO.18.2.026011.
- [146] M. Xu, L. V. Wang, Analytic explanation of spatial resolution related to bandwidth and detector aperture size in thermoacoustic or photoacoustic reconstruction, *Phys. Rev. E.* 67 (2003) 0566051-15. doi:10.1103/PhysRevE.67.056605.

- [147] R.K. Jain, Normalization of Tumor Vasculature: An Emerging Concept in Antiangiogenic Therapy, *Science* (80-.). 307 (2005) 58–62. doi:10.1126/science.1104819.
- [148] O. Falou, A. Jafari Sojahrood, J.C. Kumaradas, M.C. Kolios, Surface modes and acoustic scattering of microspheres and ultrasound contrast agents, *J. Acoust. Soc. Am.* 132 (2012) 1820–9. doi:10.1121/1.4740505.
- [149] R.E. Baddour, M.D. Sherar, J.W. Hunt, G.J. Czarnota, M.C. Kolios, High-frequency ultrasound scattering from microspheres and single cells., *J. Acoust. Soc. Am.* 117 (2005) 934–943. doi:10.1121/1.1830668.
- [150] S.C. Kim, D.W. Kim, Y.H. Shim, J.S. Bang, H.S. Oh, S.W. Kim, M.H. Seo, In vivo evaluation of polymeric micellar paclitaxel formulation: Toxicity and efficacy, *J. Control. Release.* 72 (2001) 191–202. doi:10.1016/S0168-3659(01)00275-9.
- [151] V. Pattanayak, S. Lin, J.P. Guilinger, E. Ma, J.A. Doudna, D.R. Liu, High-throughput profiling of off-target DNA cleavage reveals RNA-programmed Cas9 nuclease specificity, *Nat. Biotechnol.* 31 (2013) 839–843. doi:10.1038/nbt.2673.
- [152] Y. Wang, E.M. Strohm, Y. Sun, Z. Wang, Y. Zheng, Z. Wang, M.C. Kolios, Biodegradable polymeric nanoparticles containing gold nanoparticles and Paclitaxel for cancer imaging and drug delivery using photoacoustic methods, *Biomed. Opt. Express.* 7 (2016) 4125–38. doi:10.1364/BOE.7.004125.
- [153] J. Bereiter-Hahn, I. Karl, H. Lüers, M. Vöth, Mechanical basis of cell shape: investigations with the scanning acoustic microscope, *Biochem. Cell Biol.* 73 (1995) 337–348. doi:10.1139/095-042.
- [154] J. Bereiter-Hahn, Probing Biological Cells and Tissues with Acoustic Microscopy, in: A. Briggs (Ed.), *Adv. Acoust. Microsc.* Vol. 1., Plenum Press, New York, 1995: pp. 79–110.
- [155] D.J. Stephens, *Light Microscopy Techniques for Live Cell Imaging*, *Science* (80-.).

- 300 (2003) 82–86. doi:10.1126/science.1082160.
- [156] C. Kallepitis, M.S. Bergholt, M.M. Mazo, V. Leonardo, S.C. Skaalure, S. a. Maynard, M.M. Stevens, Quantitative volumetric Raman imaging of three dimensional cell cultures, *Nat. Commun.* 8 (2017) 14843. doi:10.1038/ncomms14843.
- [157] T. Caspersson, Chapter IV: Cytochemical Analysis of the Tumour Tissue, *Acta Radiol.* 23 (1942) 32–75. doi:10.3109/00016924209175733.
- [158] M.C. Cheung, R. LaCroix, B.K. Mckenna, L. Liu, J. Winkelman, D.J. Ehrlich, Intracellular Protein and Nucleic Acid Measured in Eight Cell Types Using Deep-Ultraviolet Mass Mapping, *Cytom. Part A.* 83A (2013) 540–551. doi:10.1002/cyto.a.22277.
- [159] M.C. Cheung, J.G. Evans, B. Mckenna, D.J. Ehrlich, Deep ultraviolet mapping of intracellular protein and nucleic acid in femtograms per pixel, *Cytom. Part A.* 79 A (2011) 920–932. doi:10.1002/cyto.a.21111.
- [160] B.J. Zeskind, C.D. Jordan, W. Timp, L. Trapani, G. Waller, V. Horodincu, D.J. Ehrlich, P. Matsudaira, Nucleic acid and protein mass mapping by live-cell deep-ultraviolet microscopy, *Nat. Methods.* 4 (2007) 567–570. doi:10.1038/NMETH1053.
- [161] J.M.R. Hatfield, L. Schulze, D. Ernst, Measurement of the ultraviolet absorption in specific parts of both living and fixed mammalian cells, using a specially designed microspectrophotometer, *Exp. Cell Res.* 59 (1970) 484–486. doi:10.1016/0014-4827(70)90659-2.
- [162] E. Huynh, G. Zheng, Porphysome nanotechnology: A paradigm shift in lipid-based supramolecular structures, *Nano Today.* 9 (2014) 212–222. doi:10.1016/j.nantod.2014.04.012.
- [163] D.B. Chithrani, A.A. Ghazani, W.C.W. Chan, Determining the size and shape dependence of gold nanoparticle uptake into mammalian cells, *Nano Lett.* 6 (2006) 662–668. doi:10.1021/nl0523960.

- [164] L.I. Zon, R.T. Peterson, In vivo drug discovery in the zebrafish, *Nat. Rev. Drug Discov.* 4 (2005) 35–44. doi:10.1038/nrd1606.
- [165] G.J. Lieschke, P.D. Currie, Animal models of human disease: zebrafish swim into view., *Nat. Rev. Genet.* 8 (2007) 353–367. doi:10.1038/nrg2091.
- [166] Q. Chen, T. Jin, W. Qi, X. Mo, L. Xi, Label-free photoacoustic imaging of the cardio-cerebrovascular development in the embryonic zebrafish, *Biomed. Opt. Express.* 8 (2017) 2359. doi:10.1364/BOE.8.002359.
- [167] R. Ma, M. Distel, X.L. Deán-Ben, V. Ntziachristos, D. Razansky, Non-invasive whole-body imaging of adult zebrafish with optoacoustic tomography, *Phys. Med. Biol.* 57 (2012) 7227–37. doi:10.1088/0031-9155/57/22/7227.
- [168] J. Karlsson, J. von Hofsten, P.E. Olsson, Generating transparent zebrafish: a refined method to improve detection of gene expression during embryonic development., *Mar. Biotechnol. (NY)*. 3 (2001) 522–7. doi:10.1007/s1012601-0053-4.
- [169] R.M. White, A. Sessa, C. Burke, T. Bowman, J. LeBlanc, C. Ceol, C. Bourque, M. Dovey, W. Goessling, C.E. Burns, L.I. Zon, Transparent Adult Zebrafish as a Tool for In Vivo Transplantation Analysis, *Cell Stem Cell.* 2 (2008) 183–189. doi:10.1016/j.stem.2007.11.002.
- [170] S. Isogai, M. Horiguchi, B.M. Weinstein, The Vascular Anatomy of the Developing Zebrafish: An Atlas of Embryonic and Early Larval Development, *Dev. Biol.* 230 (2001) 278–301. doi:10.1006/dbio.2000.9995.
- [171] R. Ross, Atherosclerosis--An inflammatory disease, *N. Engl. J. Med.* 340 (1999) 115–126. doi:10.1056/NEJM199901143400207.
- [172] S. Jeon, J. Kim, J.P. Yun, C. Kim, Non-destructive photoacoustic imaging of metal surface defects, *J. Opt.* 18 (2016) 114001. doi:10.1088/2040-8978/18/11/114001.
- [173] U. Bernini, P. Mormile, A. Novellino, P. Russo, Photoacoustic imaging of layered microcircuits for non-destructive evaluation of sub-surface defects, *J. Mater.*

- Process. Technol. 54 (1995) 181–185. doi:10.1016/0924-0136(95)01939-1.
- [174] R.N. Johnston, a Atalar, J. Heiserman, V. Jipson, C.F. Quate, Acoustic microscopy: resolution of subcellular detail., Proc. Natl. Acad. Sci. U. S. A. 76 (1979) 3325–3329. doi:10.1073/pnas.76.7.3325.
- [175] E.M. Strohm, G.J. Czarnota, M.C. Kolios, Quantitative Measurements of Apoptotic Cell Properties Using Acoustic Microscopy, IEEE Trans. Ultrason. Ferroelectr. Freq. Control. 57 (2010) 2293–2304.
- [176] P. Subochev, A. Orlova, I. Mikhailova, N. Shilyagina, I. Turchin, Simultaneous in vivo imaging of diffuse optical reflectance, optoacoustic pressure, and ultrasonic scattering, Biomed. Opt. Express. 7 (2016) 3951–3957. doi:10.1364/BOE.7.003951.
- [177] P. Subochev, Cost-effective imaging of optoacoustic pressure, ultrasonic scattering, and optical diffuse reflectance with improved resolution and speed, Opt. Lett. 41 (2016) 1006–1009. doi:10.1109/LO.2016.7549981.
- [178] P. Subochev, I. Fiks, M. Frenz, I. Turchin, Simultaneous triple-modality imaging of diffuse reflectance, optoacoustic pressure and ultrasonic scattering using an acoustic-resolution photoacoustic microscope: Feasibility study, Laser Phys. Lett. 13 (2016) 025605. doi:10.1088/1612-2011/13/2/025605.
- [179] C.F. Quate, A. Atalar, H.K. Wickramasinghe, Acoustic microscopy with mechanical scanning. A review, Proc. IEEE. 67 (1979) 1092–1114. doi:10.1109/PROC.1979.11406.
- [180] C.F. Quate, Acoustic Microscopy, Trends Biochem. Sci. 2 (1977) N127–N129.
- [181] X.W. Sun, H.S. Kwok, Optical properties of epitaxially grown zinc oxide films on sapphire by pulsed laser deposition, J. Appl. Phys. 86 (1999) 408–411. doi:10.1063/1.370744.
- [182] P.J. Smith, M. Wiltshire, S. Davies, L.H. Patterson, T. Hoy, A novel cell permeant and far red-fluorescing DNA probe, DRAQ5, for blood cell discrimination by flow cytometry, J. Immunol. Methods. 229 (1999) 131–139. doi:10.1016/S0022-

1759(99)00116-7.

- [183] R.M. Martin, H. Leonhardt, M.C. Cardoso, DNA labeling in living cells, *Cytom. Part A*. 67 (2005) 45–52. doi:10.1002/cyto.a.20172.
- [184] L. Koss, *Koss' Diagnostic Cytology and Its Histopathologic Bases*, 5ed., 5th ed., Lippincott Williams & Wilkins, 2006.
- [185] K. Njoh, L. Patterson, M. Zloh, M. Wiltshire, J. Fisher, S. Chappell, S. Ameer-Beg, Y. Bai, D. Matthews, R. Errington, P. Smith, Spectral Analysis of the DNA Targeting Bisalkylaminoanthraquinone DRAQ5 in Intact Living Cells, *Cytom. Part A*. 69A (2006) 805–814. doi:10.1002/cyto.a.
- [186] J. Yoon, K. Kim, H. Park, C. Choi, S. Jang, Y. Park, Label-free characterization of white blood cells by measuring 3D refractive index maps, *Biomed. Opt. Express*. 6 (2015) 3865. doi:10.1364/BOE.6.003865.
- [187] M. Habaza, M. Kirschbaum, C. Guernth-Marschner, G. Dardikman, I. Barnea, R. Korenstein, C. Duschl, N.T. Shaked, Rapid 3D Refractive-Index Imaging of Live Cells in Suspension without Labeling Using Dielectrophoretic Cell Rotation, *Adv. Sci*. 4 (2017). doi:10.1002/advs.201600205.
- [188] I.T. Young, P.W. Verbeek, B.H. Mayall, Characterization of chromatin distribution in cell nuclei, *Cytometry*. 7 (1986) 467–474. doi:10.1002/cyto.990070513.
- [189] R.D. Allen, G.B. David, G. Nomarski, The Zeiss-Nomarski differential interference equipment for transmitted-light microscopy., *Z. Wiss. Mikrosk.* 69 (1969) 193–221.
- [190] M.A. Green, Self-consistent optical parameters of intrinsic silicon at 300 K including temperature coefficients, *Sol. Energy Mater. Sol. Cells*. 92 (2008) 1305–1310. doi:10.1016/j.solmat.2008.06.009.
- [191] H. Kaeslin, *Digital Integrated Circuit Design: From VLSI Architectures to CMOS Fabrication*, Cambridge University Press, New York, 2008.
- [192] L.D. Favro, P.K. Kuo, J.J. Pouch, R.L. Thomas, Photoacoustic microscopy of an

- integrated circuit, *Appl. Phys. Lett.* 36 (1980) 953–954. doi:10.1063/1.91662.
- [193] J. Chen, I. De Wolf, Study of damage and stress induced by backgrinding in Si wafers, *Semicond. Sci. Technol.* 18 (2003) 261–268.
- [194] M. Nikoonahad, Recent advances in high resolution acoustic microscopy, *Contemp. Phys.* 25 (1984) 129–158. doi:10.1080/00107518408230325.
- [195] J. Bilotta, S. Saszik, A.S. Delorenzo, H.R. Hardesty, Establishing and maintaining a low-cost zebrafish breeding and behavioral research facility, *Behav. Res. Methods, Instruments, Comput.* 31 (1999) 178–184. doi:10.3758/BF03207707.
- [196] M. Westerfield, *The zebrafish book. A guide for the laboratory use of zebrafish (Danio Rerio).*, 4th ed., University of Oregon Press, Eugene, OR, USA., 2000.
- [197] C.A. MacRae, R.T. Peterson, Zebrafish as tools for drug discovery, *Nat. Rev. Drug Discov.* 14 (2015) 721–731. doi:10.1038/nrd4627.
- [198] J.S. Eisen, J.A. Weston, Development of the neural crest in the zebrafish, *Dev. Biol.* 159 (1993) 50–59. doi:10.1006/dbio.1993.1220.
- [199] D.M. Parichy, M.R. Elizondo, M.G. Mills, T.N. Gordon, E. Engeszer, Normal Table of Post-Embryonic Zebrafish Development: Staging by Externally Visible Anatomy of the Living Fish, 238 (2009) 2975–3015. doi:10.1002/dvdy.22113.Normal.
- [200] R.N. Kelsh, Genetics and evolution of pigment patterns in fish, *Pigment Cell Res.* 17 (2004) 326–336. doi:10.1111/j.1600-0749.2004.00174.x.
- [201] A.P. Singh, C. Nüsslein-Volhard, Zebrafish stripes as a model for vertebrate colour pattern formation, *Curr. Biol.* 25 (2015) R81–R92. doi:10.1016/j.cub.2014.11.013.
- [202] S. Ye, R. Yang, J. Xiong, K.K. Shung, Q. Zhou, C. Li, Q. Ren, Label-free imaging of zebrafish larvae in vivo by photoacoustic microscopy, *Biomed. Opt. Express.* 3 (2012) 360. doi:10.1364/BOE.3.000360.
- [203] J. Yang, L. Gong, X. Xu, P. Hai, Y. Shen, Y. Suzuki, L. V. Wang, Motionless

- volumetric photoacoustic microscopy with spatially invariant resolution, *Nat. Commun.* 8 (2017) 1–7. doi:10.1038/s41467-017-00856-2.
- [204] B. Rao, F. Soto, D. Kerschensteiner, L. V Wang, Integrated photoacoustic, confocal, and two-photon microscope, *J. Biomed. Opt.* 19 (2014) 036002. doi:10.1117/1.JBO.19.3.036002.
- [205] D. Soliman, G.J. Tserevelakis, M. Omar, V. Ntziachristos, Combining microscopy with mesoscopy using optical and optoacoustic label-free modes, *Sci. Rep.* 5 (2015) 1–9. doi:10.1038/srep12902.
- [206] R. Haindl, S. Preisser, M. Andreana, W. Rohringer, C. Sturtzel, M. Distel, Z. Chen, E. Rank, B. Fischer, W. Drexler, M. Liu, Dual modality reflection mode optical coherence and photoacoustic microscopy using an akinetic sensor, *Opt. Lett.* 42 (2017) 4319. doi:10.1364/OL.42.004319.
- [207] M.J. Moore, E.M. Strohm, M.C. Kolios, Simultaneous photoacoustic and optical attenuation imaging of single cells using photoacoustic microscopy, in: *Prog. Biomed. Opt. Imaging - Proc. SPIE*, 2016. doi:10.1117/12.2212961.
- [208] M.J. Moore, E.M. Strohm, M.C. Kolios, Triplex micron-resolution acoustic, photoacoustic, and optical transmission microscopy via photoacoustic radiometry, *Opt. Express.* 26 (2018) 22315–22326.
- [209] A.M. Philip, Y. Wang, A. Mauro, S. El-Rass, J.C. Marshall, W.L. Lee, A.S. Slutskym, C.C. dos Santos, X.-Y. Wen, Development of a Zebrafish Sepsis Model for High-Throughput Drug Discovery, *Mol. Med.* 23 (2017) 134–148. doi:10.2119/molmed.2016.00188.
- [210] S.-W. Jin, D. Beis, T. Mitchell, J.-N. Chen, D.Y.R. Stainier, Cellular and molecular analyses of vascular tube and lumen formation in zebrafish, *Development.* 132 (2005) 5199–5209. doi:10.1242/dev.02087.
- [211] E. De Luca, G.M. Zaccaria, M. Hadhoud, G. Rizzo, R. Ponzini, U. Morbiducci, M.M.

- Santoro, ZebraBeat : A flexible platform for the analysis of the cardiac rate in zebrafish embryos, *Sci. Rep.* 4 (2014) 1–13. doi:10.1038/srep04898.
- [212] T. Chaigne, B. Arnal, S. Vilov, E. Bossy, O. Katz, Super-resolution photoacoustic imaging via flow induced absorption fluctuations, *Optica*. 4 (2017) 1397–1404. doi:10.1364/OPTICA.4.001397.
- [213] C. Errico, J. Pierre, S. Pezet, Y. Desailly, Z. Lenkei, O. Couture, M. Tanter, Ultrafast ultrasound localization microscopy for deep super-resolution vascular imaging, *Nature*. 527 (2015) 499–502. doi:10.1038/nature16066.
- [214] C.B. Kimmel, W.W. Ballard, S.R. Kimmel, B. Ullmann, T.F. Schilling, Stages of embryonic development of the zebrafish, *Dev. Dyn.* 203 (1995) 253–310. doi:10.1002/aja.1002030302.
- [215] S. Isogai, N.D. Lawson, S. Torrealday, M. Horiguchi, B.M. Weinstein, Angiogenic network formation in the developing vertebrate trunk, *Development*. 130 (2003) 5281–5290. doi:10.1242/dev.00733.
- [216] J.Y. Bertrand, A.D. Kim, S. Teng, D. Traver, CD41⁺ cmyb⁺ precursors colonize the zebrafish pronephros by a novel migration route to initiate adult hematopoiesis, *Development*. 135 (2008) 1853–1862. doi:10.1242/dev.015297.
- [217] E. Murayama, K. Kissa, A. Zapata, E. Mordelet, V. Briolat, H.F. Lin, R.I. Handin, P. Herbomel, Tracing Hematopoietic Precursor Migration to Successive Hematopoietic Organs during Zebrafish Development, *Immunity*. 25 (2006) 963–975. doi:10.1016/j.immuni.2006.10.015.
- [218] K. Kulkeaw, D. Sugiyama, Zebrafish erythropoiesis and the utility of fish as models of anemia, *Stem Cell Res. Ther.* 3 (2012) 1–11. doi:10.1186/scrt146.
- [219] M. Hirata, K.I. Nakamura, T. Kanemaru, Y. Shibata, S. Kondo, Pigment cell organization in the hypodermis of zebrafish, *Dev. Dyn.* 227 (2003) 497–503. doi:10.1002/dvdy.10334.

- [220] J.T. Bagnara, P.J. Fernandez, R. Fujii, On the blue coloration of vertebrates, *Pigment Cell Res.* 20 (2007) 14–26. doi:10.1111/j.1600-0749.2006.00360.x.
- [221] K. Curran, J.A. Lister, G.R. Kunkel, A. Prendergast, D.M. Parichy, D.W. Raible, Interplay between Foxd3 and Mitf regulates cell fate plasticity in the zebrafish neural crest, *Dev. Biol.* 344 (2010) 107–118. doi:10.1016/j.ydbio.2010.04.023.
- [222] T.C. Tran, B. Sneed, J. Haider, D. Blavo, A. White, T. Aiyejorun, T.C. Baranowski, A.L. Rubinstein, T.N. Doan, R. Dingledine, E.M. Sandberg, Automated, quantitative screening assay for antiangiogenic compounds using transgenic zebrafish, *Cancer Res.* 67 (2007) 11386–11392. doi:10.1158/0008-5472.CAN-07-3126.
- [223] D. Alex, I.K. Lam, Z. Lin, S.M.Y. Lee, Indirubin shows anti-angiogenic activity in an in vivo zebrafish model and an in vitro HUVEC model, *J. Ethnopharmacol.* 131 (2010) 242–247. doi:10.1016/j.jep.2010.05.016.
- [224] C. Wang, W. Tao, Y. Wang, J. Bikow, B. Lu, A. Keating, S. Verma, T.G. Parker, R. Han, X.Y. Wen, Rosuvastatin, identified from a zebrafish chemical genetic screen for antiangiogenic compounds, suppresses the growth of prostate cancer, *Eur. Urol.* 58 (2010) 418–426. doi:10.1016/j.eururo.2010.05.024.
- [225] S. Eisa-Beygi, X.-Y. Wen, R.L. Macdonald, A call for rigorous study of statins in resolution of cerebral cavernous malformation pathology, *Stroke.* 45 (2014) 1859–1861. doi:10.1161/STROKEAHA.114.005132.
- [226] S. Eisa-Beygi, R.L. MacDonald, X.-Y. Wen, Regulatory pathways affecting vascular stabilization via VE-cadherin dynamics: Insights from zebrafish (*Danio rerio*), *J. Cereb. Blood Flow Metab.* 34 (2014) 1430–1433. doi:10.1038/jcbfm.2014.128.
- [227] C.S. Lim, E.S. Kim, J.Y. Kim, S.T. Hong, H.J. Chun, D.E. Kang, B.R. Cho, Measurement of the Nucleus Area and Nucleus/Cytoplasm and Mitochondria/Nucleus Ratios in Human Colon Tissues by Dual-Colour Two-Photon Microscopy Imaging, *Sci. Rep.* 5 (2015) 1–11. doi:10.1038/srep18521.

- [228] M. Cristofanilli, M.J. Ellis, A. Stopeck, J. Matera, M.C. Miller, M. Reuben, James, G. V. Doyle, W.J. Allard, L.W.W.M. Terstappen, D.F. Hayes, Circulating Tumor Cells, Disease Progression, and Survival in Metastatic Breast Cancer, *N. Engl. J. Med.* 351 (2004) 781–791.
- [229] S. Nagrath, L. V Sequist, S. Maheswaran, D.W. Bell, D. Irimia, L. Ulkus, M.R. Smith, E.L. Kwak, S. Digumarthy, A. Muzikansky, P. Ryan, U.J. Balis, R.G. Tompkins, D. a Haber, M. Toner, Isolation of rare circulating tumour cells in cancer patients by microchip technology., *Nature.* 450 (2007) 1235–9. doi:10.1038/nature06385.
- [230] P. Paterlini-Brechot, N.L. Benali, Circulating tumor cells (CTC) detection: Clinical impact and future directions, *Cancer Lett.* 253 (2007) 180–204. doi:10.1016/j.canlet.2006.12.014.
- [231] S. Meng, D. Tripathy, E.P. Frenkel, S. Shete, E.Z. Naftalis, J.F. Huth, P.D. Beitsch, M. Leitch, S. Hoover, D. Euhus, B. Haley, L. Morrison, T.P. Fleming, D. Herlyn, L.W. Terstappen, T. Fehm, T.F. Tucker, N. Lane, J. Wang, J.W. Uhr, Circulating tumor cells in patients with breast cancer dormancy, *Clin Cancer Res.* 10 (2004) 8152–8162. doi:10.1158/1078-0432.CCR-04-1110.
- [232] V. Gnyawali, E.M. Strohm, S.S.H. Tsai, M.C. Kolios, Simultaneous ultrasound and photoacoustics based flow cytometry, in: *Prog. Biomed. Opt. Imaging - Proc. SPIE*, 2018: p. 104940H.
- [233] V. Gnyawali, E.M. Strohm, J.-Z. Wang, S.S.H. Tsai, M.C. Kolios, Microfluidic acoustic and photoacoustic flow cytometry: a label-free approach, *Prep.* (2018).
- [234] E.M. Strohm, V. Gnyawali, J.A. Sebastian, R. Ngunjiri, M.J. Moore, S.S.H. Tsai, M.C. Kolios, Sizing biological cells using a microfluidic acoustic flow cytometer, *Prep.* (2018).
- [235] V. Gnyawali, Development of microfluidic acoustic flow cytometry based on simultaneous ultrasound backscatter and photoacoustics for micron and sub-micron size objects, Ryerson University, 2018.

- [236] C.J. Veinotte, G. Dellaire, J.N. Berman, Hooking the big one: the potential of zebrafish xenotransplantation to reform cancer drug screening in the genomic era, *Dis. Model. Mech.* 7 (2014) 745–754. doi:10.1242/dmm.015784.
- [237] R.T. Peterson, B.A. Link, J.E. Dowling, S.L. Schreiber, Small molecule developmental screens reveal the logic and timing of vertebrate development, *Proc. Natl. Acad. Sci.* 97 (2000) 12965–12969. doi:10.1073/pnas.97.24.12965.
- [238] S.H. Lam, H.L. Chua, Z. Gong, T.J. Lam, Y.M. Sin, Development and maturation of the immune system in zebrafish, *Danio rerio*: A gene expression profiling, in situ hybridization and immunological study, *Dev. Comp. Immunol.* 28 (2004) 9–28. doi:10.1016/S0145-305X(03)00103-4.
- [239] I.J. Marques, F.U. Weiss, D.H. Vlecken, C. Nitsche, J. Bakkers, A.K. Lagendijk, L.I. Partecke, C.D. Heidecke, M.M. Lerch, C.P. Bagowski, Metastatic behaviour of primary human tumours in a zebrafish xenotransplantation model, *BMC Cancer.* 9 (2009). doi:10.1186/1471-2407-9-128.

Glossary

AR-PAM	Acoustic Resolution Photoacoustic Microscopy
dB	Decibel
DMEM	Dulbecco's Modified Eagle Medium
dpf	Days-post-fertilization
FC	Flow Cytometry
FEM	Finite Element Method
FWHM	Full-width at Half-maximum
GFP	Green Fluorescent Protein
I ₃ M	Indirubin-3'-Monoxime
IFC	Image Flow Cytometry
MAP	Maximum Amplitude Projection
N:C	Nucleus-to-Cytoplasmic
OR-PAM	Optical Resolution Photoacoustic Microscopy
PA	Photoacoustic
PACF	Photoacoustic Flow Cytometry
PAM	Photoacoustic Microscopy
PAR	Photoacoustic Radiometry
PAT	Photoacoustic Tomography
PBS	Phosphate-buffered saline
PTFC	Photothermal Flow Cytometry
PTU	1-Phenyl 2-Thiourea
RBC	Red Blood Cell
ROI	Region of Interest
SASAM	Saarland scanning acoustic microscope
SNR	Signal-to-Noise Ratio
UHF	Ultra-high Frequency
UV	Ultra-violet
US	Ultrasound